الجمهورية الجزائرية الديمقراطية الشعبية
République Algérienne Démocratique et Populaire
وزارة التعليم العالي والبحث العلمي
Ministère de l'enseignement supérieur et la recherche scientifique

Université Mohamed Khider – Biskra
Faculté des Sciences et de la technologie
Département : Génie électrique
Ref : ……

جامعة محمد خيضر بسكرة
كلية العلوم والتكنولوجيا
قسم: الهندسة الكهربائية
المرجع: .....

Thèse présentée en vue de l'obtention
Du diplôme de

Doctorat LMD en : électronique

Spécialité (Option) : Micro-électronique

Intitulé

Etude et simulation d'un laser à semiconducteur à puits quantique
(Study and simulation of a semiconductor single quantum well laser)

Présentée par :

Menani Adel

Soutenue publiquement le : 15/12/2021

Devant le jury composé de :

Pr. Saadoune Achour	**Professeur**	**Président**	**Université de Biskra**
Pr. Lakhdar Dehimi	**Professeur**	**Rapporteur**	**Université de Batna**
Dr. Beddiaf Zaidi	**Maitre de conférences A**	**Examinateur**	**Université de Batna**
Dr Bekhouche Khaled	**Maitre de conférences A**	**Examinateur**	**Université de Biskra**
Dr. Megherbi Med Larbi	**Maitre de conférences A**	**Examinateur**	**Université de Biskra**

الجمهورية الجزائرية الديمقراطية الشعبية
République Algérienne Démocratique et Populaire
وزارة التعليم العالي والبحث العلمي
Ministère de l'enseignement supérieur et la recherche scientifique

Université Mohamed Khider – Biskra
Faculté des Sciences et de la technologie
Département : Génie électrique
Ref : ……

جامعة محمد خيضر بسكرة
كلية العلوم والتكنولوجيا
قسم: الهندسة الكهربائية
المرجع: .....

Thèse présentée en vue de l'obtention
Du diplôme de

Doctorat LMD en : électronique

Spécialité (Option) : Micro-électronique

Intitulé

Etude et simulation d'un laser à semiconducteur à puits quantique
(Study and simulation of a semiconductor single quantum well laser)

Présentée par :

Menani Adel

Soutenue publiquement le : 15/12/2021

Devant le jury composé de :

Pr. Saadoune Achour	**Professeur**	**Président**	**Université de Biskra**
Pr. Lakhdar Dehimi	**Professeur**	**Rapporteur**	**Université de Batna**
Dr. Beddiaf Zaidi	**Maitre de conférences A**	**Examinateur**	**Université de Batna**
Dr Bekhouche Khaled	**Maitre de conférences A**	**Examinateur**	**Université de Biskra**
Dr. Megherbi Med Larbi	**Maitre de conférences A**	**Examinateur**	**Université de Biskra**

Study and simulation of a semiconductor single quantum well laser

Thesis in

Micro-Electronics

by

Adel Menani

In Fulfilment of the requirements for the degree

of

LMD Doctorate

2021

ACKNOWLEDGEMENT

In the name of Allah, the Most Gracious and the Most Merciful.

A long journey it was, with all its ups and downs, a quotidian struggle, it would be the definition of this doctoral research path, sometimes between relieving joy and deep frustration, between enjoying every day's learning and overcoming the little failures… One would name it a beautiful burden and an amazing chapter of life, hoping for a bright new chapter, with the same thirst of learning and learning and learning.

All praises to Allah and His blessing for the completion of this thesis. I thank Allah for all the opportunities, trials and strength that have been showered on me to finish writing the thesis. I experienced so much during this process, not only from the academic aspect but also from the aspect of personality.

It's a genuine pleasure to express my sincere gratitude to my mentor professor, tutor and supervisor Pr.Dehimi Lakhdar for his valuable guidance and support during my PhD research, with all his advices and encouragement, I was able to reach the completion of this work… for an honourable man and kind teacher that he is … and for the huge positive impact he has on my life since the first day we met.

All the thanks to my Dr.Dehimi Said for all the help and advices that he provided me with during this period, a true friend and a very helpful colleague indeed.

I would like also to express my thanks to Dr.Furtunato Pezzimente for his good collaboration and continuous correspondence.

I thank profusely my reading committee members and respectful teachers: Dr.Megherbi Mohamed Larbi, Dr.Bakhouche Khaled, Pr.Saadoune Achour and Dr.Beddiaf Zaidi … for their time, efforts and interest and also their contribution to the success of the viva.

To every single member of my family and friends and all teachers from all stages, from primary school to University.

DEDICATION

To my father … my source of inspiration

To my mother … to you all my devotion

To my wife … my love … my passion

ملـــخص

في الوقت الحاضر، أصبح تطوير الليزر قصير الطول الموجي الذي ينبعث منه ضوء متماسك باللون الأخضر، الأزرق، البنفسجي أو الأشعة فوق البنفسجية (UV) أحد أهم التحديات في مجال الإلكترونيات الضوئية، وعلى وجه الخصوص، تلك التي تنتجها النتريد -III المواد ذات فجوة الحزمة الواسعة المصنوعة من النيتريد-III.

خلال هذه الأطروحة، تم تحقيق نمذجة ليزر البنية النانوية للبئر الكمي المضغوط المكون أساسا من AlxGa1-xN / Wurtzite III-GaN باستخدام برنامج محاكاة ATLAS الخاص بـ SILVACO-TCAD. كان التركيز الرئيسي لهذا العمل البحثي هو دراسة تأثير سُمك البئر الكمي (QW) ، وكثافة النواقل ، وتركيز الألومنيوم (Al) في طبقات الحاجز على الخصائص الضوئية (الكسب الضوئي ، الانبعاث التلقائي والكثافة الطيفية للطاقة) و الخصائص الكهربائية ليزر ذو بئر كمي مكون أساسا من نيتريد الغاليوم (GaN)، والذي يتم فحصه عن طريق تحليل نمذجة دقيقة في نطاق واسع من درجات الحرارة ، كل ذلك باستخدام منهجين مختلفين لحساب حواف نطاق الطاقة والكتل الفعالة، حيث في البداية نفترض أن نطاقي النقل والتكافؤ هي قطع مكافئة، أما النموذج الثاني فلا يعتبر نطاقات الطاقة قطع مكافئة ويتم حسابه عبر شكلية k.p 6×6 نطاقات.

تسمح لنا النتائج أن نقول أنه باستخدام طريقة k.p، يمكننا الحصول على نتائج أكثر دقة يتم التعبير عنها ككسب بصري معتبر مع كثافة تيار عتبة منخفضة تعمل في درجات حرارة عالية وتنبعث ضمن نظام الأشعة فوق البنفسجية (UV).

الكلمات المفتاحية: بئر كمي، Wurtzite، الكسب الضوئي، طريقة k.p، تيار العتبة.

ABSTRACT

Nowadays, the development of short wavelength lasers which can emit coherent light in green, blue, violet, and ultraviolet (UV) regimes become one of the most important challenges in the field of optoelectronics, and in particular, those made by III-nitride wide bandgap materials.

During this thesis, a modelling of a wurtzite compressive strain quantum well nanostructure laser based on III-nitride GaN/$Al_xGa_{1-x}N$ was achieved by the use of ATLAS of SILVACO TCAD simulation software. The main focus of this research work was to study the effect of the quantum well (QW) width, carrier density, and Aluminum (Al) concentration in the barrier layers on the optical (optical gain, spontaneous emission and the power spectral density) and electrical characteristics of a gallium nitride (GaN)-based QW laser diode, which is investigated by means of a careful modelling analysis in a wide range of temperature, all by using two different approaches for the calculation of energy band edges and effective masses, where in the first we assume the conduction and valence bands are parabolic, however, the second model consider the non-parabolicity of the bands and computed via 6×6 band k.p formalism.

The results allow us to say that, by the use k.p method, we can get more accurate results that are expressed as a more significant optical gain with low threshold current density operating at high temperatures and emitting in the ultraviolet (UV) regime.

Keywords: Quantum well, Wurtzite, Optical gain, k.p method, Threshold current.

RESUME

De nos jours, le développement des lasers à courtes longueurs d'ondes qui peuvent émettre une lumière cohérente dans les régimes vert, bleu, violet et ultraviolet (UV) devient l'un des défis les plus importants dans le domaine de l'optoélectronique, et en particulier, ceux fabriqués en matériaux à large bande interdite à base de III-nitrure.

Au cours de cette thèse, une modélisation d'un laser à nanostructure à puits quantique à contrainte compressive à base de wurtzite III-nitrure GaN / AlxGa1-xN a été réalisée en utilisant ATLAS du logiciel de simulation SILVACO TCAD. L'objectif principal de ce travail de recherche était d'étudier l'effet de la largeur du puits quantique (QW), de la densité des porteurs et de la concentration d'aluminium (Al) dans les couches barrières sur les caractéristiques optiques (gain optique, émission spontanée et densité spectrale de puissance) et électriques d'une diode laser à un puits quantique à base de nitrure de gallium (GaN), et qui est étudiée l'intérêt d'une analyse de modélisation minutieuse dans une large gamme de températures, tout en utilisant deux approches différentes pour le calcul des bordures de bandes d'énergie et des masses effectives, où dans la première nous supposons que les bandes de conduction et valence sont paraboliques, cependant, le second modèle considère la non-parabolicité des bandes et est calculée via le formalisme k.p 6 × 6 bandes.

Les résultats permettent de dire que, par l'utilisation de la méthode k.p, on peut obtenir des résultats plus précis exprimés en gain optique plus important avec une faible densité de courant de seuil fonctionnant à des températures élevées et émettant dans le régime ultraviolet (UV).

Mots clés: puits quantique, Wurtzite, gain optique, méthode k.p, courant de seuil.

TABLE OF CONTENTS

Dedication

Acknowledgments

ملخص ……..…….…. I

Abstract ……..…… II

Resumé ……..... III

Table of contents ……..……... IV

List of figures ……. IX

List of tables ……..… XII

INTRODUCTION

A brief history of nitride-based materials ……. 1

State of the art of GaN-based Single Quantum Well lasers …….. 2

Motivation and objectives of the study …….. 3

Organization of the manuscript …….. 3

CHAPTER 1: PROPERTIES OF III-NITRIDES AND FABRICATION OVERVIEW

1-1 General properties of III-nitrides …… 6

1.2 Crystal polarity …… 8

1.2.1 Dislocations ……..…… 9

1.2.2 Elastic properties ……..…… 11

1.3 Spontaneous and piezoelectric polarization ……..……. 12

1.4 Energy diagram ……..……..…... 14

1.4.1 direct bandgap semiconductors energy diagram ……. 14

1.4.2 band structure of III-nitride material ……. 15

1.5 Degeneracy of the valence band at the Γ point ……. 18

1.6 Carriers effective masses …… 19

1.7 c-GaN and h-GaN polytypes …….. 19

1.8 Crystal structure and properties of AlN ……..…… 20

1.8.1 Crystal structure …….. 20

1.8.2 Band structures ……. 20

1.8.3 Carriers effective masses ……... 21

1.9 Overview of deposition of GaN and AlN layers ……. 22

1.10 Group III nitrides epitaxy …… 24

1.11 Substrates and buffer layers for group III nitrides …… 24

1.11.1 Sapphire substrate ……. 25

1.11.2 Silicon carbide (SiC) substrate …….. 25

1.11.3 Silicon (Si) substrate …….. 25

1.12 Growth methodologies of GaN and AlN ……. 26

1.13 Doped GaN ……. 27

1.13.1 n-type Doping …… 28

1.13.2 p-type Doping …… 28

1.14 Doping of AlGaN ……. 30

CHAPTER 2: THEORY OF III-NITRIDE-BASED SEMICONDUCTOR LASERS

2.1 Theory of semiconductor lasers ……..…… 32

2.1.1 A brief history of semiconductor lasers ……..... 32

2.1.2 Laser applications …… 33

2.2 Basic principles of lasers …… 34

2.2.1 Radiation-matter interaction ……..... 34

2.2.2 Einstein's Model of Light–Atom Interaction ……..…… 35

a-Absorption …… 36

b-Spontaneous emission ……..…… 37

c-Stimulated emission ……..……. 37

2.2.3 Conditions for Population Inversion …… 38

2.3 Laser oscillation ……..…… 41

2.4 Inversion Threshold ……...…… 43

2.5 Laser band structure ……..……..…… 46

2.6 Quantum wells ……...…… 47

2.7 laser optical responses …… 50

2.7.1 Threshold current …… 50

2.7.2 Light Spectra and Efficiencies …… 52

2.7.3 Power-Light characteristic and external efficiency …… 54

2.8 laser optical gain …… 55

2.8.1 gain expression and achieving conditions …… 55

2.8.2 optical coefficients and rates of radiative interactions ……..…… 57

2.9 The optical gain in quantum wells ……..……..…… 59

2.9.1 Emission wavelength ……...…… 60

2.9.2 Density of energy levels ……..…… 61

2.9.3 gain expression with wave vector conservation ……...…… 62

CHAPTER 3: PHYSICAL MODELS AND SIMULATION INTERFACE

3.1 The physical models ……..……. 66

3.1.1 The calculation of the density of states …… 66

3.1.2 Band gap energy ……..…… 66

3.1.2.1 General ternary band gap model with bowing ……..…… 66

3.1.2.2 Band gap narrowing ……..…..… 67

3.1.3 Spontaneous and piezoelectric polarisation ……..… 67

3.1.4 Shockley-Read-Hall …… 67

3.1.5 Auger recombination ……...… 68

3.1.6 Impact ionization / Incomplete ionization ……. 68

3.1.7 Mobility model …… 69

3.1.8 The radiative recombination model ……..…… 70

3.1.9 The refractive index model ……...… 71

3.1.10 Threshold Current Density …… 72

3.1.11 Calculations for the optical gain …… 72

3.1.11.1 The parabolic band model …….. 72

3.1.11.2 k.p band model …… 75

3.2 The simulation process ……..…….. 77

3.2.1 ATLAS inputs and outputs ……..…… 78

3.2.2 ATLAS commands ……..…… 79

a- Structure specification ……...……. 80

I- The Mesh specification ……...…… 80

II- Regions specification …… 82

III- Electrodes specification ……..…… 82

IV- Doping profile ……...…… 82

b- Materials and models specification ……..…… 83
I- Material properties specification …… 83
II- Physical models specification ……..… 84
III- Contacts specification ……..… 86
1- Numerical methods ……...……... 86
2- Solution specification …….. 87
3- Graphical user interface extraction……..……...…..…… 88

CHAPTER 4: RESULTS AND DISCUSSION

4.1 Introduction ……..…… 90

4.2 The device structure ……...…… 90

4.3 The band diagrams ……..…...… 92

4.4 The band gap energy dependence Aluminum content …… 92

4.5 The spontaneous emission dependent Aluminum content ……..…… 94

4.6 The power spectral density dependent Aluminum content ……..…… 97

4.7 The optical gain ……...… ……..… 98

4.7.1 The optical gain-carrier density dependence ……... 99

4.7.2 The optical gain-Aluminum content dependence ……...……... 101

4.7.3 The optical gain-well width dependence ……..……. 102

4.7.4 The optical gain-temperature dependence …….…… 103

4.7.5 The quantum well band gap energy-temperature dependence ……..……..… 104

4.8 The threshold current density-temperature dependence ……...…… 107

CONCLUSION …… 108

REFERENCES …… 112

PUBLICATON …… 130

LISTE OF FIGURES

Figure 1.1: Schematic representation of (a) the wurtzite and (b) zinc-blende structures. The pink and violet spheres indicate metal and N atoms, respectively ……. 6

Figure 1.2: Hexagonal structure of GaN with representations of the base vectors and main crystallographic planes …….. 7

Figure 1. 3: Polarity in Group III nitride: Metal polar along [0001] and Nitrogen polar along [000$\bar{1}$] ……..… 9

Figure 1.4: A schematic diagram showing, edge and screw dislocation ……...… 10

Figure 1.5: Piezoelectric and spontaneous polarization-induced charge σ/q(P_SP+P_PE) ... 14

Figure 1.6: Schematic of a band model of a III-V semiconductor material with a direct bandgap ……...…… 15

Figure 1.7: Electronic structure of the valance band of (a) GaN and (b) AlN near the Brillouin zone centre point Γ (for unstrained wurtzite material. For simplicity, zero energy is assigned to the top of the valence band) …… 16

Figure 1.8: a) Zinc blende GaN band structure b) first Brillouin zone of cubic GaN lattice ……...…….... 17

Figure 1.9. a) Wurtzite GaN band structure b) first Brillouin zone of hexagonal GaN lattice …….. 18

Figure 1.10. a) Zinc-blende AlN band structure b) first Brillouin zone of hexagonal AlN lattice ……...… 20

Figure 1.11. a) Wurtzite AlN band structure b) first Brillouin zone of hexagonal AlN lattice …….. 21

Figure 2.1: Main application of LDs ……...… 33

Figure 2.2: Overall annual commercialized laser revenues in 2019 ……...…… 33

Figure 2.3: Different types of radiation-matter interaction ……..… 35

Figure 2.4: Schematic energy diagrams, retaining only the two levels E1 and E2 of the laser transition ……...…… 35

Figure 2.5: Energy transitions of an atom. a) absorption, b) spontaneous emission c) stimulated emission ……..… 36

Figure 2.6: Einstein model for the absorption radiative process …….…… 36

Figure 2.7: Einstein model for the spontaneous emission radiative process ……..…… 37

Figure 2.8: Einstein model for the stimulated emission radiative process …….…… 38

Figure 2.9: Illustration and overview of parameters which are introduced to describe multilevel atomic transitions ……...… 39

Figure 2.10: a) normal population, there are more atoms at lower levers b) population inversion, there are more atoms at higher levels …… 41

Figure 2.11: Different designs of laser oscillators. The gain medium is blue, the reflector unit of the resonator is shown in grey, and the path travelled by the photons is represented by red arrows ……..…… 42

Figure 2.12: Scheme of a typical laser oscillator …… 44

Figure 2.13: Output power dependence the resonator pumping power ……..…… 45

Figure 2.14-a: Band structure of p-n junction at thermal equilibrium …… 46

Figure 2.14-b: Band structure of a direct polarized p-n junction …… 47

Figure 2.14-c: Band structure of a polarized p-n junction with high direct voltage ……...… 47

Figure 2.15: Energy structure of GaN/AlGaN quantum well showing its quantification energy levels ……...… 49

Figure 2.16: Comparison of bulk 3-D and quantum well 2-D systems: (a) Density of states in conduction band, and (b) electron concentration distribution …….…… 50

Figure. 2.17: Optical gain as a function of laser bias current. a) Optical gain vs. emission photon energy, for different bias current b) Variation of peak optical gain with nominal current density …….…… 51

Figure 2.18: light output vs. laser bias current showing the threshold current and the three lasing regimes …….…… 52

Figure 2.19: Emission spectra of laser diode at different bias current …… 53

Figure 2.20: Population a) in thermodynamic equilibrium T = 0K, b) under inversion for T = 0K, c) under inversion for T>0K.Shaded areas are populated with electrons …… 55

Figure 2.21: Gain in the two-band models ……..… 56

Figure 2.22: Gain characteristic for a) 3-D structure (bulk) b) 2-D structure (QW) ……..… 61

Figure 2.23: The refractive index dependent Aluminium concentration in GaN and AlxGa1-xN materials ……... 63

Figure 2.24: The refractive index for AlxGa1-xN for (λ=400nm) ……..…… 64

Figure 3.1: Fermi-Dirac function and energy band diagram showing the parabolicity approximation ……..… 74

Figure 3.2: Simulation Flow for the optical model's calculations ……..… 75

Figure 3.3: Atlas inputs and outputs ……...… 78

Figure 3.4: Atlas command groups with primary statements in each groups …….…… 79

Figure 3.5: The meshing of the structure …… 81

Figure 4.1: The structure of the SQW laser diode ……..… 90

Figure 4.2: The light intensity distribution along the device ……..…… 91

Figure 4.3 AlGaN/GaN conduction and valence band edges of a compressively strained GaN QW on AlGaN barrier layers (including piezo-electric field) …… 92

Figure 4.4: The band gap energy dependence Aluminum content …….…… 93

Figure 4.5: The compressibility modulus dependent Aluminum content ……...…… 93

Figure 4.6 The transverse electric (TE) and magnetic (TM) of the spontaneous emission dependent the Al contents: (a) x=0.1, (b) x=0.15, (c) x=0.2, (d) x=0.25 and (e) x=0.3 …..… 96

Figure 4.7 The power spectral density dependent the Al contents

(x=0.1, x=.15, x=0.2, x=0.25 and x=0.3) ……...…… 98

Figure 4.8 Optical gain spectrum in an Al0.1Ga0.9N/GaN/Al0.1Ga0.9N QW laser as a function of the wavelength for different carrier densities in the active region at T = 300K. a) Parabolic band model b) 6-band k.p model ……...……100

Figure 4.9 The optical gain spectrum as a function of the Al content at T = 300 K.
a) Parabolic band model b) 6-band k.p model ……..…… 101

Figure 4.10 Optical gain spectrum as a function of the GaN QW width
(x = 0.1 and n = 1×1019 cm-3) at T = 300 K …… 102

Figure 4.11 The dependence of the optical gain on temperature in the range
T= [200, 300, 400] °k for: a) Parabolic bands model b) 6-band k.p model ……..… 103

Figure 4.12 GaN bandgap energy as a function of the temperature ……..… 104

Figure 4.13: TE-polarized optical gain spectrum for a) parabolic gain model
b) 6-band k.p gain model and c) work of Asgari et.Al ……...….. 106

Figure 4.14 The threshold current density dependence on temperature

(Lw = 40 Å, x = 0.1, and n = 1×10^{19} cm^{-3}) ……...… 107

LISTE OF TABLES

Table 1.1: Lattice parameters of bulk InN, GaN and AlN …… 7

Table 1.2: Perfect and partial dislocations in group III nitride layers, with lines along [0001] direction ……..… 10

Table 1.3: Experimental and theoretical stiffness constants of GaN and AlN in GPa …… 11

Table 1.4: Spontaneous polarization parameters [C/m^2] ……..… 13

Table 1.5: Piezoelectric polarization parameters ……..…… 13

Table 1.6: Band parameters of GaN and AlN: bandgap energy at T = 0 K; Varshni parameters; electron and hole effective masses (m_0 being the nominal mass in vacuum) …… 17

Table 1.7: Theoretical and experimental values of Δ_{SO} and Δ_{cr} for the Cubic and hexagonal GaN ……..…… 18

Table 1.8: Carriers effective masses of GaN at T=300°k …… 19

Table 1.9: Comparison between c-GaN and h-GaN polytypes …… 19

Table 1.10: Crystal parameters of h-AlN and c-AlN structures ……..…..… 20

Table 1.11 Theoretical and experimental values of ΔSO and Δcr for the c-AlN and h-AlN . 21

Table 1.12 Carriers effective masses of AlN at T=300°k ……...…… 21

Table 1.13: List of methodologies used to grow GaN and AlN ……..… 26

Table 2.1: The refractive index parameters a and b from ……...…… 63

Table 3.1: GaN impact ionization parameters …… 69

Table 3.2: Caughey and Thomas mobility parameters for GaN ……..…… 69

Table 3.3: The material statement parameters used in the simulation …… 83

Table 3.4: The physical models used in the simulation ……..…….. 84

Table 3.5: The laser physical models and parameters used in the simulation ……..... 86

INTRODUCTION

A brief history of nitride-based materials:

Group III nitrides are one of the most adequate semiconductor families for the optoelectronic, high temperature and high power electronic devices. The fundamental bandgap range of III-nitride alloy system is the widest of all known compound semiconductors, extending from InN (0.7 ± 0.05 eV1, near IR), to GaN (3.4 eV, mid UV) and finally to AlN (6.2 eV, deep UV) [1,2]. Thus group III nitrides can be used for optoelectronic applications ranging from the near infrared to the deep ultraviolet spectral region 3. Group III nitrides can operate at high temperatures and hostile environments which allow them to be used in space and nuclear reactors where Si and GaAs technologies fail to compete [3].

The history of research in group III nitrides dates effectively from about 100 years. The first synthesis of AlN, GaN and InN were reported in 1907 [4], 1910 [5] and 1932 [6] respectively. However, it took decades to receive significant research attention. In 1970's a significant advance took place in GaN research by the growth of GaN epitaxial layers on sapphire substrates using Hydride Vapor Phase Epitaxy (HVPE) [7], Molecular Organic Vapor Phase Epitaxy (MOVPE) [8] and Molecular beam epitaxy [9]. The interest in these materials was outburst with the achievement of p-type doping [10,11] which initiated the advent of violet to yellow LEDs [12-14], laser diodes [13], UV LEDs [14,15]. The development of InGaN based solar cells is also one of the emerging field of research in III-nitrides [16]. An additional effort has been made towards High Electron Mobility transistors (HEMTs) based on nitride heterojunctions [17]; and intense research activity has been dedicated towards the application of III-V nitride materials in high power, microwave-frequency electronic devices [18,19]. The large breakdown fields and high saturation velocities make the nitrides ideal for producing high power HFETs and a full range of unipolar and bipolar devices [20,21]. The transport properties of InN are better than those of GaN, which tops InN as the material most adequate for device applications in the ultra-high speed area [22].

State of the art of GaN-based Single Quantum Well lasers

Laser semiconductor diodes are key components in modern optical communications, storage, printing, medicine, and information processing. [23,24] These types of devices were developed and evolved constantly in the direction of size reduction and integration. [25,26] A quantum well (QW) laser improves the functioning characteristics of laser diodes [27,28], this improvement is expressed in the direction of low threshold current, a narrow emission band as well as emitted wavelength dependence on nanostructure dimension (quantum size effect) [29,30].

A quantum well laser is a structure in which the active region of the device is so narrow that quantum confinement occurs, according to quantum mechanics. [31,32] The wavelength of the light emitted by a quantum well laser is determined by the width of the active region rather than just the band gap of the material from which the device is realized. [33,34] Consequently, much shorter wavelengths can be obtained from quantum well lasers than from conventional laser diodes using a particular semiconductor material. [35,36] The efficiency of a quantum well laser is also greater than a conventional laser diode due to the stepwise form of its density of states function. [36-38] In the optoelectronic integrated circuits (OEICs), the quantum well lasers will interact optically and electrically with other devices as integrated modulators, optical fibers and coherent amplifiers, detectors, and optical integrated guides [39-41]. A fully analytical method to describe these kind of complex systems cannot be realistic without questionable simplifying assumptions. [42–44] The implementations of refined mathematical methods and algorithms as well as circuit simulators become essentially in the applications development. [45,46]

The ability to fabricate single quantum well (SQW) and multiple quantum well (MQW) devices has given rise to new optical and electronic devices as well as to new physical phenomena [47]. Since the first investigation of optical properties in quantum wells by Dingle et al., [48] the application of quantum well structures to semiconductor laser diodes [49,50] has received considerable attention because of physical interest as well as its superior characteristics, such as low threshold current density [51,52], low temperature dependence of threshold current [53-55], lasing wavelength tenability, and excellent dynamic properties [56-58]. By controlling the width of the quantum wells, one can modify the electron and hole wavefunctions, which leads to the modification of material parameters. This results in

improvements of the laser characteristics, as well as introduction of new concepts to semiconductor optical devices.

Nowadays, one of the most important challenges in the field of optoelectronics is the development of short wavelength lasers which can emit coherent light in green, blue, violet, and ultraviolet (UV) regimes. [59-61] In particular, III-nitride wide bandgap materials have received a great attention for the promising realization of optoelectronic devices. [62-64] These devices are able to operate at high power levels and high temperatures due to their mechanical hardness and larger band offset. [65,66] Recently, GaN-based high efficiency short wavelength LEDs and LDs have been commercialized by achieving apparent improvements in terms of crystal quality and conductivity control in solid-state lighting and high-density optical storage systems. In addition, one of the most interesting features of GaN is the realization of the wurtzite-type crystal for semiconductor lasers. Although zinc-blend GaN has also been studied in recent years it still does not have good qualities as the wurtzite crystal. [67,68]

Motivation and objectives of the study

This Phd study is one of the studies that take part of a large zone of interest of many researchers in the field of small wavelength laser diodes and their developments. However, the main goal of this research is to study the effect of the quantum well (QW) width, carrier density, and aluminum (Al) concentration in the barrier layers on the optical characteristics of a gallium nitride (GaN)-based QW laser diode, which is investigated by means of a careful modelling analysis in a wide range of temperature.

The device optical gain is calculated using two different models; the first is based on the simple parabolic band model whereas the second is based on the perturbation theory (k.p model) for calculating the band structure.

Organization of the manuscript

This manuscript is divided into three main chapters:

- **Chapter 1:** Describes the general properties of the III-nitride materials in the terms of crystalline and electronic structure as well as the discussion about the spontaneous and piezoelectric fields are presented besides the experimental techniques and fabrication processes starting from the growth of the layers (substrate, barrier layer, quantum well), into doping phase.

- **Chapter 2:** Introduces the fundamental basic principles of the semiconductor laser, the lasing process and functionalities, the cavity, the internal and external efficiency, the electric and optical responses of the III-nitride based lasers, and finishes with the optical gain in the quantum well with all calculations such as the optical coefficients and rates.
- **Chapter 3:** Describes the physical models employed into the simulation software in order to present this work, a 2-D and 3-D device simulation framework ATLAS of SILVACO TCAD, besides, it illustrates the process of introducing these models in a precise sequence in or order to achieve a sum of seeking results represented in the last chapter.
- **Chapter 4:** This chapter investigates the way of the device performance improvement by optimizing the active region of the device ($Al_xGa_{1-x}N/GaN/Al_xGa_{1-x}N$ single quantum well laser). Several studies are carried out, mentioning the spontaneous emission and the optical gain, and some of them by manipulating and changing in some parameters such as: the quantum well thickness, the Aluminium concentration in the barrier layers, the carrier injection density, the band gap and temperature dependence as well as the threshold current density dependence; all this by the use of two deferent calculation methods of the electrical and optical responses: A parabolic bands model and a multiband k.p formalism for the calculation of the non-parabolic bands and electrons and holes wave-functions.

CHAPTER 1

PROPERTIES OF III-NITRIDES

AND FABRICATION OVERVIEW

CHAPTER 1

1-1 General properties of III-nitrides:

III-Nitride semiconductors like AlN, InN and GaN can appear in three crystalline configurations, namely wurtzite (α-phase), zinc blende (β-phase) and rock salt (γ-phase) structures. The wurtzite structure shows hexagonal symmetry with two hexagonal sublattices of metal (Al, Ga, In) and nitrogen (N) atoms which are shifted with respect to each other ideally by 3/8 [0001] (figure 1.1. (a)). The zinc-blende structure, also called sphalerite, shows a cubic symmetry, consisting of two interpenetrating face-centered cubic sublattices. One sublattice is shifted with respect to the other by ¼ [111] (figure 1.1. (b)). The rock salt structure, with a cubic symmetry where the two atom types form two interpenetrating face-centered cubic lattices, is the rarest configuration, appearing when crystals are synthesized under high pressure.

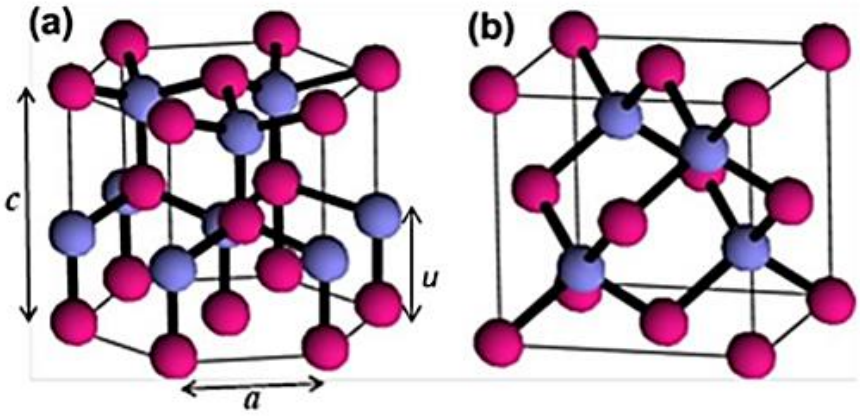

Figure 1.1: Schematic representation of (a) the wurtzite and (b) zinc-blende structures. The pink and violet spheres indicate metal and N atoms, respectively

In this work, we focus on III-nitrides with wurtzite structure, which is the thermodynamically more stable configuration. We have used GaN as a reference for the discussion, unless described otherwise. Figure 1.1 (a) shows the a and c parameters of the hexagonal crystal structure of III-nitrides, and the anion-cation bond length u along the [0001] axis. A four index (h k i l) notation is used to refer to crystallographic planes or axis, which are described as a function of three base vectors *a1*, *a2*, *a3* and the out-of-plane vector *c*, as presented in Figure 1.2. Note that $i = -h-k$, since the three base vectors are separated by an angle of 120°.

The family of basal planes is termed as {0001} c-plane. The c-plane orientation is the most commonly used in opto- and microelectronics. There are two other families of planes which are of high importance, namely the {1-100} m-plane and {11-20} a-plane, both perpendicular to the c-plane and containing an equal number of Ga and N atoms. These main crystal plane orientations in GaN are illustrated in figure 1.2.

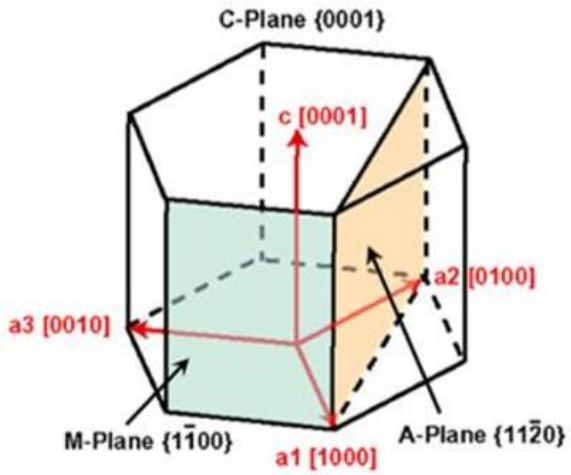

Figure 1.2: Hexagonal structure of GaN with representations of the base vectors and main crystallographic planes.

Since the hexagonal lattice is not centrosymmetric, the [0001] and [000-1] directions are not equal. In the GaN bond perpendicular to the {0001} plane, the vector pointing from Ga to N is identified arbitrarily as the [0001] direction. If the material is grown along this direction, then it is called Ga-polar if it is grown in the opposite direction then it is called N-polar.

In an ideal wurtzite crystal, the c/a and u/c ratios are 1.633 and 0.375, respectively. However, due to the difference in metal ions, the bond lengths and the resultant c/a ratios of AlN, GaN, and InN are different. Table 1.1 describes the lattice parameters of wurtzite III-nitrides at 300 K.

	InN [69]	**GaN [69,70]**	**AlN [69,70]**
c (Å)	5.703	5.185	4.982
a (Å)	3.545	3.189	3.112
c/a	1.608	1.626	1.6
u/c	0.377	0.377	0.382

Table 1.1: Lattice parameters of bulk InN, GaN and AlN.

The lattice parameters of nitride-based alloys are usually supposed to vary linearly with composition following the Vegard's law [Vegard, 1921]:

$$a\ (A_xB_{1-x}N) = x * a(AN) + (1-x) * a(BN) \quad (1.1)$$

$$c(A_xB_{1-x}N) = x * c(AN) + (1-x) * a(BN) \quad (1.2)$$

The knowledge of heteroepitaxy along the c-plane is well established. However, the growth in m- and a-plane orientations was not considered until recently due to the unavailability of suitable substrates. During the last decade, the realization of the importance of non-polar III-nitrides have first led to the fabrication of non-polar films/templates on foreign substrates. Few examples include a-plane GaN on r-plane sapphire substrates [71], or m-plane GaN on m-plane SiC [72]. However, the heteroepitaxial growth on *a* and m-plane layers is prone to high defect densities. More recently, halide vapor phase epitaxy (HVPE) has developed to the point of producing relatively thick (< 1 μm) GaN crystals along the [0001] direction [73], which can be diced into high-quality *a*- and *m*-plane platelets for epitaxy of nonpolar structures. The main drawback of this method, as of now, is the high cost involved and the limited surface area available for growth.

1.2 Crystal polarity

The group III nitrides are not centrosymmetric crystal structures, as a result, the two crystallographic directions [0001] and [000$\bar{1}$] are not equivalent. Conventionally, the [0001] polarity is defin ed by the direction of the vector associated to the metal (Al/Ga/In)- nitrogen(N) bond as shown in Figure 1.3. The epitaxial layer grown along this direction is called metal polar and the material grown in the opposite direction is called nitrogen polar. Hence the metal polar and nitrogen polar structures are the mirror images to each other. The two different polar materials possess distinct properties in terms of surface morphology, chemical reactivity, thermal stability and even the growth conditions. For instance, metal-polarity surfaces are more chemically stable than nitrogen polarity surfaces [74,75].

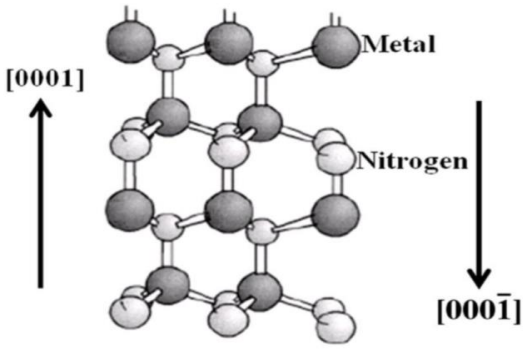

Figure 1. 3. Polarity in Group III nitride: Metal polar along [0001] and Nitrogen polar along [000$\bar{1}$] [76].

The realization of the two polarities of this Group III nitride system i.e. metal polar or N-polar, is especially sensitive to the chosen substrate material and the applied growth technique as well [77]. The polarity of the films can be probed by various techniques like wet chemical etching, electron microscopic techniques such as Convergent Beam Electron Diffraction (CBED) patterns, Co-Axial Impact Collision Ion Scattering Spectroscopy (CAICISS) and recently hydrogen irradiation has been proposed to effectively determine the polarity [74].

1.2.1 Dislocations

Dislocations are linear defects which arise from the imperfections in the crystalline structure. A material system is often prone to have dislocations irrespective of homo or hetero epitaxy. These dislocations are generated to relax the stress which arises during the growth and to decrease the global energy of the material system. These dislocations can strongly affect the device performance [78,79]. The origin of dislocations is the difference of lattice parameters and thermal expansion coefficients of the substrate and the epilayer. The dislocations are characterized by their Burgers vector ($\vec{b}$) and dislocation line ($\vec{u}$). In group III nitride epitaxy, the most common dislocations are Threading Dislocations (TDs) [80,81] generated at the interface of the substrate and propagating up to the surface of the layer. A dislocation can either be perfect or partial. A dislocation is said to be perfect, when its Burgers vector corresponds to an entire translation of the lattice; it is partial when the Burgers vector is a fraction of a translation of the lattice. In nitride layers grown along c, the main defects are TDs (shown in table 1.2), which forms as edge, screw or mixed type and are distinguished by the angle made between the burgers vector and the dislocation line.

(1) For a pure edge type dislocation, the dislocation line is perpendicular to Burgers vector ($\vec{b}$). A schematic diagram of atomic planes can be used to illustrate lattice defects such as dislocations. The "extra half-plane" concept of an edge type dislocation is shown in Figure1.4.

(2) For a screw type dislocation, the dislocation line is parallel to Burgers vector as shown in Figure 1.4.

(3) For a mixed type dislocation, there does not exist a particular well defined angular relationship between the dislocation line and the Burgers vector.

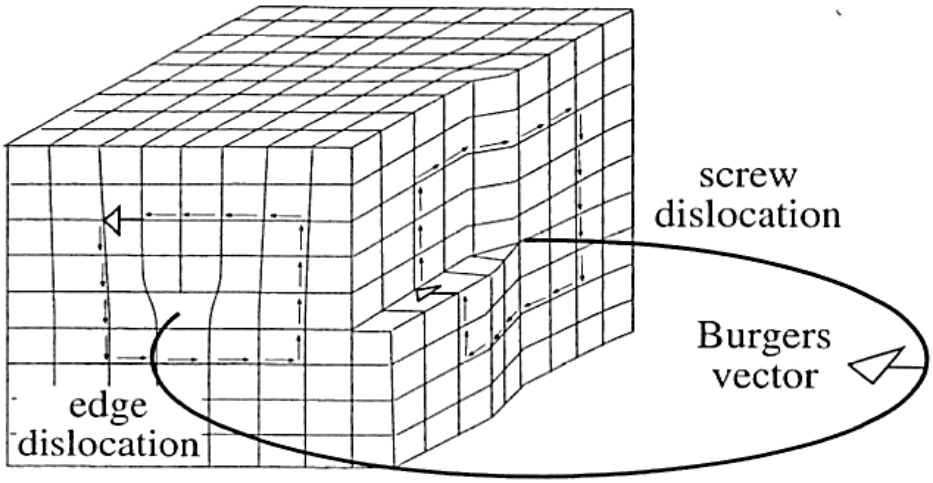

Figure 1.4. A schematic diagram showing, edge and screw dislocation [82].

Burger vector ($\vec{b}$)	Type of dislocation	Character
1/3 < 11$\bar{2}$0 >	Edge type *(a)*	Perfect
< 0001 >	Screw type *(c)*	Perfect
1/3 < 11$\bar{2}$3 >	Mixed type *(a+c)*	Perfect
1/3 < 1$\bar{1}$00 >		Shockley partial
1/6 < 20$\bar{2}$3 >		Frank-Shockley partial
1/2 < 0001 >		Frank partial

Table 1.2. Perfect and partial dislocations in group III nitride layers, with lines along [0001] direction [79,80].

1.2.2 Elastic properties

Strain is introduced during the epitaxial growth because of the mismatch of lattice constants and thermal expansion coefficients with the substrate. Strain affects the optical, electrical and bandgap properties of the III-nitrides.

In the framework of linear elasticity, Hooke's law describes the relation between the stress (σ_{ij}): applied to a material and the strain (ε_{kl}):

$$\sigma_{ij} = \sum C_{ijkl}\, \varepsilon_{kl} \tag{1.3}$$

where (C_{ijkl}) is the fourth-order elastic tensor. For simplification, we introduce the indices {1,2,3,4,5,6}, which replace the pairs of indices $\{xx, yy, zz, yz, zx, xy\}$:

$$\varepsilon_1 = \varepsilon_{xx} \;\; ; \;\; \varepsilon_2 = \varepsilon_{yy} \;\; ; \;\; \varepsilon_3 = \varepsilon_{zz}$$

$$\varepsilon_4 = \varepsilon_{yz}\,, \varepsilon_{zy} \;\; ; \;\; \varepsilon_5 = \varepsilon_{zx}\,, \varepsilon_{xz} \;\; ; \;\; \varepsilon_6 = \varepsilon_{xy}\,, \varepsilon_{yx}$$

The elastic module can be represented by a matrix (a second-order tensor). For a crystal of hexagonal symmetry, this matrix contains six elastic modules, of which five are independent, as given in equation (1.4):

$$\mathrm{C}_{ij} = \begin{pmatrix} c_{11} & c_{12} & c_{13} & & & \\ c_{12} & c_{11} & c_{13} & & & \\ c_{13} & c_{13} & c_{33} & & & \\ & & & c_{44} & & \\ & & & & c_{44} & \\ & & & & & \frac{1}{2}(c_{11}-c_{12}) \end{pmatrix} \tag{1.4}$$

The values of the parameters C_{ij} for GaN and AlN are summarized in **table 1.3**.

	c_{11}	c_{12}	c_{13}	c_{33}	c_{44}	References
GaN	374	106	70	379	101	[85] exp.
	390	145	106	398	105	[86] exp.
	365	135	114	381	109	[87] exp.
	370	145	110	390	90	[88] exp.
	396	144	100	392	91	[83] theory
	367	135	103	405	95	[84] theory
AlN	411	149	99	389	125	[89] exp.
	410	140	100	390	120	[88] exp.
	398	140	127	382	96	[83] theory
	396	137	108	373	116	[84] theory

Table 1.3: Experimental and theoretical stiffness constants of GaN and AlN in GPa

During heteroepitaxy of thin films of III-nitrides on the (0001) plane, the in-plane stress is uniform ($\sigma_{11} = \sigma_{22} = \sigma$) and there is no stress along the c axis or shear stress (biaxial stress configuration). In this case, the Hooke law is simplified as in **equation (1.5).**

$$\begin{pmatrix} \sigma \\ \sigma \\ 0 \end{pmatrix} = \begin{pmatrix} C_{11} & C_{12} & C_{13} \\ C_{12} & C_{11} & C_{13} \\ C_{13} & C_{13} & C_{33} \end{pmatrix} \begin{pmatrix} \varepsilon_1 \\ \varepsilon_2 \\ \varepsilon_3 \end{pmatrix} \tag{1.5}$$

Therefore, in such a situation, the strain components ε_1 and ε_2 are equal and their value is given by:

$$\varepsilon_1 = \varepsilon_2 = \varepsilon_{xx} = -(a_{epi} - a_{sub})/a_{sub} \tag{1.6}$$

where a_{epi} and a_{sub} are the lattice constants of the epilayer and the substrate, respectively. The biaxial strain induces a strain ε_3 of opposite sign along the [0001] axis perpendicular to the surface given by:

$$\varepsilon_3 = \varepsilon_{zz} = -2(C_{13}/C_{33})\varepsilon_{xx} \tag{1.7}$$

1.3 Spontaneous and piezoelectric polarization

A good understanding of the electrical polarization effects at the material interfaces is key to proper device simulation. III-V nitrides are the only III-V materials that show spontaneous polarization P_{SP}. This has been found to increase from GaN over InN to AlN [90] and it also has a negative sign. The reason is an intrinsic asymmetry of the bonding in the equilibrium wurtzite crystal structure. However, mechanical stress also results in polarization, which is then called piezoelectric polarization P_{PZ}. It is negative for tensile and positive for compressive strained AlGaN layers. Therefore, the orientation of the spontaneous and piezoelectric polarization is parallel in case of tensile strain and antiparallel in case of compressive strain. AlGaN layers grown on GaN buffers are always under tensile strain, thus only this case will be further discussed. As both polarizations have the same direction the total polarization is simply the sum:

$$P = P_{PZ} + P_{SP} \tag{1.8}$$

Further, the total polarization of the AlGaN layer is stronger than that of the underlying relaxed GaN buffer layer. The negative spontaneous polarization of both layers and the negative

piezoelectric polarization vector under tensile strain points from the Nitrogen atom towards the nearest Gallium atom along the [0001] axis. Thus, for Ga-faced polarity crystals the total polarization is directed towards the substrate, while for N-faced crystals it is directed towards the surface. It is found that the polarization-induced sheet charge is positive for AlGaN on top of GaN with Ga-face polarity and GaN on top of AlGaN with N-face polarity.

In the following the polarization induced charge at an AlGaN/GaN interface is calculated. Using the provided parameters and the same approach, the polarization for different material interfaces can be determined accordingly.

The spontaneous polarization P_{SP} at the AlGaN/GaN interface is calculated by [91]:

$$P_{SP} = P_{SP,AlN} + P_{SP,GaN}(1 - x) \tag{1.9}$$

	GaN	AlN	InN	References
$\boldsymbol{P_{SP}}$	-0.029	-0.081	-0.032	[90]
$\boldsymbol{P_{SP}}$	-0.034	-0.090	-0.042	[92]

Table 1.4: Spontaneous polarization parameters [C/m^2]

The piezoelectric polarization P_{PZ} is calculated by:

$$P_{PZ} = 2.\frac{a-a_0}{a_0}\left(e_{13} - e_{33}.\frac{C_{13}}{C_{33}}\right) \tag{1.10}$$

without taking partial relaxation into account. The parameters a and a_0 are the lattice constants, e_{13} and e_{33} are the piezoelectric coefficients, and C_{13} and C_{33} denote the elastic constants. The parameter values for both the spontaneous (**Table 1.4**) and piezoelectric (**Table 1.5**) polarization are achieved by the revised calculations of [92].

Material	a	a_0	e_{13}	e_{33}	C_{13}	C_{33}
	[Å]	[Å]	[C/m^2]	[C/m^2]	[Gpa]	[Gpa]
GaN	3.197	5.210	-0.37	0.67	68	354
AlN	3.108	4.983	-0.62	1.50	94	377
InN	4.580	5.792	-0.45	0.81	70	205

Table 1.5: Piezoelectric polarization parameters

Using the provided method and the listed values, the polarization induced charges for AlGaN/GaN, InAlN/GaN, and InGaN/GaN interfaces are calculated and shown in **Fig. 1.5**. While using slightly different values than Ambacher *et al.* [91], the results are in a good agreement. Furthermore, the significantly larger charges at the InAlN/GaN interface must be noted (due to the higher spontaneous polarization in AlN).

The dependence of the spontaneous polarization coefficients for GaN, AlN, and InN on temperature has been measured to be minimal [93,94]. There are no reports on the temperature dependence of the piezoelectric polarization.

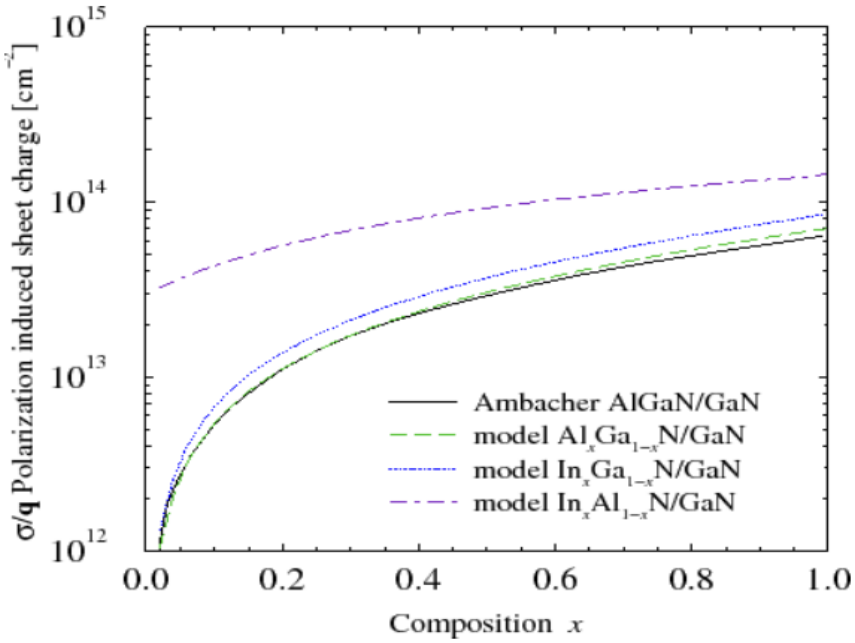

Figure 1.5: Piezoelectric and spontaneous polarization-induced charge $\sigma/q(P_{SP} + P_{PE})$ as function of the Aluminium molar fraction x

1.4 Energy diagram

1.4.1 direct bandgap semiconductors energy diagram

The understanding of the basic semiconductor material properties helps in interpreting the behaviour of the mode-locked laser diodes and designing the optimum devices. The direct bandgap III-V compound semiconductor materials were extensively studied for the development of efficient semiconductor lasers. The GaN, InN and AlN direct band gap materials are usually preferred as a substrate thanks to their better lattice matching to both ternary (e.g: AlGN) and quaternary (e.g: InAlGaN) compounds [95].

For a direct bandgap bulk semiconductor material, a typical energy versus wave vector (E-k) diagram is illustrated in **Figure 1.6**, which consists of a conduction band and three valence bands referred to as; heavy hole, light hole and the split-off band [96]. If the bottom of the conduction band and top of the valence band occur at the same value of the wave vector k, then the energy of the electron E_e and hole E_h are represented by the following parabolic functions [97].

$$E_e = E_c + \frac{\hbar^2 k^2}{2m_e^*} \tag{1.11}$$

$$E_h = E_v - \frac{\hbar^2 k^2}{2m_h^*} \tag{1.12}$$

Where $E_{c,v}$ are the conduction and valence band energies, $m_{e,h}^*$ are the effective masses of electrons and holes respectively, and k is the wave vector .

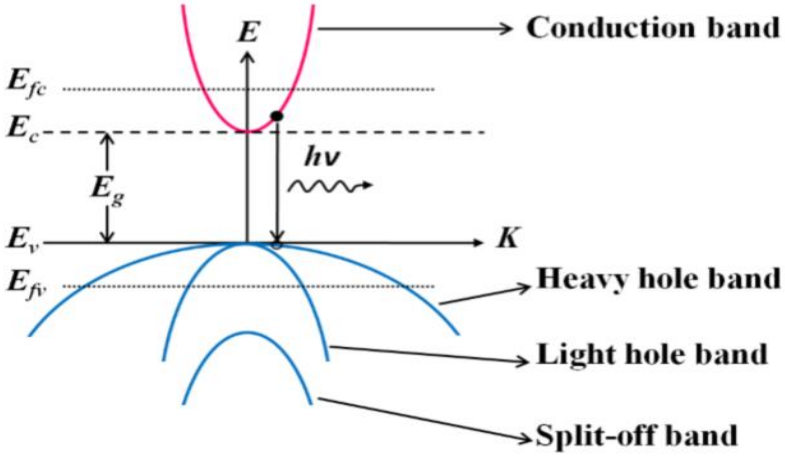

Figure 1.6: Schematic of a band model of a III-V semiconductor material with a direct bandgap [96]

1.4.2 band structure of III-nitride material

The band structure of a semiconductor emerges as a solution of the Schrödinger equation of non-interacting electrons in the periodic lattice. Visualization of the bandgap requires a plot of energy vs. wavevector *k = (kx, ky, kz)*. It is common to plot band structures as curves of $E_n(k)$ for values of k along straight lines connecting symmetry points in the k-space. These points of symmetry occur in the first Brillouin zone and are labelled as Γ, Δ, Λ, Σ. The bandgap is described as the energy difference between the bottom of the conduction band and the top of

the valence band. If the bottom of the conduction band and top of the valence band occur at the same symmetry point, then the material is said to have a direct bandgap. In the case of wurtzite III-nitrides, the bandgap is direct, with the conduction band minimum and the valence band maximum located at the Γ point. Due to the asymmetric nature of the wurtzite structure the valence band degeneracy is lifted. Thus the heavy hole (HH), light hole (LH) and spin-orbit, crystal field splitting (CH) subbands are separated as shown in the **figure 1.7**. The top of HH and LH subbands are higher than CH subband in energy for GaN. However, in the case of AlN the top of the CH subband is at higher energy than the HH or LH subbands.

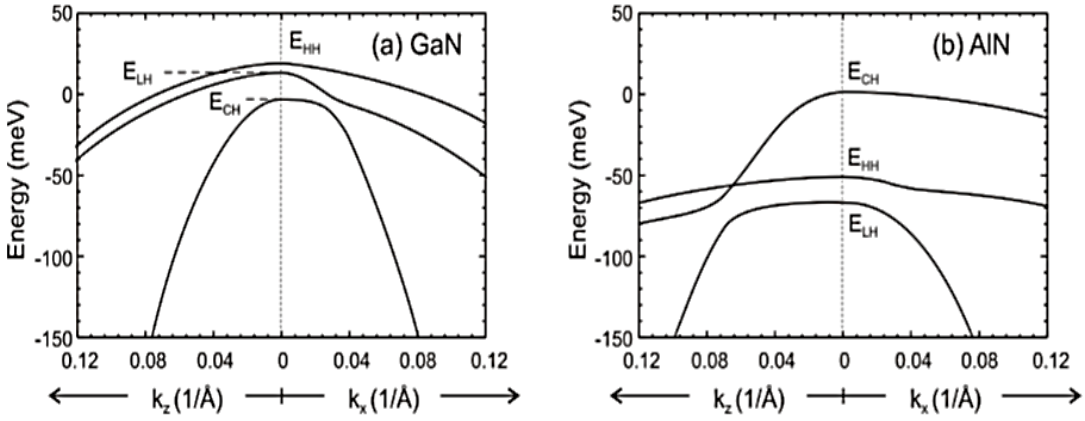

Figure 1.7: Electronic structure of the valance band of (a) GaN and (b) AlN near the Brillouin zone centre point Γ (for unstrained wurtzite material. For simplicity, zero energy is assigned to the top of the valence band)

The values of the bandgap of GaN, AlN and InN are summarized in **table 1.6**. An effective mass approximation can be utilized to describe the band structure at Γ(k=0) by assuming a parabolic band structure at this point. This means that the electron or hole behaviour can be modelled as a free particle with an effective mass m^* experiencing a fixed potential. Typical values of the effective masses for electrons and holes in III-nitrides are recorded in **table 1.6**.

For ternary compounds like AlGaN or InGaN the bandgap is approximated by a quadratic equation [98-100]:

$$E_g(AB) = xE_g(A) + (1-x)E_g(B) - x(1-x)b \qquad (1.13)$$

where b is the bowing parameter, which accounts for the deviation from a linear interpolation between the two binaries A and B. The bowing parameter has a value of 0.8-1.3 eV in the case

of AlGaN [101 54]. By changing the Al or In content in GaN it is hence possible to obtain alloys with desirable bandgap.

	GaN	AlN
E_g (T = 0 k) (eV)	3.507 [102]	6.23 [102]
α_V (meV/k)	0.909 [102]	1.999 [102]
β_D(k)	830 [102]	1429 [102]
m_e^*	0.2 m_0 [103]	(0.32-0.40) m_0 [102,104]
m_h^*	1.25 m_0 [105]	1.44 m_0 [106]

Table 1.6: Band parameters of GaN and AlN: bandgap energy at T = 0 K; Varshni parameters; electron and hole effective masses (m_0 being the nominal mass in vacuum).

The bandgap of these materials is temperature dependent due to electron-lattice interactions and temperature dependence of the lattice parameters [107,108]. The temperature variation of the bandgap can be estimated by using the Varshni equation:

$$E_g(T) = E_g - \left(\frac{\alpha_V T^2}{\beta_D + T}\right) \qquad (1.14)$$

where α_V and β_D are the Varshni and Debye coefficients respectively, whose values for GaN and AlN are listed in **Table 1.6**.

The two GaN polytypes, like most III-V materials, have a direct band gap at the Γ point, the center of the Brillouin zone (k = 0).

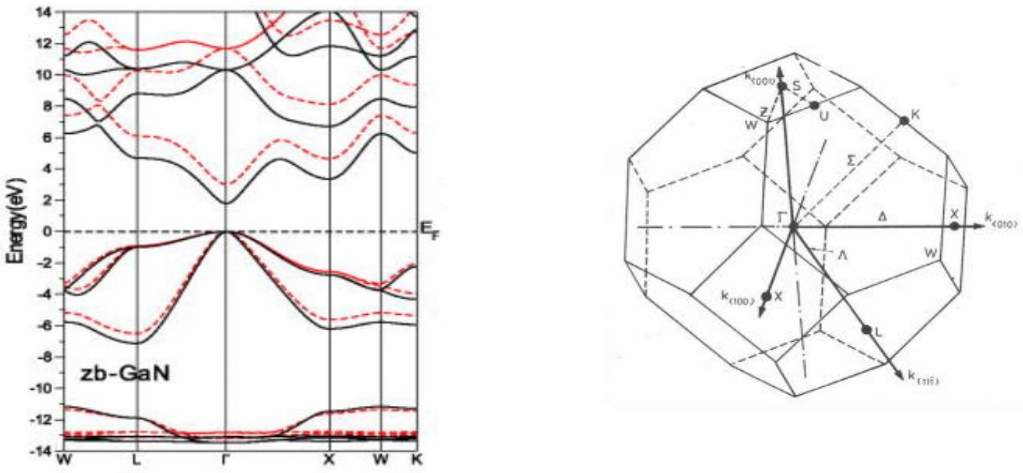

Figure 1.8. a) Zinc blende GaN band structure [109]

b) first Brillouin zone of cubic GaN lattice [110]

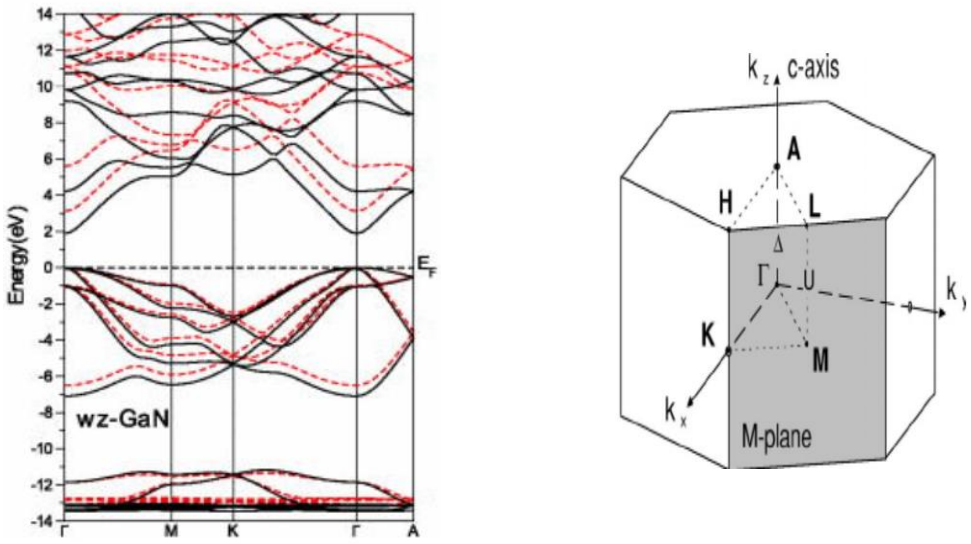

Figure 1.9. a) Wurtzite GaN band structure [109]

b) first Brillouin zone of hexagonal GaN lattice [110].

1.5 Degeneracy of the valence band at the Γ point

In the cubic lattice structure, at the Γ point (the area of radiative transitions) the spin-orbit coupling divide the upper part of the valence band into two levels, the first one corresponds to the heavy holes band et light holes band, however the second, shifted by Δ_{SO} (spin-orbit coupling), corresponds to the spin-orbit holes, degenerated at Γ.

In the case of the hexagonal GaN, the non-cubic form gives rise to an electric field called crystal field Δ_{cr} which induces a rise in degeneracy at the Γ point of the heavy and light holes.

		Hexagonal	Cubic
Δ_{SO} (meV)	Theoretical	14	20
	Experimental	8	17
Δ_{cr} (meV)	Theoretical	34.3	0
	Experimental	39	0

Table 1.7 Theoretical and experimental values of Δ_{SO} and Δ_{cr} for the Cubic and hexagonal GaN [111-113]

1.6 Carriers effective masses

The effective masses of the carriers, proportional to the inverse of the band curves, are reported in **table 1.8**. In the case of direct band gap semiconductors, the electron effective masses changes slowly with the considered crystallographic direction.

	h-GaN	c-GaN
m_e^* (Electrons effective mass)	$0{,}22.m_0$	$0{,}13.\ m_0$
m_{hh}^* (Heavy holes effective mass)	$2{,}10.\ m_0$	$1{,}30.\ m_0$
m_{lh}^* (Light holes effective mass)	$0{,}30.\ m_0$	$0{,}19.\ m_0$
m_{SO}^* (Spin-orbit effective mass)	$0{,}60.\ m_0$	$0{,}60.\ m_0$

Where: m_0 is the free electron mass

Table 1.8 Carriers effective masses of GaN at T=300°k [111,114]

1.7 c-GaN and h-GaN polytypes

Wurtzite GaN	Zinc-blende GaN
Direct band gap at Γ point (k=0)	Direct band gap at Γ point (k=0)
The crystal field induces a rise in degeneracy of heavy and light holes at Γ point.	The spin-orbit coupling divide the upper part of the valence band into two levels. The first corresponds to the heavy and light holes bands, however the second, shifted by $\Delta_{SO,}$ corresponds to spin-orbit band.
The mass of heavy holes located at the highest level of the valence band is high. **[115]**	The mass of heavy holes located at the highest level of the valence band is low. **[115]**
The p-type doping: limited at 10^{17} cm^{-3} **[116]**	The p-type doping: limited at 5.10^{18} cm^{-3} **[116]**
The density of dislocations is very high 10^{10} cm^{-2}. To reduce it to 10^7 cm^{-2}, the ELOG method "epitaxially lateral overgrown" has to be used, but it very expensive. **[117,111,118]**	The dislocations propagate along (111) direction of the Gallium nitride. The cross section of two of these defects may annihilate them. However, the crystal quality is ameliorated far from the substrate. **[111]**
The instability of ht InGaN alloy decomposes into rich and low Indium zones in quantum wells	The narrower band gap leads to accessibility of visible wavelengths using the Indium with lesser percentage.

The existence of the piezoelectric fields separates the carriers, which leach to a diminution of the gain **[119]** et a widening of the emission lines.	The piezoelectric fields do not exist
Absence of solid GaN, stable.	Absence of solid GaN, metastable.**[120]**
The difficulty of creation of the laser cavity	The crystal cleaves more easily, which facilitates the creation of the laser cavity. **[119]**

Table 1.9: Comparison between c-GaN and h-GaN polytypes

1.8 Crystal structure and properties of AlN

1.8.1 Crystal structure

The crystal parameters of the hexagonal and cubic structures at 300 °K are represented in **table 1.10 [112]**

Crystal structure	Hexagonal	Cubic
Lattice constant (At 300 °K)	a=3.096 A° c=4.959 A°	a=4.353 A°

Table 1.10: Crystal parameters of h-AlN and c-AlN structures

1.8.2 Band structures

The AlN cubic and hexagonal band structures and their parameters are represented as follows:

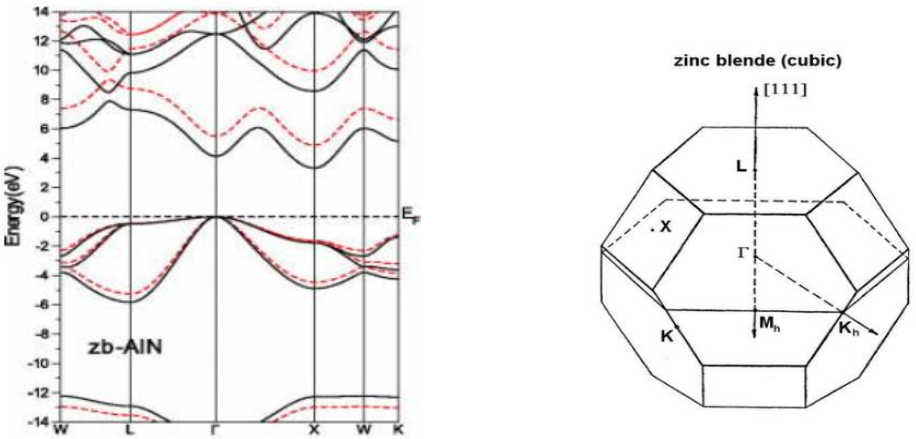

Figure 1.10. a) Zinc-blende AlN band structure [109]

b) first Brillouin zone of hexagonal AlN lattice [121].

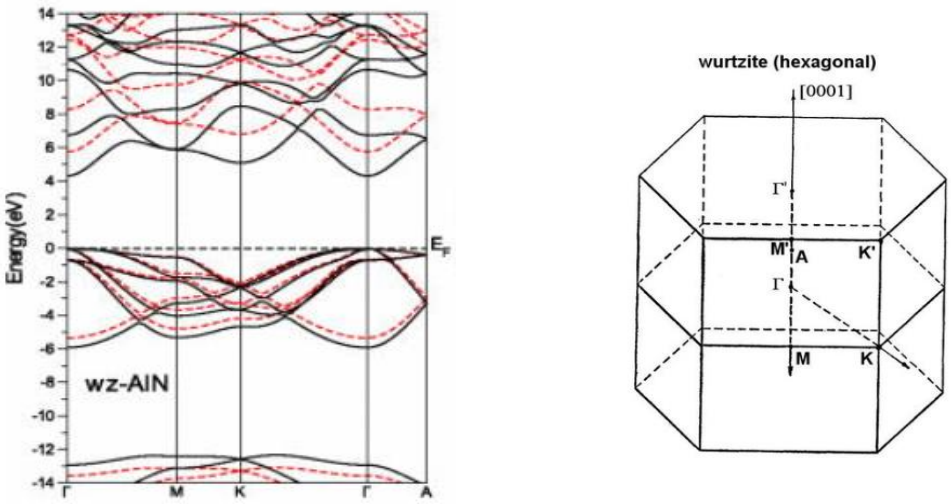

Figure 1.11. a) Wurtzite AlN band structure [109]

b) first Brillouin zone of hexagonal AlN lattice [121].

		h-AlN	c-AlN
Δ_{SO} (meV)	Theoretical	11	19
	Experimental	19	17
Δ_{cr} (meV)	Theoretical	-217	0
	Experimental	-200	0

Table 1.11 Theoretical and experimental values of Δ_{SO} and Δ_{cr} for the c-AlN and h-AlN [111-113]

1.8.3 Carriers effective masses

	h-GaN	c-GaN
m_e^* (Electrons effective mass)	0,30.m_0	0,25. m_0
m_{hh}^* (Heavy holes effective mass)	1,40. m_0	2,58. m_0
m_{lh}^* (Light holes effective mass)	0,30. m_0	0,26. m_0
m_{SO}^* (Spin-orbit effective mass)	0,25. m_0	0,23. m_0

Table 1.12 Carriers effective masses of AlN at T=300°k [111,114]

R. F. Davis of University of North Carolina developed the first cubic AlN layer on 3C-SIC substrate in 1989.

1.9 Overview of deposition of GaN and AlN layers

GaN was one of important choice for material in III–nitride compound semiconductors[122]. In first report, metal gallium and ammonia was reacted to produce a GaN material in the form of small needles and platelets [123]. GaN grown on sapphire substrate using Hydride Vapour Phase Epitaxy (HVPE) method was demonstrated by Maruska after three decades[124].

It was a high background electron concentrations (~10^{8}-10^{20} cm^{-3}) and poor crystallinity of epilayers on non-native substrate.

Yoshida et al. has demonstrated that when AlN is deposited on GaN layer electrical and luminescent properties improved [125]. Further, AlN nucleation layer or GaN nucleation layer grown at low temperatures 500 °C - 750 °C prior to the growth of high temperature GaN epilayers [126,127] improved the top layer. GaN growth mode consists of three-dimensional (3D) islands to two-dimensional (2D) growth mode leading to smooth and flat GaN epilayer.

Success of p-type doping in GaN was another breakthrough in the history [128,129]. The first nitride LED suffered from very low efficiency because of an insulating layer [130]. The major difficulty was solved when Akasaki [131] discovered that electron beam annealing could activate magnesium doped GaN and create a p-type material.

To start with a p-type doping in GaN, the first LED was fabricated in less than three years. Then, there has been constant development, especially after the ground breaking discoveries concerning growth and p-type doping activation of GaN and fabrication of blue light emitting diodes won the 2014 year Nobel Prize in Physics.

Discovery of InN bandgap was 0.7 eV [132-134] instead of previously thought 1.9 eV in III–nitride compound semiconductors [135].

However, GaN based alloys have been grown hetero-epitaxially due to the lack of native GaN substrates: usually on Si, SiC and sapphire. The problems associated with the large lattice mismatch, wetting of the substrate and different thermal expansion coefficients, resulted in structural defects in epilayers. These defects propagate to the surface along the growth direction. The forbidden energy bandgap of the GaN defective epilayer can act as

scattering and recombination centers. This reduces life time and quality of fabricated optical and electronic devices.

Low-temperature nucleation layer enhances the wetting of the substrate and suppress the growth islands [136]. Another alternative approach is Epitaxial Lateral Overgrowth (ELO) method [137]. The GaN substrate was etched in columns, after the etching, dielectric material was masked as a columnar array. Thereafter, GaN growth proceeds laterally and vertically from the columns. Eventually GaN defect-free layer grows over the top of the mask to create continuous layers. Hence different methods were attempted to reduce defects in epilayer.

Research efforts were made to improve quality of GaN epilayer and reduce defect densities in materials. These materials were used in instrumental to build several optoelectronic devices. For example, GaN layer has been grown by ELO method with dislocation density in orders of 10^{10} to 10^{6} cm^{-3}.

Nitride based laser diodes working at room temperature with a life time exceeding over 10,000 h have been demonstrated [138]. Nevertheless, the availability of single crystal GaN substrates is still highly desirable, which would lead to better device quality and reliability, longer device lifetime, and better affordability.

Group III-nitride based crystalline materials have attracted extensive research interest in theoretical and experimental research due to their fundamental and physical properties. For the development source materials for single crystals, GaN powder was commercially synthesized via reaction of Ga2O3 with NH3; with high concentration of oxygen as impurity. This oxygen concentration appears with dislocations in GaN single crystals and inhibits continuous growth. Further AlGaN nanocrystalline powder has been synthesized by pyrolysis route [139].

GaN nanowires have been used for label-free dual sensing of DNA molecules [140]. Localized charge transfer process and surface band bending in methane have used in GaN nanowires for sensors [141]. Photosynthesis has been demonstrated by CO2 reduction into CH4 and CO using 1D GaN nanowires [142]. Metal gallium is extremely expensive and commercially synthesis of GaN powders has low yield. GaN powder has been synthesized by various methods reported by research groups. Vacuum-Ultraviolet-Sensitive (λ<200 nm) photodetector with fast response speed based on high-quality AlN micro/nanowire has been demonstrated earlier [143]. Hence simple and inexpensive chemical method to produce GaN, AlGaN nanocrystalline and 1D III-nitrides semiconductor nanostructure is in current interest [144].

1.10 Group III nitrides epitaxy

The common growth techniques for III nitrides are Molecular beam epitaxy (MBE), Metal organic Vapor Phase epitaxy (MOVPE), Hydride Vapor Phase epitaxy (HVPE), Sputtering and Pulsed Laser Deposition (PLD). Among them MOVPE and MBE are the most used for device processing and we have employed these techniques to grow the samples which are investigated in this work.

The quality of epitaxial layers depends upon the growth technique, the epitaxial growth mode (homoepitaxial or heteroepitaxial), the substrate used and the processing conditions. The choice of growth technique depends on the desired structure and needs, for example, in case of industrial production, MBE had less success for nitrides than MOVPE. For group III nitrides growth, although bulk GaN and AlN are available, the small size and high cost prevent their wide usage. Therefore, due to the current lack of affordable bulk nitride substrates, group III nitrides are grown by heteroepitaxy. However, a number of research groups and industries are currently pioneered in the growth of bulk nitride substrates. Lattice and thermal mismatch between epitaxial layers and substrates have long been the major challenge in obtaining high quality devices in the III-Nitride material system. The properties of the most commonly used substrates for group III nitrides are listed in Table 1.5, which indicates a large lattice and thermal mismatch between the III–nitrides and the substrates. Because of this mismatch the growth of good quality epilayers is challenging [145].

1.11 Substrates and buffer layers for group III nitrides

For epitaxial growth, one of the major issues is to select the suitable substrate. Generally, close matched substrates are used to reduce the film stress and dislocations in epitaxial films. There are many factors which contribute to select the substrates for group III nitride epitaxy, and no single material possesses all of the desired qualities. The foremost important factors are the lattice parameters and the thermal expansion coefficients of the substrate closely match with the epitaxial film. Furthermore, the substrates must be chemically and mechanically stable at high temperatures. A substrate should be easily available in large wafer size at relatively low cost in order to make production-scale devices. A high thermal conducting substrate increases device lifetime and allows devices to operate at higher power densities. For optoelectronic purposes, the substrate should have a wide band gap and a high refractive index, so that the photons generated in the active layers of the film are not absorbed

by the substrate. A number of substrates have been used for Group III nitrides epitaxy and a complete review was reported by Liu et al [146].

1.11.1 Sapphire substrate

Sapphire is the most extensively used substrate for growth of the III–nitrides despite of its large structural and thermal mismatch with GaN and InN. This is supported by the fact that the layers grown on sapphire have, in many cases, better quality and sapphire is easily available up to inches in diameter at relatively low cost. Sapphire substrates are transparent and stable at high temperatures. In general, the quality of the films grown directly (i.e., without the buffer layer) on any plane of sapphire is poor. Obtaining a good quality nitride epilayers necessitates the nitridation of sapphire substrates and an insertion of a low temperature intermediate buffer layer. Furthermore, the optical transparency of sapphire is beneficial in back illuminated detectors and LEDs for lack of absorption. The main drawback of sapphire as a substrate, is the low thermal conductivity, which causes heat management as an important concern for high current density devices [147].

1.11.2 Silicon carbide (SiC) substrate

Extensive work has been done on the growth of III– nitrides on SiC substrates [148,149]. SiC has several advantages over sapphire for InN and GaN epitaxy, which includes a smaller lattice mismatch and higher thermal conductivity. Additionally, SiC has good electrical conductivity which eases to make electrical contacts to the backside of the substrates and thereby simplifies the device structure compared to sapphire substrates. Large good quality SiC substrates are commercially available. Low temperature GaN or AlN buffer layers are also deposited on the SiC substrates before growing the nitrides. The stress developed in the films grown on SiC is smaller than that grown on sapphire, because of less lattice mismatch. SiC is also a polar material which facilitates the growth of single polar nitrides.

1.11.3 Silicon (Si) substrate

Generally, nitride-based devices are grown on sapphire, silicon carbide substrates. However, a considerable work has been done on the growth of group III nitrides on Si substrate. The major attractive points of Si as a substrate includes high quality, low cost, availability of large size, good electrical and thermal conductivity. In addition, Si substrate can accomplish the integration of III nitride devices with other Si based electronics. Although the crystal quality of GaN grown on Si is still poorer than that on sapphire and SiC, research on this is in great

progress. A low temperature buffer layer of AlN is usually grown on Si before the growth of the main epilayer to avoid the formation of Si_xN_y. The growth of a polar epilayer on nonpolar substrate is more complicated due to the formation of additional defects, such as inversion domains [145].

1.12 Growth methodologies of GaN and AlN

The growth of III-nitrides has occurred in a variety of instruments, each with their own particular benefits and drawbacks. **Table 1.13** lists the typical machines used to grow GaN and AlN, including metalorganic vapor phase epitaxy (MOVPE) / chemical vapor deposition (MOCVD), hydride vapor phase epitaxy (HVPE) [150], MBE and reactive sputtering.

Deposition Technique	Description	Ref
MOVPE/ MOCVD	- Precursors: Mixtures of trimethylindium, -gallium, or –aluminium ($(CH_3)_3M$), and NH3 - Growth temperature: 1000-1100°C [152-154] - Results: High growth rate (1-3 µm/h) and excellent material quality and control over layer thickness and doping	[151]
HVPE	- Precursors: GaCl, NH_3 [155] - Growth temperature: 1000-1050°C [130], [156-158] - Results: Very high growth rate (up to 100 µm/h). Possibility to synthesize mm-thick GaN crystal boules to slice free-standing wafers.	[159]
MBE	- Precursors: High purity metals and N_2 or NH_3 - Growth temperature: 700-800 - Results: very low growth rate, excellent control over layer composition. Can start and stop the growth of layers with atomic precision as well as the flux of a specific atom giving layer-by –layer control over the alloy concentration and thickness. Furthermore, in-situ reflection high-energy electron diffraction (RHEED) characterization greatly helps to characterize the growth. Gas-MBE also exists, which uses ammonia or hydrazine for the N-precursor.	[160]

Sputtering	- Precursors: High purity metals or III-nitride blanks and N2 - Growth temperature: 300-750°C - Results: lower crystal quality but deposition is possible in any substrate and in large surfaces. [161].	[161]

Table 1.13: List of methodologies used to grow GaN and AlN.

1.13 Doped GaN

Controlled doping in a broad range of concentrations in wide-bandgap semiconductors is very challenging for p-type varieties, as has been pointed out, for example, by Walukiewicz [152]. Simple substitution of elements such as C, Si, and Ge on the Ga sites and O, S, and Se on the N sites can potentially form shallow donors in GaN. Simple substitution of elements, such as Be, Mg, Ca, Zn, and Cd on the Ga sites and C, Si, and Ge on the N sites have the potential of forming relatively shallow acceptors in GaN. In practice, however, GaN n-typeis achieved by using Si, Ge, and Se, the latter being not that common. On the other hand, for p-type GaN only Mg has been successful but the level of hole concentration that can be achieved hit a ceiling of about 10^{18} cm^{-3}. Electronic and optoelectronic applications require n-type and p-type semiconductors. Even for high quality GaN, grown by the many different processes (MBE, CVD, and HVPE), is unintentionally n-type doped, a phenomenon that is attributed to native defects (i.e., points defects, dislocation, stacking fault, VN, antisites) and impurities (i.e., C, O, H) in GaN. Many potential p-type dopants attempted for incorporation into GaN cannot effectively compensate electrons in GaN and lead to p-type GaN. Hence, formation of p-type GaN is not straightforward. On the other hand, n-type doping of GaN is accomplished without major complications. This means that GaN p-type doping is the bottleneck to taking full advantage of the potential of GaN, especially in applications where both n-type GaN and p-type GaN are required, such as in optoelectronics.

The precursors, carrier gas, growth conditions, substrate material, among others, define the incorporation of impurities and imperfections in the crystal that result in the generation of defect-induced free carriers. Despite many decades of improvements in GaN technology, the residual electron concentration hovers around 1×10^{16} cm^{-3}. Unintentional impurities imply lack of control, which is undesirable. In the following subsections a succinct description of GaN n-type and p-type doping is presented [163].

1.13.1 n-type Doping

In unintentional GaN samples with a low n-type background, n-type doped GaN with Si is a very well founded practice for both MBE and MOCVD techniques [164]. Controllability of electron concentration~10^{17} to 2×10^{19} cm^{-3} by varying the SiH4 flow rate in MOCVD growth is possible [165]. With GeH4 an order of magnitude higher electron concentration beyond what is feasible by Si is possible.The Si ionization energy level in GaN is about 30meV (dilution limit) and decreases as the doping level increases due to screening [166]. PL measurements in average-quality GaN yield a binding energy value of 22meV [167]. Measurements on high-quality GaN layers grown on freestanding GaN wafers indicate (as determined by magneto-optical studies [168] and detailed analysis of the two-electron satellite transitions [169] a binding energy of 30,18 meV. Owing to the high solubility of Si (10^{20} cm^{-3}) in GaN, Si is suitable for group III nitride doping and it is the most frequently used. Carrier concentrations in Si-doped GaN in the range 10^{17}-10^{19} cm^{-3} were observed, when silane (SiH4) (used as an Si precursor) molar flow was varied 100 times. Also, Ge doping is well behaved. Ge solubility in GaN is in the range of 10^{17}-10^{19} cm^{-3} when germane (GeH4) (used as Ge precursor) molar flow was varied 100 times in MOCVD growth. Ge doping has produced materials with electron concentrations of 7×10^{16} - 10^{19} cm^{-3}. More recently, Wieneke et al. [170] reported electron concentrations above 10^{20} cm^{-3} in nonpolar a-plane GaN epilayers grown by MOVPE on r-plane sapphire substrates using isobutylgermane (IBGe) as a Ge precursor. A linear electron concentration versus molar flow relationship for both SiH4 and GeH4 precursors was observed [171,172]. However, Ge incorporation is less efficient (by one order of magnitude) than Si incorporation.

1.13.2 p-type Doping

As noted above, p-type doping in wide bandgap semiconductors is challenging and elusive, and nitrides are no exception. p-Type GaN, for the fabrication of p-n junction LEDs, was first achieved by Akasaki and Amano [173] in MOVPE-grown Mg-doped GaN. Doping activation was attained on Mg-doped GaN via low-energy electron-beam irradiation (LEEBI) treatment. The Hall measurement data showed a hole concentration of~ 2×10^{16} cm^{-3} with a mobility of~8 cm^2/ (V s) and a resistivity of~35 Ω cm at room temperature. Nakamura et al., with the same process that Amano used, obtained a hole concentration of $3\times10^{18}cm^{-3}$, a mobility of 9 cm^2/ (V s), and a resistivity of 0,2 Ω cm at room temperature [174]. Soon thereafter, Nakamura et al. developed a doping activation technique based on N_2-ambient thermal

annealing at temperatures above 700 °C. After the thermal treatment, the resistivity of Mg-doped GaN films dropped from 1×10^{6} to 2 Ω cm and the hole concentration and mobility were $3\times10^{17}cm^{-3}$ and 10 cm^2/ (V.s) [175]. Nowadays, thermal activation is one of the most widely used techniques to active Mg in GaN. The thermal process is reversible with the GaN reverting to an insulating compensated state when annealed under NH_3, where the decomposed hydrogen from NH_3 was thus considered as the critical compensating agent during the annealing process under the NH3 atmosphere. A great deal of effort has been addressed to p-dope GaN and its ternaries by incorporating group II and group IV elements. So far, no other dopant has been as successful as Mg in converting GaN, AlGaN, and InGaN, with low Al and In mole fractions, to p-type materials. Needless to say, p-type doping in GaN and its ternaries remains a topic of interest both in terms of technological aspects and also at the fundamental level. In the case of the chemical vapor phase epitaxy technique [176], CCp_2Mg and MCp_2Mg are utilized for the source of Mg. Experimental results indicate CCp_2Mg is less volatile and its incorporation in GaN is more efficient at high temperatures, where a better GaN quality compared with the quality of GaN grown at lower temperatures is attained. Mg concentrations in p-type GaN films may be extremely high:~1% of the host species. When substitutionally incorporated, only about 1% of the Mg atoms are ionized in GaN.

In Mg-doped GaN grown by MOCVD, the concentration of free holes at room temperature reaches its maximum value of about 10^{18} cm^{-3} for a Mg chemical concentration of about 3×10^{19} cm^{-3}, and it decreases with further increase of Mg concentration [177]. The activation energy of Mg acceptors in GaN and $Al_xGa_{1-x}N$ is in the range of 160-200 meV, which is larger than k_BT at 300K and increases with Al fraction [178-182]. As a result, low conductivity of holes in p-type GaN and p-type $Al_xGa_{1-x}N$ is observed, degrading the performance of light emitters.

Because of the relevance of GaN-based optoelectronic devices, studies conducted to better understand the process and realize highly conductive p-type GaN and AlGaN are in demand, especially for the case of high Al-composition p-type AlGaN. Results on Mg-doped p-type $Al_xGa_{1-x}N$ with low Al content $0 < x < 0:27$ are available in [183-186]. An activation energy as high as 310 meV was reported in [165] for x=0.27. Demonstration of p-type conductivity in Mg-doped $Al_xGa_{1-x}N$ (x=0.35) epilayers was reported by Yu et al. [187]. The influence of growth conditions on p-type conductivity was also investigated.

Researchers found that a proper V/III ratio and a relatively high growth rate were needed to improve the electrical characteristics of the p-type AlGaN epilayers. As a result of optimized growth conditions, a p-type resistivity of 3:5 Ω cm and a hole concentration of $> 5\times10^{17}$ cm^{-3} were attained. Unlike layers grown by MOCVD, MBE-grown p-type GaN layers do not require post-growth annealing, neither employing activated nitrogen nor employing ammonia as the nitrogen source [188]. Mg-doped GaN layers grown by RMBE with ammonia as the nitrogen source exhibit p-type conductivity without any post-growth treatment [189], which is very advantageous. In the case of GaN growth by MBE, Mg incorporation depends on the stoichiometry, the polarity of the growing surface [189,190], the substrate temperature, and the growth rate [191-193].

1.14 Doping of AlGaN

AlGaN alloys are studied extensively as contact layers of UV LEDs and laser diodes. For these applications, conductive AlGaN alloys with high Al content are necessary. Hence the role of dopants, impurities and defects in such systems have to be understood. Silicon (Si) is used for the n-type doping, but achieving highly conductive n-type $Al_xGa_{1-x}N$ for $x > 0.70$ is proven difficult. Beyond this threshold, a sharp increase in the donor activation energy [194-196] and resistivity [197] was observed. Carrier compensation by deep level defects, including deep Si DX centers, has often been speculated. DX centers are formed when a shallow donor impurity undergoes a large bond-rupturing displacement and becomes a deep acceptor by trapping electrons. This heavily drops the carriers available for conduction. Different calculations support that Si forms a deep DX center in $Al_xGa_{1-x}N$ [198-201]. Thus, Park and Chadi [200] predicted the onset of DX behavior for Si to occur at $x > 0.24$, whereas Boguslawski and Bernholc [198] predicted that Si-related DX centers are stable at $x > 0.60$, and Gordon et al. [199] obtained an onset of DX transition for $x = 0.94$. Experimental results are also contradictory, e.g. some studies suggested Si to be a DX center in $Al_xGa_{1-x}N$ for $x > 0.5$ [202], others for $x \geq 0.84$ [203], and some show indications of self-compensation for high doping levels ($[Si] > 3\times10^{19}$ cm^{-3}) for $x \geq 0.42$ [204].

Ge doping was possible in GaN as it was a shallow donor like Si. However, there is very little information about its behaviour in AlxGa1-xN. Gordon et al. [199] predicted the onset of the DX transition for Ge in AlGaN at $x = 0.52$. However, to our knowledge, there were no experimental studies of Ge doping of AlGaN. In view of the results obtained for GaN, it was interesting to explore its behaviour in the ternary alloy.

CHAPTER 2

THEORY OF III-NITRIDE-BASED SEMICONDUCTOR LASERS

CHAPTER 2

2.1 Theory of semiconductor lasers

2.1.1 A brief history of semiconductor lasers

Semiconductor lasers [205,206] contain a zone (mostly called the active layer) that has gain if sufficiently pumped and that overlaps with an optical.

The term ‘L.A.S.E.R’ is an acronym for ‘light amplification by stimulated emission of radiation’. The amplification relies on stimulated emission, theoretically predicted by Einstein in 1917. The laser concept was first explored in the microwave wavelength region (1954, MASER using ammonia, Ch. H. Townes, Nobel prize 1964). The first optical laser (1958, US patent No. 2,929,922 awarded 1960, A.L. Schawlow, Ch.H. Townes) was the ruby laser developed in 1960 by Th. Maiman.

Lasers are distinguished from other light sources by their coherence. Spatial coherence is typically expressed through the output being a narrow beam, which is diffraction-limited. Laser beams can be focused to very tiny spots, achieving a very high irradiance, or they can have very low divergence in order to concentrate their power at a great distance. Temporal (or longitudinal) coherence implies a polarized wave at a single frequency, whose phase is correlated over a relatively great distance (the coherence length) along the beam.[207] A beam produced by a thermal or other incoherent light source has an instantaneous amplitude and phase that vary randomly with respect to time and position, thus having a short coherence length.

Lasers are characterized according to their wavelength in a vacuum. Most "single wavelength" lasers actually produce radiation in several modes with slightly different wavelengths. Although temporal coherence implies monochromaticity, there are lasers that emit a broad spectrum of light or emit different wavelengths of light simultaneously. Some lasers are not single spatial mode and have light beams that diverge more than is required by the diffraction limit. All such devices are classified as "lasers" based on their method of producing light, i.e., stimulated emission. Lasers are employed where light of the required spatial or temporal coherence cannot be produced using simpler technologies.

2.1.2 Laser applications

The fabrication of high quality LEDs paves the way for the realization of lasers which can operate at light wavelengths from ultraviolet (UV) to green. The blue ray disc technology has replaced the traditional DVDs as the blue laser diodes can allow five times higher storage capacity. A major breakthrough in research has been accomplished by the infrared lasing in high quality single crystalline InN nanobelts [208]. The possibility of making ternary and quaternary nitride systems fosters the semiconductor lasers emitting from deep UV to IR region.

The main applications of LDs address:

- Optical storage.
- Telecommunications.
- Solid-state laser pumping.
- Medical therapeutics.
- Image recording.
- Barcode scanning.
- Inspection, measurement and control.
- Material processing.
- Sensing.
- Basic research.

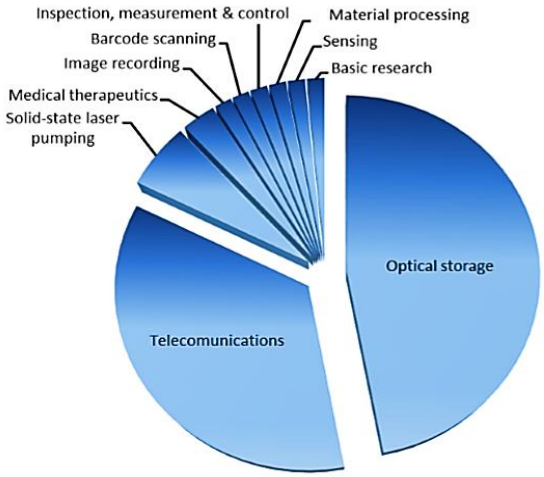

Figure 2.1: Main application of LDs [209,210]

Figure 2.1 shows the market repartition for the LDs applications. Optical storage is clearly the major segment followed by telecommunications

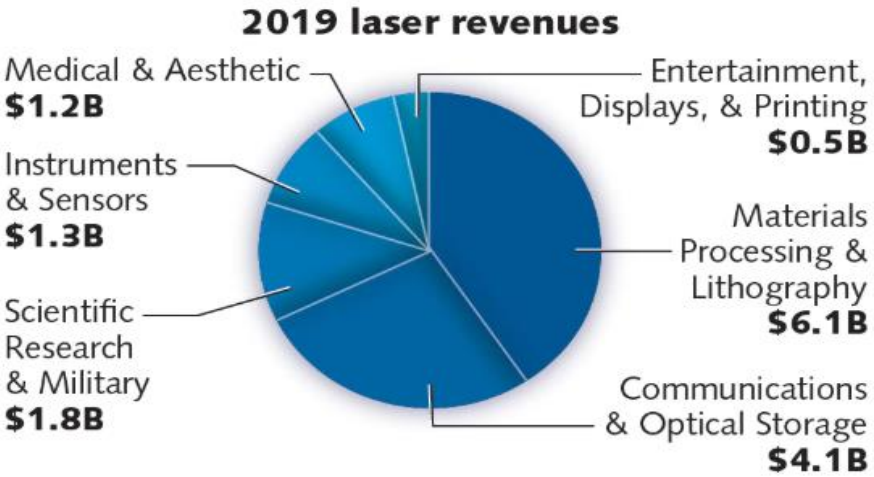

Figure 2.2: Overall annual commercialized laser revenues in 2019 [211]

2.2 Basic principles of lasers

2.2.1 Radiation-matter interaction

"Radiation-matter" interactions describe the effects of radiation on an atom. The term "radiation" is to be taken in its quantum sense:

• Electromagnetic radiation (light, X-ray, gamma ray);

• Particle (electron, neutron, alpha radiation).

These radiations are used to analyse matter. Indeed, atoms are too small to be visible or palpable, so we can only know them indirectly; we observe the way in which they disturb incident radiation. This gave rise to two types of analysis methods:

• Diffraction methods: when the atoms are organized in an orderly fashion (crystal), the radiation will be diffused in certain directions of space only; the study of this spatial distribution of the scattered intensity makes it possible to characterize the organization of matter;

• Spectrometric methods: atoms will absorb part of the incident radiation and re-emit others, the absorption and re-emission spectrum is characteristic of the binding energies of matter, and therefore of its chemical nature.

Incident radiation can interact with the atom in several ways:

• it can be diffused, that is to say that it "bounces" on the atom:

Elastic diffusion: the radiation rebounds without losing energy; if the incident radiation is electromagnetic (light, X-ray) we speak of Rayleigh scattering, if it is an electron, we speak of backscattering;

- Inelastic scattering: the radiation causes the ejection of a weakly bound electron, so it loses energy, this is Compton scattering;

• it can be absorbed, causing an electronic transition:

- If the incident energy is low, it simply causes the change of orbit of an electron;
- If the energy is sufficient, it causes ionization; if the incident radiation is electromagnetic, we speak of a photoelectric effect and the ejected electron is a photoelectron; if the incident radiation is an electron beam, the ejected electrons are secondary electrons.

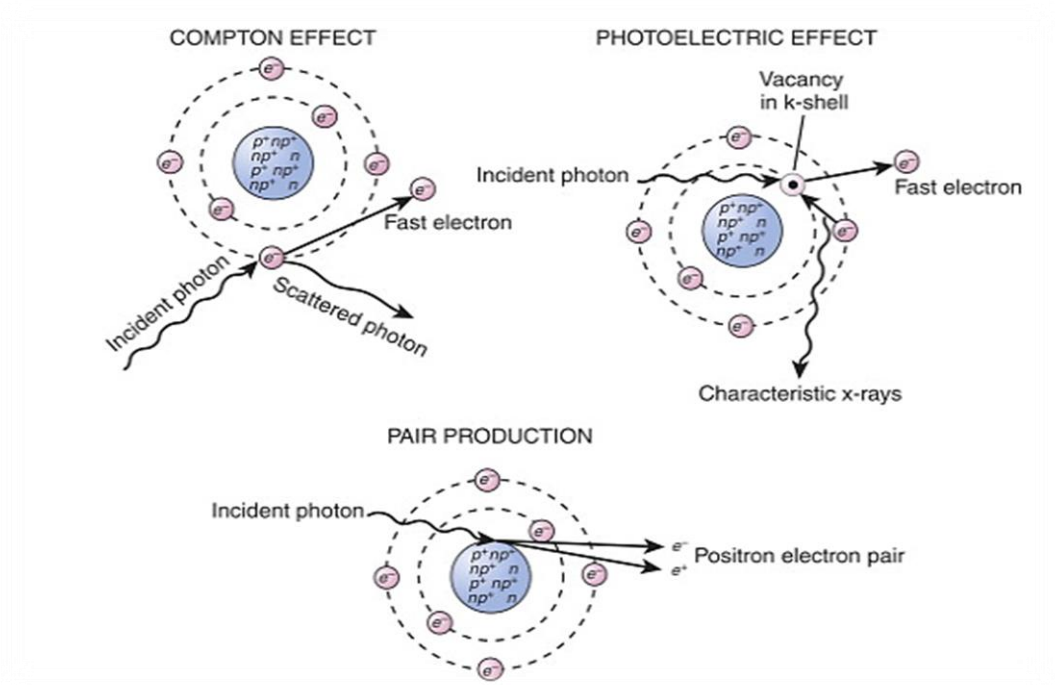

Figure 2.3: Different types of radiation-matter interaction [212]

2.2.2 Einstein's Model of Light–Atom Interaction

Einstein considered two energy states of an atom [213] and postulated three types of atomic transitions which are illustrated in Figure B.1, that is, absorption, spontaneous emission, and stimulated emission.

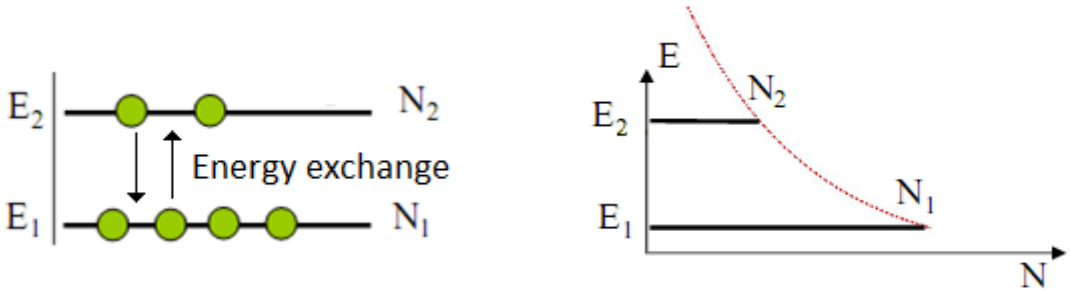

Figure 2.4: Schematic energy diagrams, retaining only the two levels E1 and E2 of the laser transition [214].

For each process, Albert Einstein introduced an individual coefficient which characterizes the respective transition rate (number of transition events per unit time).

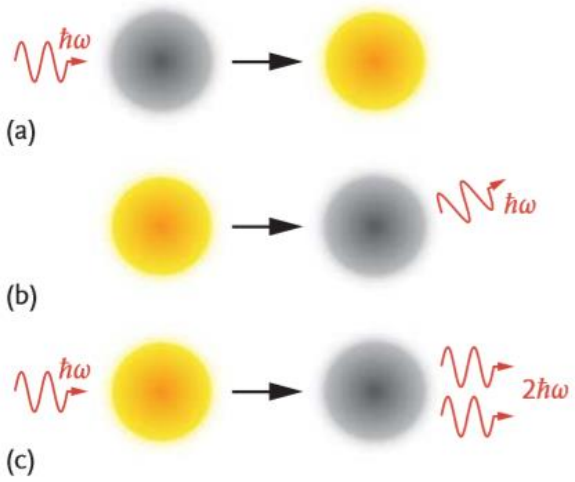

Figure 2.5: Energy transitions of an atom. a) absorption, b) spontaneous emission c) stimulated emission [213]

a-Absorption

An atom in the lower energy state (1) is excited to a higher state (2) by absorption of a photon with the energy $E_2 - E_1 = \hbar\omega_{21}$ (Figure 2.5.a). As a consequence, the photon is annihilated as its complete energy is transferred to the atom. The rate at which the number of atoms in the lower state N_1 changes in time is given by:

$$\frac{dN_1}{dt} = -B_{12}N_1\rho(\omega) \qquad (2.1)$$

where B_{12} is the Einstein coefficient for absorption and $\rho(\omega)$ the spectral energy density of light (energy per volume per frequency interval) with $[\rho]=Js/m^3$. The subscript "12" of the Einstein coefficient indicates that the transition starts with the energy level (1) and ends up in (2).

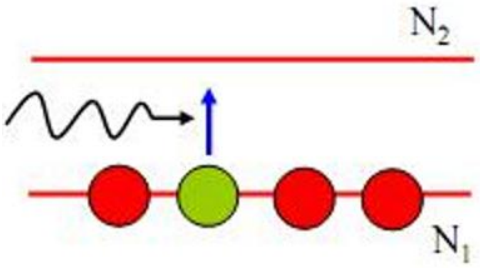

Figure 2.6: Einstein model for the absorption radiative process [204]

b-Spontaneous emission

An excited atom spontaneously transits to the lower state after an average lifetime τ_{21}. At this point, a photon of energy, $\hbar\omega_{21}$ is released and travels along a random direction (Figure 2.5b). Spontaneous emission is a statistical process and arises from the atom's natural tendency to lose its excess energy. The rate at which the population of excited atoms N_2 changes in time is given by:

$$\frac{dN_2}{dt} = \frac{N_2}{\tau_{21}} = -A_{21}N_2 \qquad (2.2)$$

$A_{21} = 1/\tau_{21}$ is the Einstein coefficient for spontaneous emission. If the life time τ_{21} of an atom in the excited state is in the range of some nanoseconds (10^{-9}s), the emission of photons is referred to as fluorescence. Atoms remain virtually forever in the ground state, since this is the only stable energy state.

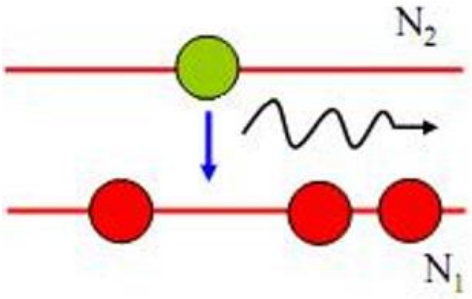

Figure 2.7: Einstein model for the spontaneous emission radiative process [204]

c-Stimulated emission

In case of stimulated emission, an incident photon of energy $\hbar\omega_{21}$ triggers an excited atom to transit to a lower state by generating a second photon (Figure 2.5c). Interestingly, the second photon is a "clone" of the incident one in that it has the same frequency, polarization, and travels along the same direction. Both emitted photons are thus said to be coherent. Analogous to Equations (2.1) and (2.2), the transition rate of stimulated emission is given by:

$$\frac{dN_2}{dt} = -B_{21}N_2\rho(\omega) \qquad (2.3)$$

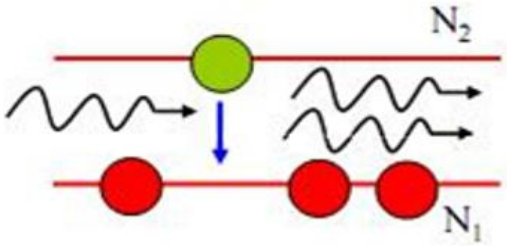

Figure 2.8: Einstein model for the stimulated emission radiative process [204]

Although the Einstein coefficients A_{21}, B_{12}, and B_{21} are associated to different transition processes, they are all directly related to each other. If we know one of them, we can work out the rest. Let us consider mutually non-interacting atoms inside an isolated box. Under steady-state conditions with light present, the rates of atomic excitations and depletions are exactly balanced, that is:

$$\underbrace{B_{12}N_1\rho(\omega)}_{\text{absorption}} = \underbrace{A_{21}N_2 + B_{21}N_2\rho(\omega)}_{\text{emission}} \tag{2.4}$$

Starting from Equation (2.4), Einstein derived that:

$$B_{12} = B_{21} \tag{2.5}$$

Indicating that the probabilities for absorption and stimulated emission are equal. In addition, he found that:

$$A_{21} = \propto \omega^3 B_{21} \tag{2.6}$$

Compared to stimulated emission and absorption, the contribution of spontaneous emission becomes more significant the higher the light frequency. This is why it is generally more difficult to build a laser at high frequencies (or short wavelengths) of light. Furthermore, transitions with high absorption probability also tend to have a high emission rate, for both spontaneous and stimulated processes. [205]

2.2.3 Conditions for Population Inversion

Let us consider atoms exposed to polychromatic light given by the situation shown in Figure 2.9 as an energy level scheme. The energy states of the atomic system are represented by horizontal bars. The states (1) and (2) are called the lower and upper laser levels, respectively. The vertical arrows correspond to possible transition processes. By photon absorption, atoms are excited to the upper laser level (2) a rate P_2 per second per volume.

After a lifetime τ_{21}, they transit back to (1) because of spontaneous emission. State (1) is not necessarily the ground state of the atoms. Another level (0) might exist which is beneath the lower laser level (1). For this reason, an excited atom may also transit spontaneously to the ground state (0) after a lifetime τ_{20}. The total depletion rate by spontaneous emission from the excited state (2) is then given by $1/\tau_2 = 1/\tau_{21} + 1/\tau_{20}$. Pump rate P_1 and lifetime τ_1 of the lower laser level are defined in an analogous way, whereas P_1 does not include spontaneous emission from (2) to (1).

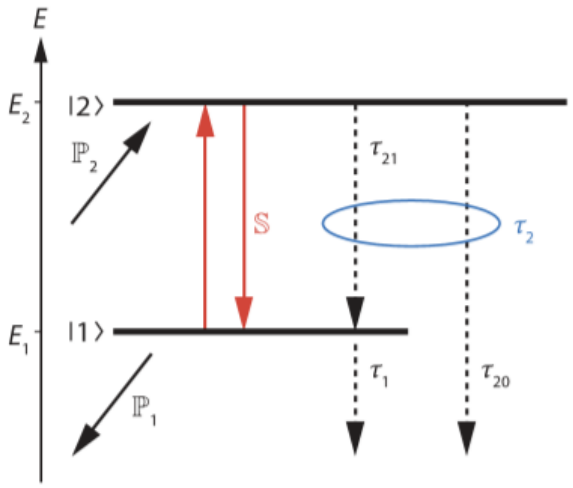

Figure 2.9: Illustration and overview of parameters which are introduced to describe multilevel atomic transitions [205]

To understand the dynamics of a laser system, let us assume a low pump intensity at first. In this case, only the contributions of the pump source and spontaneous emission are taken into account so that the population of atoms in state (1) and (2) changes in time like:

$$\frac{dN_1}{dt} = -P_1 + \frac{N_2}{\tau_{21}} - \frac{N_1}{\tau_1} \tag{2.7}$$

$$\frac{dN_2}{dt} = +P_2 - \frac{N_2}{\tau_2} \tag{2.8}$$

respectively. The relations (2.7) and (2.8) are the rate equations of a non-amplifying system. If pumping and de-excitation are exactly balanced, the population of states remains constant despite dynamic processes. For this stationary state ($\frac{dN_1}{dt} = \frac{dN_2}{dt} = 0$), the population difference [206] N_2 - N_1 between the upper and lower laser levels can be calculated from Equations. (2.7) and (2.8) as:

$$\Delta N_0 = N_1 - N_2 = \mathrm{P}_2\tau_2\left(1 - \frac{\tau_1}{\tau_{21}}\right) + \mathrm{P}_1\tau_1 \tag{2.9}$$

If the factor $(1 - \tau_1/\tau_{21})$ is positive, we may deduce the following necessary requirements for population inversion:

1. The pump rates P_1 and P_2 are large.
2. The depletion rate $1/\tau_2$ from the excited state is low. This means, on average, that the atoms stay for a long time in state (2).
3. The life time in the lower laser level is short. This means that the atoms remain only a short time in state (1) so that this state becomes quickly depleted.

In the next step, we increase the pump beam's intensity. As a consequence, intensity amplification by stimulated transitions (red arrows in Figure 2.9) must be included. For this purpose, we will introduce an additional transition rate S (with $S \propto B_{21}\rho(\omega)$ and expand the rate equations (2.7) and (2.8) to:

$$\frac{dN_1}{dt} = -\mathrm{P}_1 + \frac{N_2}{\tau_{21}} - \frac{N_2}{\tau_1} + \underbrace{N_2S - N_1S}_{\text{Stimulated transitions}} \tag{2.10}$$

$$\frac{dN_2}{dt} = +\mathrm{P}_2 - \frac{N_2}{\tau_2} - \frac{N_2}{\tau_2} - \underbrace{N_2S + N_1S}_{\text{Stimulated transitions}} \tag{2.11}$$

Equation (2.11) reveals that the population of the upper laser level is reduced by stimulated emission. However, since stimulated emission increases the population of (1), the amount of absorption events also rises (see fourth term of Equation (2.11)). In the steady state, the population difference in the presence of stimulated emission is:

$$\Delta N_s = N_2 - N_1 = \frac{\Delta N_s}{1 + \mathrm{s}(\tau_2 + \tau_1 - (\tau_1\tau_2/\tau_{21})} \tag{2.12}$$

where we used Equation (2.9). As expected for a laser, the number of atoms in the excited state and, consequently, the degree of inversion is reduced by the stimulated transition rate S and increased by the pump rate P_2.

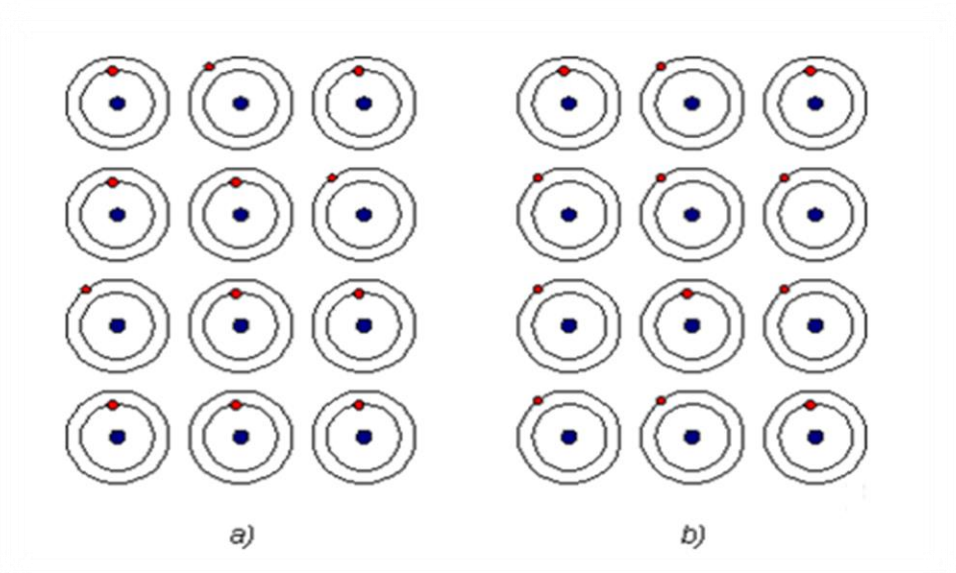

Figure 2.10: a) normal population, there are more atoms at lower levers

b) population inversion, there are more atoms at higher levels [207]

2.3 Laser oscillation

So far, we have only looked at the atomic states to support coherent light amplification. However, a feasible gain medium is only half of the story. For example, consider a rod-shaped gain medium and remember that the traveling directions of spontaneously emitted photons are distributed in a statistical manner. All photons exiting the medium sideways do not effectively contribute to light amplification. By chance, those photons which travel parallel to the rod axis induce more stimulated emission events than all the others so that the resulting radiation is preferably enhanced along the rod axis. If the efficiency of stimulated emission is high enough, an intense light beam is formed. If the rod length is extended, the output power will increase even more and the beam divergence will be reduced. Clearly, such an arrangement already exhibits all typical characteristics of a laser. But losses inside the gain medium lower the total light output. This can only be compensated for by even longer traveling distances of photons inside the gain medium. However, long gain media are not really a practicable solution, because of mechanical difficulties and cost considerations of the very pure materials. To optimize light amplification, we thus let photons pass multiple times through a shorter gain medium by adding a reflecting unit, the so-called resonator. As we will see, this setup leads to a superposition of light waves which again results in a constructive interference effect. The combination of gain medium and resonator is called a laser oscillator. Based on this concept, various designs have

been proposed during the past few decades (Figure 2.11). Depending on the oscillator geometry, the beam shape differs in diameter, divergence, and composition.

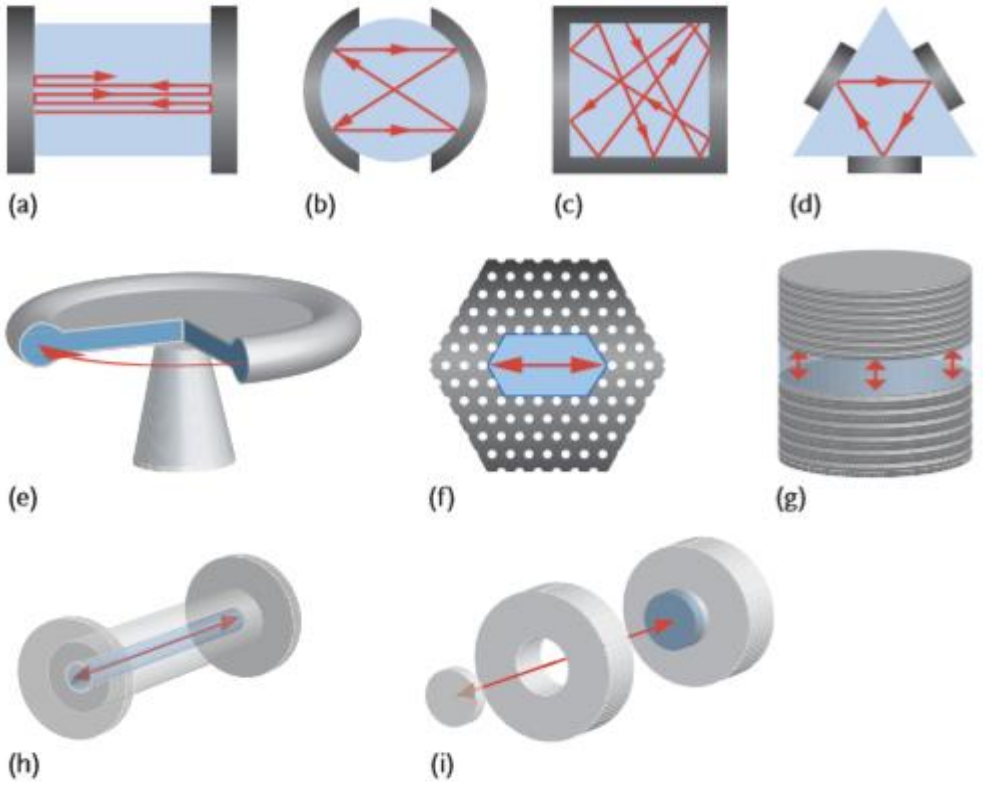

Figure 2.11: Different designs of laser oscillators. The gain medium is blue, the reflector unit of the resonator is shown in grey, and the path travelled by the photons is represented by red arrows.

The different laser oscillators are illustrated as:

- A) Two plane mirrors facing each other.
- (b) Concentric resonator design consisting of two opposite spherical mirrors.
- (c) Rectangular resonator cavity.
- (d) Triangular ring resonator.
- (e) Micro-disk resonator.
- (f) Photonic crystal oscillator for which the resonator itself is made of the gain material. Reflections around the central "defect" region arise, since photons cannot penetrate the periodic hole array.
- (g) Micro-pillar oscillator consisting of a disk-shaped gain medium embedded between two Bragg gratings ("DBRs") that act as mirrors.

- (h) Fiber laser resonator. The gain medium is enclosed by a cladding to keep the beam inside the resonator. At both medium–air interfaces the beam is partially reflected.
- (i) Disk laser resonator.

2.4 Inversion Threshold

Let us first take a look at the consequences of such an oscillator setup on the laser light intensity. Let us consider a gain medium of length L_g and volume V_g and enclose it with two facing mirrors as depicted in Figure 2.12. This arrangement allows the light beam to bounce back and forth. The resulting intensity inside the resonator is then determined by:

$$I = I_+ + I_- \tag{2.13}$$

I_+ and I_- denote the intensities of wave fronts inside the resonator which travel to the right and to the left, respectively. For light amplification, the intensity I must be at least maintained after each round-trip. This means that the intensity enhancement by the gain medium must outweigh the round-trip losses due to absorption, scattering, and so on. Following the beam along the resonator brings us to:

$$(T_i . G . R_1)(T_i . G . R_2)\, I_+ \geq I_+ \tag{2.14}$$

where T_i is the internal transmittance, R_1 and R_2 the reflectances of the resonator mirrors (Figure 2.12),and G is the gain medium amplification factor (gain factor). The latter is determined by:

$$G = e^{\sigma(N_2 - N_1)L_g} \tag{2.15}$$

and thus grows exponentially with the population inversion $\Delta N = N_2 - N_1$. In Equation (2.15), σ denotes the wavelength-dependent optical gain cross-section that describes the strength with which light interacts with atoms via the transition. A large value of σ corresponds to a strong interaction and, hence, to a rapid growth of the light intensity.

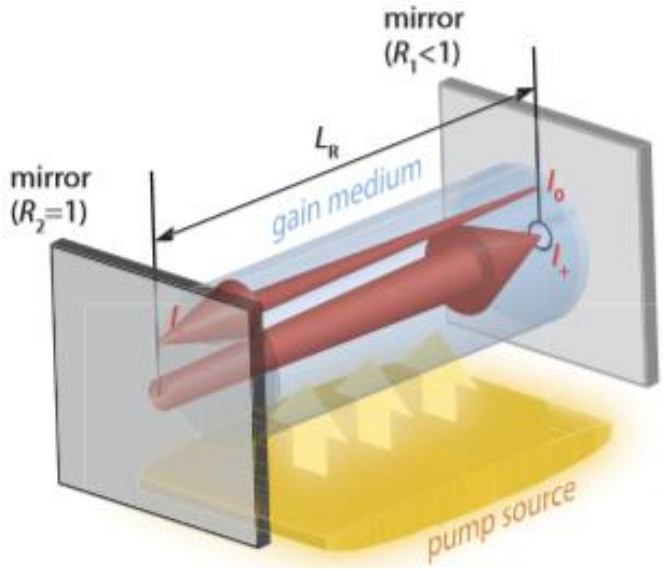

Figure 2.12: Scheme of a typical laser oscillator.

(The gain medium (blue) is encapsulated by two mirrors (grey) which are placed at a distance LR. The left mirror is highly reflective ($R_2 = 1$), whereas the right mirror has a lower reflectance ($R_1 < 1$) and thus acts as an output coupler. Energy is introduced to the oscillator by a pump source (orange). The photons inside the resonator pass the gain medium multiple times (shown as red arrows) while the beam intensity (represented by arrow thickness) is increased.)

With Equation (2.14) and with the mean value of the mirror reflectances $R = \sqrt{R_1 R_2}$, the threshold condition for an oscillator follows as:

$$RT_i G \geq 1 \tag{2.16}$$

If $RT_i G < 1$, the number of photons added by pumping is too small for laser operation. This means that the intrinsic losses of the gain medium "suppress" all photons generated by stimulated emission. Accordingly, the population inversion of real laser systems must be higher than previously discussed, where losses have been neglected. From Equations (2.15) and (2.16), the threshold inversion for laser operation results as:

$$\Delta N_{th} = -\frac{\ln(T_i R)}{\sigma L_g} \tag{2.17}$$

Related to the threshold inversion, we can define a threshold pumping power Pth which depends on atomic parameters like optical gain cross-section σ and life time of the laser level. If the pumping power exceeds the threshold ($P_{pump} > P_{th}$), a net amplification of the light intensity is obtained. The output power of a laser then reads

$$P_{out} = \eta_{sl}\left(P_{pump} - P_{th}\right) \tag{2.18}$$

With the slope efficiency

$$\eta_{sl} = \frac{\Delta P_{out}}{\Delta P_{pump}} \tag{2.19}$$

$$= \left(\frac{\eta_{pump}}{\ln(T_i\sqrt{R})}\right)\left(\frac{R-1}{R+1}\right) \tag{2.20}$$

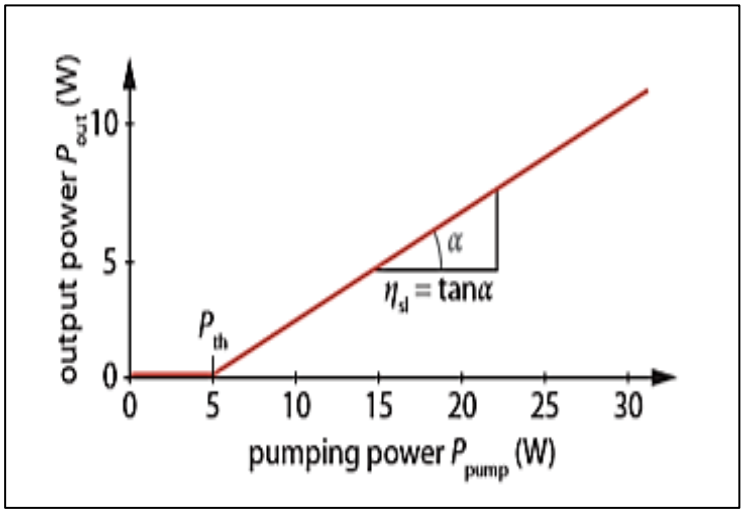

Figure 2.13: Output power dependence the resonator pumping power [218].

The gain medium amplification factor and absorption as well as the reflectance of the resonator mirrors determine the minimum threshold pumping power P_{th}. Below P_{th} we have no laser operation. Above P_{th}, the net output power $P_{out} = \int IdS$ increases linearly. The efficiency η of the system is given by the slope of the curve. Hence, for the example given in this diagram, the threshold pumping power is $P_{th} = 5W$, and the slope efficiency is η_{sl}= 50%.

The slope efficiency depends on the internal transmittance T_i, the reflectance of the resonator mirrors, and the pump efficiency η_{pump} [218]. Alternatively, the output power can be written as:

$$\eta_{out} = I_s \frac{V_g}{L_g}\left(\frac{1-R}{1+\mathrm{R}}\right)\left(\frac{P_{pump}}{P_{th}} - 1\right)$$

$$= \left(\frac{R-1}{\mathrm{R}+1}\right)\left(\frac{\eta_{pump}}{\ln(T_i\sqrt{R})}P_{pump} + \frac{V_g}{L_g}I_s\right) \qquad (2.21)$$

where I_s is the saturation intensity. It is apparent from Equation (2.18) that the laser output power rises linearly with P_{pump} starting from P_{th}. The optimization of the output power for a given pump power usually involves a trade-off between high slope efficiency and low threshold pumping power.

Besides the differential slope efficiency, frequent use is made of the power conversion efficiency.

$$\eta_{pc} = \frac{P_{out}}{P_{pump}} \qquad (2.22)$$

which is the electrical-to-optical power efficiency. It is defined as the ratio of output power to supplied pumping power. η_{pc} does not include the additional power required for cooling and controlling the laser system.

2.5 Laser band structure

To obtain a laser emission, it is necessary to have an inversion of population.

At thermal equilibrium the conduction and valence bands are both above the fermi level in p-type region, and below it in the n-type region, as illustrated in **Figure (2.14-a)**.

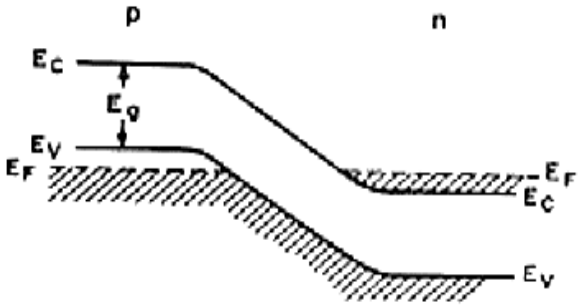

Figure 2.14-a: Band structure of p-n junction at thermal equilibrium [219].

As soon as we apply a direct polarisation to the diode, the injection on electrons at the n-type region and holes at the p-type region shifts the fermi level in both regions (in the opposite direction), as shown in **Figure (2.14-b)**.

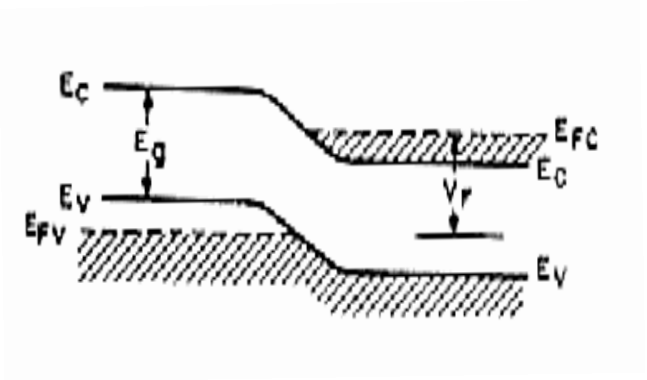

Figure 2.14-b: Band structure of a direct polarized p-n junction [219].

Now, if we increase the polarisation potential (the direct bias), the carriers' injection is sufficient to obtain the situation in **figure 2.14-c**: In the d width space charge zone, we find a high density of electrons in the conduction band and holes in the valence band, which is the condition for a population reversal. For this to happen:

$$E_{F_C} - E_{F_V} > E_g$$

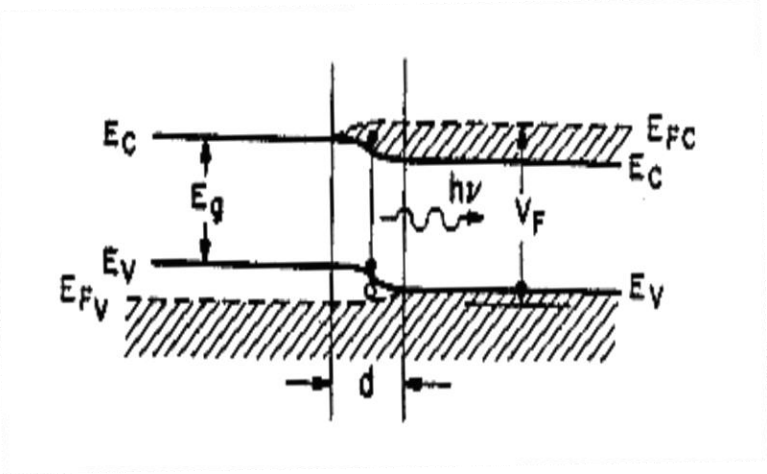

Figure 2.14-c: Band structure of a polarized p-n junction with high direct voltage [219].

2.6 Quantum wells

One important application of heterojunction is to use ΔE_c, and ΔE_v, to form barriers for carriers. A quantum well is formed by two heterojunctions or three layers of materials such that the middle layer has the lowest E_c, for an electron well or the highest E_v, for a hole well. A quantum well thus confines electrons or holes in a two-dimensional (2-D) system. When

electrons are free to move in a bulk semiconductor in all directions (3-D), their energy above the conduction-band edge is continuous, given by the relationship to their momentum:

$$E - E_c = \frac{\hbar^2}{2m_e^*}\left(k_x^2 + k_y^2 + k_z^2\right) \tag{2.23}$$

In a quantum well, carriers are confined in one direction, say in the x-coordinate such that k_x = 0. It will be shown that the energy within this well is no longer continuous with respect to the x-direction, but becomes quantized in subbands.

A well of artificial potential of quantum size is thus produced in which the free carriers of the semiconductor (electron and holes) will find themselves confined to discrete energy levels. Each of the linked energies allowed inside the well is associated with a wave function whose square represents the density of probability of presence on the quantified energy level. The use of quantum wells within the active zone generates a confinement of electrons and holes in a smaller volume, which for a given injection, makes it possible to increase the density of carriers and therefore to achieve the inverse of population more easily [220].

The most-important parameters for a quantum well are the well width L_x, and well height $\emptyset_b$. The potential barrier is obtained from the conduction-band and valence-band offsets (ΔE_C and ΔE_V). The solution for the wavefunction of the Schrodinger equation inside the well is:

$$\Psi(x) = \sin\left(\frac{i\pi x}{L_x}\right) \tag{2.24}$$

Where i is an integer. It should be noted that at the well boundaries, Ψ is truly zero only when $\emptyset_b$ is infinite. With finite $\emptyset_b$, carriers can "leak" out (by tunnelling) of the well with finite probability. This is important for the formation of a superlattice. The pinning of nodes at the well boundaries leads to the quantization of subbands, each has a bottom energy of (with respect to the band edges)

$$E_i = \frac{\hbar^2\pi^2 i^2}{2m^* L_x^2} \tag{2.25}$$

These solutions do not take into account a finite barrier height. With L_x, as a variable, a quantum well can only be loosely defined. The minimum requirements should be that the

quantized energy $\hbar^2\pi^2/2m^*L_x^2$ is much larger than kT, and L_x is smaller than the mean free path and the de Broglie wavelength. (Notice that the de Broglie wave- length λ-$h/(2m^*E)^{1/2}$ has a form similar to L_x of Equation 2.25 Also, it is interesting to note that since the continuous conduction band is now divided into subbands, carriers no longer reside on the band edges E_c or E_v but on these subbands only. In effect, the effective energy gap for interband transitions inside the quantum well becomes larger than the bulk E_g.

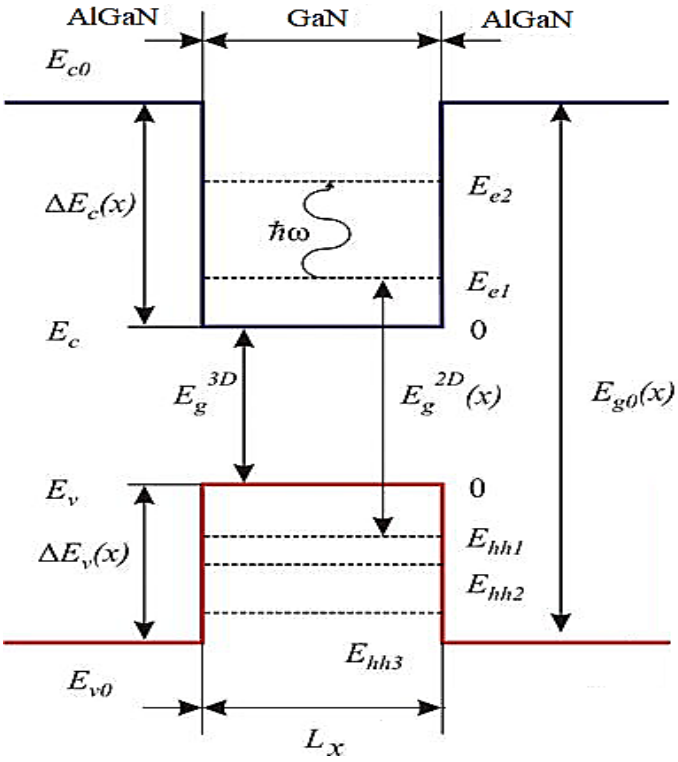

Figure 2.15: Energy structure of GaN/AlGaN quantum well showing its quantification energy levels [221].

Many of the advantages of the quantum-well laser arise from the unique shape of the density of states in a 2-D system. The reduction of threshold current is explained as follows, apart from the fact that the active-layer thickness is thin (Equation 2.26). **Figure 2.16** compares the density of states in 3-D (bulk) and 2-D (quantum-well) systems, as well as their electron concentration distribution. In a 3-D system, since the density of states varies as $\sqrt{E}$ and approaches zero at the band edge, the electron distribution, obtained by multiplying the Fermi-Dirac distribution function, has a wide spread in energy level. In a quantum well (2-D), the density of states is constant within each subband. Consequently, the electron profile at the band

edge, E_1 in this case, is much sharper. This condition makes population inversion much easier to achieve, thus lowering the threshold current.

$$J_{th} = \frac{J_0 d}{\eta_{in}}\left(1 + \frac{g_{th}}{g_0}\right)$$
$$= \frac{J_0 d}{\eta_{in}}\left\{1 + \frac{g_{th}}{g_0 \Gamma}\left[\alpha + \frac{1}{2L} ln\left(\frac{1}{R_1 R_2}\right)\right]\right\} \quad (2.26)$$

At high current bias, more than one subbands are filled with injected carriers. The emission spectrum internally is thus much wider. The lasing wavelength, however, is also selected by other means such as the optical cavity length. So in a quantum-well laser, wavelength tuning can cover a wider range. This is in additional to the variation of quantum-well width which controls the quantization levels.

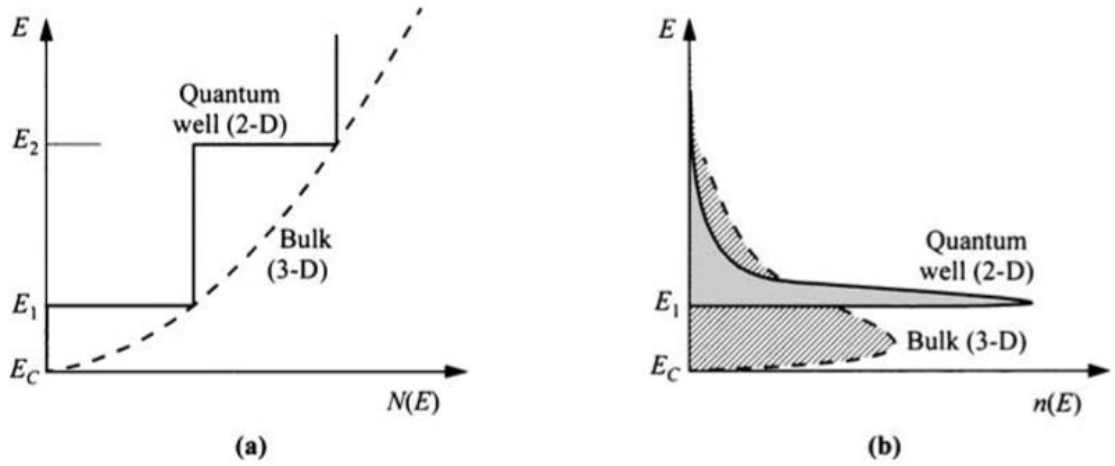

Figure 2.16: Comparison of bulk 3-D and quantum well 2-D systems: (a) Density of states in conduction band, and (b) electron concentration distribution.

2.7 laser optical responses

2.7.1 Threshold current

In stimulated emission, the optical gain depends strongly on the electron concentration in the upper energy level. In a laser diode, the injected electron concentration is proportional to the bias current, so the optical gain also has a linear dependence on the bias current. Figure 2.17 helps to clarify this picture. As the bias current is increased, the Fermi-Dirac distribution functions $F_C(E)$ and $F_V(E)$ change, that is, E_{Fn} increases and E_{Fp} decreases, so the quantity $(E_{Fn} - E_{Fp})$ increases (Figure 2.17-a). The optical gain increases and the shape of the gain curve also changes.

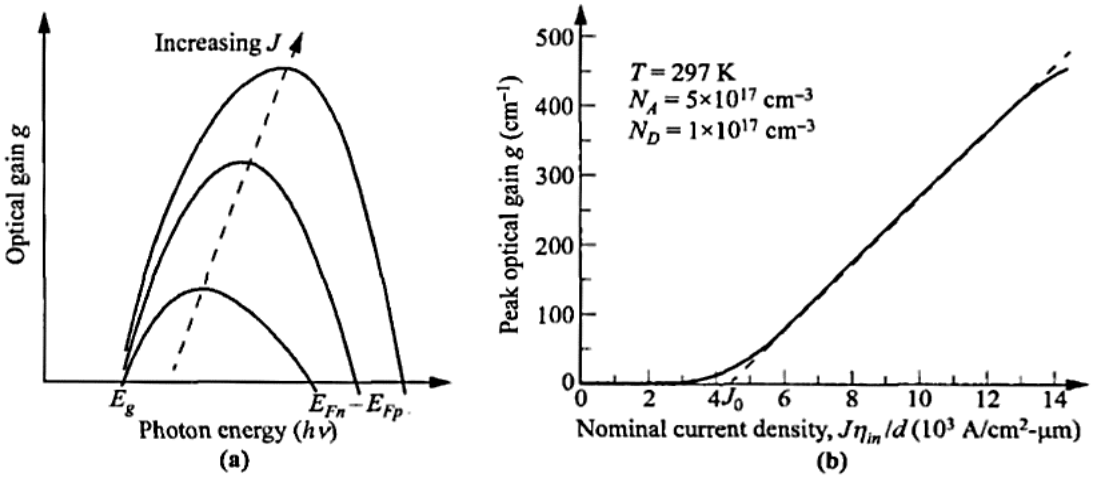

Figure. 2.17: Optical gain as a function of laser bias current.

(a) Optical gain vs. emission photon energy, for different bias current.

(b) Variation of peak optical gain with nominal current density. [222]

The peak optical gain g shifts to a slightly higher energy (shorter wave- length). The relationship between optical gain and bias current can be described by the linear equation.

$$g = \frac{g_0}{J_0}\left(\frac{J\eta_{in}}{d} - J_0\right) \tag{2.27}$$

For a nominal current density ($J\eta_{in}/d$) above a threshold value of J_0 the optical gain increases linearly with the bias current. Figure 2.17-b shows the calculated gain for a sample laser. The gain is superlinear at low values and increases linearly with J for $50 \leq g \leq 400$ cm^{-1}. The linear dashed line represents **Equation 2.27** with g_0/J_0 = 5×10^{-2} cm-μm/A and J_0 = 4.5×10^3 A/cm^2-μm. At higher current bias, the gain is reduced from the projected value and tends to saturate. This phenomenon of gain saturation arises because for a high rate of stimulated emission, the large extent of population inversion is hard to sustain. A reduced electron concentration in the conduction band results in smaller optical gain until a balance is struck when the supply of carriers can replenish the rate of stimulated emission.

We now address the light output when the bias current is varied. The general characteristics are shown in **Figure 2.18**. At low current there is only spontaneous emission in

all directions with a relatively broad spectrum. As the current is increased, the gain increases until the threshold for lasing is reached. The condition for lasing is when the gain is large enough so that a light wave makes a complete traversal of the cavity with the gain equalling the internal loss and external emission. The threshold current density for lasing is given in **equation 2.26** previously mentioned [201]:

$$J_{th} = \frac{J_0 d}{\eta_{in}}\left\{1 + \frac{g_{th}}{g_0 \Gamma}\left[\alpha + \frac{1}{2L} ln\left(\frac{1}{R_1 R_2}\right)\right]\right\} \tag{2.26}$$

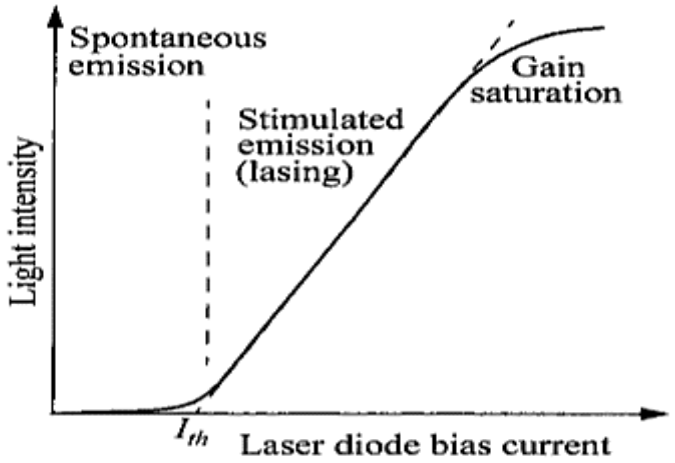

Figure 2.18: light output vs. laser bias current showing the threshold current and the three lasing regimes

This equation also takes into account the confinement factor by replacing g_{th} with Γg_{th}. It is seen here in order to reduce the threshold current density, one can increase η_{in}, Γ, L, R_1 and R_2, and to reduce d and α. Achieving low threshold current is one of the main goals in laser development.

2.7.2 Light Spectra and Efficiencies

Figure 2.19 shows typical output characteristics of semiconductor lasers as the bias current is increased from low currents of spontaneous emission to currents in excess of the laser threshold. At low currents, the spontaneous emission is proportional to the diode bias current, and it has a broad spectral distribution with a typical spectral width at half power of 5 to 20 nm. This is similar to emission in an LED. As the bias current approaches the threshold value, the optical gain can be high enough for amplification so that intensity peaks start to appear. The peaks in wavelength correspond to the standing waves in the optical resonator. At this bias

level, the light is still incoherent due to the nature of spontaneous emission. When the bias reaches the threshold current, the lasing spectra suddenly become much narrower (< 1 Å), and the light is coherent and much more directional. Also shown are multiple modes lasing simultaneously, called longitudinal modes, but the number of modes can be reduced with further increase of bias current, as shown in the top figure. The mode spacing is inversely proportional to the cavity length *L*, so it is advantageous to have small *L* to limit single-mode operation. This is one of the advantages of semiconductor lasers compared to other laser mediums.

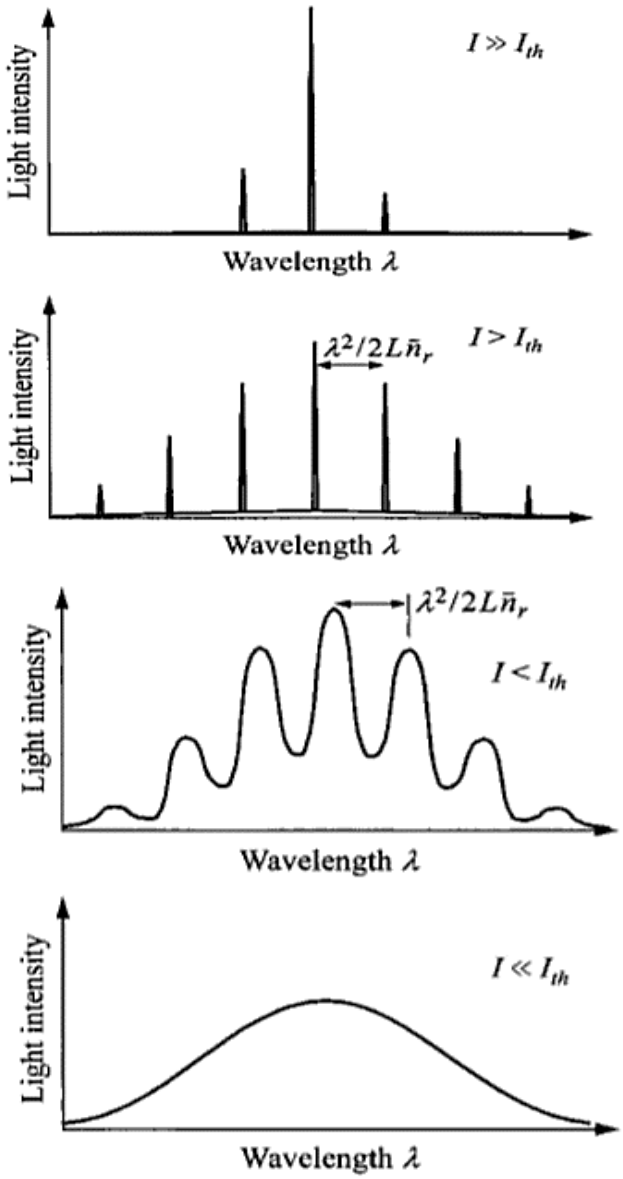

Figure 2.19: Emission spectra of laser diode at different bias current:

(bottom to top) much below threshold, just below threshold, just above threshold, much above threshold. Scales on intensity increasing from bottom to top.

2.7.3 Power-Light characteristic and external efficiency

We consider the power and efficiencies of the laser light output. Above threshold, the power generated by stimulated emission internally is linearly dependent on the bias current:

$$P_{st} = \frac{(I - I_{th})hv\eta_{in}}{q} \tag{2.28}$$

The loss per length inside the optical resonator is a, while the average mirror loss from one complete return path is $(1/2L)\ln(1/R_1R_2)$. The power inside the cavity versus output power are proportional to these factors. The laser power output is, thus, given by the ratio of these factors as:

$$P_{out} = P_s \frac{(1/2L)ln(1/R_1R_2)}{\alpha + (1/2L)ln(1/R_1R_2)}$$

$$= \frac{(I - I_{th})hv\eta_{in}}{q}\left[\frac{ln(1/R_1R_2)}{2\alpha L + (1/2L)ln(1/R_1R_2)}\right] \tag{2.29}$$

The external quantum efficiency is defined as the photon emission rate per injected carrier:

$$\eta_{ex} = \frac{d(P_{out}/hv)}{d[(I - I_{th})/q]}$$

$$= \eta_{in}\left[\frac{ln(1/R_1R_2)}{2\alpha L + (1/2L)ln(1/R_1R_2)}\right] \tag{2.30}$$

The overall power efficiency is defined as

$$\eta_p = \frac{P_{out}}{VI} = \frac{(I - I_{th})hv\eta_{in}}{VIq}\left[\frac{ln(1/R_1R_2)}{2\alpha L + (1/2L)ln(1/R_1R_2)}\right] \tag{2.31}$$

In general, the bias qV is slightly higher than the energy gap E_g or photon energy hv. So η_{in}, η_{ex}, and η_p are very high, in the order of tens of percents.

2.8 laser optical gain

2.8.1 gain expression and achieving conditions

Due to current injection, [224] a non-equilibrium carrier distribution is created. After fast thermalization processes (phonon scattering), it can be mostly described by quasi-Fermi levels. Sufficiently strong pumping leads to inversion, i.e. conduction band states are more strongly populated with electrons than valence band states (**Figure 2.20**). In this case, the stimulated emission rate is stronger than the absorption rate. The thermodynamic laser condition requires the difference of the quasi-Fermi levels to be larger than the bandgap.

$$F_n - F_p > E_g \tag{2.32}$$

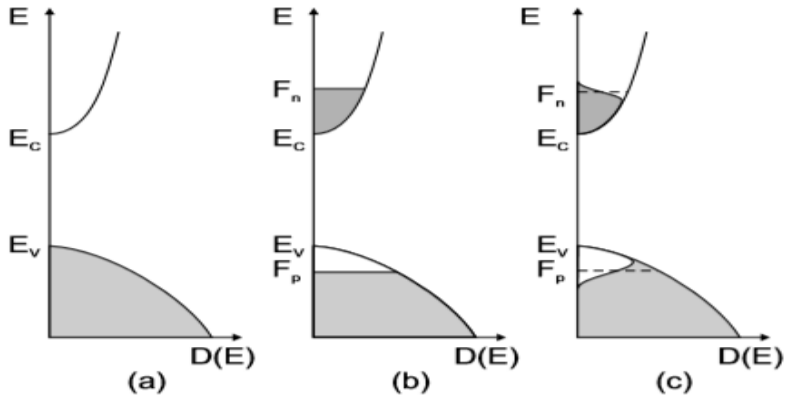

Figure 2.20: Population a) in thermodynamic equilibrium T = 0K, b) under inversion for T = 0K, c) under inversion for T>0K.Shaded areas are populated with electrons

The gain is defined as the (frequency-dependent) coefficient $g(\hbar\omega)$ that describes the light intensity along a path L according to:

$$I(L) = I(0)\exp(gL) \tag{2.33}$$

The gain spectrum as a function of the photon energy $\hbar\omega$ with no momentum vector conservation is given by:

$$g(\hbar\omega) = \int_0^{\hbar\omega - E_g} D_e(E)D_h(E')[f_e(E)f_h(E') - (1 - F_e(E)(1 - f_h(E'))]dE \tag{2.34}$$

With $E' = \hbar\omega - E_g - E$. The gain is positive for those photon energies for which light is amplified and negative for those that are absorbed. In **Figure 2.21-a**, the electron and hole concentrations are shown as a function of the quasi-Fermi energies. In **Figure 2.21-b**,

the difference of the quasi-Fermi energies is shown as a function of the carrier density (for neutrality n = p). The gain spectrum is shown in **Figure 2.21-c** for a two-band model. [203] In the case of inversion, the gain is positive for energies between E_g and $F_n - F_p$. At $\hbar\omega = F_n - F_p$, the gain is zero (transparency) and for larger energies negative (positive absorption coefficient).

For a given fixed energy, the gain increases with increasing pumping and increasing carrier density n (**Figure 2.21-d**). For very small density, it is given as $g(n \to 0) = -\alpha$. The gain rises around transparency approximately linearly with the pumping intensity. At transparency carrier density n_{tr} , the gain is zero. Therefore, the relation $g(n)$ can be approximated as (linear gain model):

$$g(n) \approx \hat{\alpha}\frac{n - n_{tr}}{n_{tr}} \tag{2.35}$$

For large carrier density, the gain saturates (at a value similar to α).

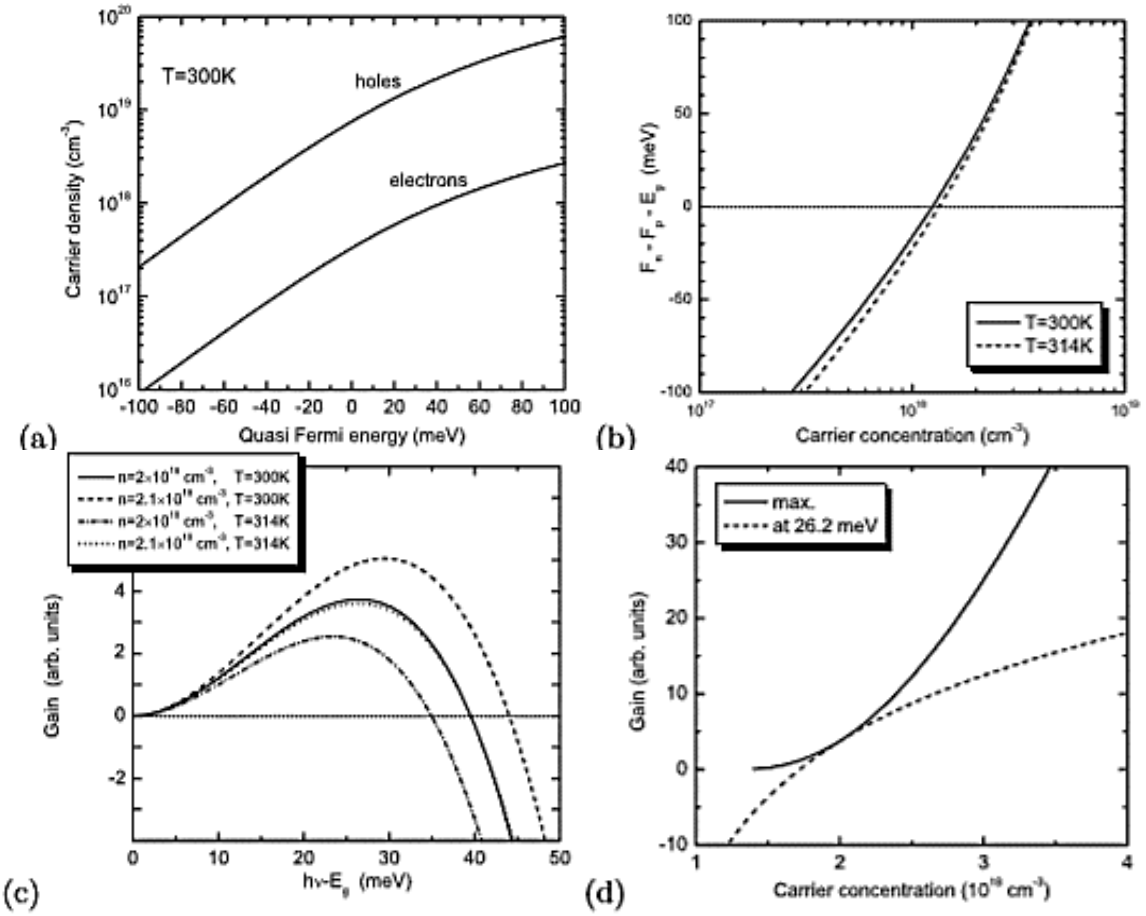

Figure 2.21: Gain in the two-band model **a)** Electron and hole concentrations at T = 300K as a function of the quasi-Fermi energies counted relative to the band edges, i.e. F_n–E_C

and $E_V - F_p$. **b)** Difference of quasi-Fermi levels as a function of carrier concentration (n = p) at two different temperatures. **c)** Gain spectra for n =2×10^{18} and T = 300 K (solid line), increased carrier density n =2.1×10^{18} cm^{-3} and T = 300 K (dashed line), higher temperature n =2×10^{18} cm^{-3} and T = 314K (dash-dotted line) and same difference of the quasi-Fermi levels as for the solid line, n =2.1×10^{18} cm^{-3} and T = 314 K (dotted line). **d)** Maximum gain (solid line) and gain at a particular energy (dashed line), for photon energy E_g+ 26.2 meV for which the gain is maximal for n =2×10^{18} cm^{-3} and T = 300 K.

2.8.2 optical coefficients and rates of radiative interactions

The gain is directly associated with stimulated emission rate $\bar{r}_{21st}$ (number of photons created by stimulated emission per unit of volume and time defined as **[205,226]**:

$$\bar{r}_{21st} = \frac{dF}{dz} \tag{2.36}$$

and

$$F = V_g P(E_{21}) = \frac{c}{n_r} P(E_{21}) \tag{2.37}$$

where at thermal equilibrium de density of photons of energy E_{21} is:

$$P(E_{21}) = \frac{A_{21} f_2 (1 - f_1)}{B_{12} f_1 (1 - f_2) - B_{21} f_2 (1 - f_1)} \tag{2.38}$$

A_{21} is the probability of an electron in E_2 level returns to level E_1, B_{12} and B_{21} are the probabilities of stimulated transitions.

And we know that the net rate of the stimulated emission $\bar{r}_{21st}$ is defined as follows:

$$\bar{r}_{21st} = r_{21st} - r_{12} = B_{21}(f_2 - f_1)P(E_{21}) \tag{2.39}$$

And net rate of the absorption is:

$$\bar{r}_{21abs} = r_{12} - r_{21st} = B_{21}(f_1 - f_2)P(E_{21}) \tag{2.40}$$

The absorption coefficient $\alpha(E_{21})$ is given by:

$$\alpha(E_{21}) = \frac{n_r}{c} B_{21}(f_1 - f_2) \tag{2.41}$$

This coefficient is related to the net rate of stimulated emission $\bar{r}_{21st}$:

$$\alpha(E_{21}) = \frac{h^3 c^2}{8\pi n_r^2 E_{21}^2} \left(e^{(E_{21}/k_B T)} - 1\right) \bar{r}_{21st}(E_{21}) \tag{2.42}$$

So the optical gain can be defined as:

$$g(E_{21}) = \frac{\bar{r}_{21st}}{V_g P(E_{21})} = \frac{B_{21}(f_2 - f_1)}{c/n_r} = -\alpha(E_{21}) \tag{2.43}$$

The coefficient of creation of electron-hole pairs is given by:

$$\alpha'(E_{21}) = \frac{r_{21}}{V_g P(E_{21})} = \frac{n_r}{c} B_{21}(1 - f_2) \tag{2.44}$$

α' is different from α, because it does not take into account the stimulated emission.

In semiconductors, it is necessary for the evaluation of different coefficients to consider all possible transitions that occur between the conduction and valence band separated by an energy $E_{21} = hv$

- The number of occupied states in the conduction band:

$$d_{n_c} = \rho_c(E_2 - E_c) f_c(E_2) dE_2 \tag{2.45}$$

- The number of occupied states in the valence band:

$$d_{n_v} = \rho_v(E_v - E_1) f_v(E_1) dE_1 \tag{2.46}$$

The general form of the net emission rate which is the difference between the emitted and absorbed photons per unit of volume, where the net rates of spontaneous and stimulated emissions respectively are written as:

$$\bar{r}_{sp}(E) = \sum_{i,j} A_{ij}\, \rho_i f_i \rho_j \big(1 - f_j\big) \tag{2.47}$$

And

$$\bar{r}_{st}(E) = \sum_{i,j} A_{ij}\, \rho_i \rho_j \big(f_i - f_j\big) \tag{2.48}$$

A_{ij} is the probability of a radiative transition between the states *i* and *j*, and ρ_i, ρ_j are the densities of states of the states before respectively.

Now let's consider E the energy of transition between a level E' in the conduction band with a level E'' in the valence band.

$$\bar{r}_{sp}(E', E'') = A_{(E', E'')} \rho_c(E') f_c(E') \rho_v(E'') [1 - f_v(E'')] \tag{2.49}$$

We use only one variable by employing the rule of energy conservation $E'' = E' - E$

$$\bar{r}_{sp}(E', E) = A_{(E',E)}\rho_c(E')f_c(E')\rho_v(E' - E)[1 - f_v(E' - E)] \tag{2.50}$$

We obtain the spontaneous emission rate by using integral on all the values of E'

$$\bar{r}_{sp}(E) = \int_{E'} A_{(E',E)}\rho_c(E')f_c(E')\rho_v(E' - E)[1 - f_v(E' - E)]\, dE' \tag{2.51}$$

The same way, the net stimulated emission rate is written:

$$\bar{r}_{st}(E) = \int_{E'} A_{(E',E)}\rho_c(E')\rho_v(E' - E)[f_c(E') - f_v(E' - E)]\, dE' \tag{2.52}$$

where

$$\bar{r}_{sp}(E) = \frac{n_r^3 E^2}{\pi^2 \hbar^3 c^3} \int_{E'} B_{(E',E)}\rho_c(E')f_c(E')\rho_v(E' - E)[1 - f_v(E' - E)]\, dE' \tag{2.53}$$

and

$$\bar{r}_{st}(E) = \int_{E'} B_{(E',E)}\rho_c(E')\rho_v(E' - E)[f_c(E') - f_v(E' - E)]\, dE' \tag{2.54}$$

The absorption coefficient is given by:

$$\alpha(E) = \frac{n_r}{c} \int_{E'} B_{(E',E)}\rho_c(E')\rho_v(E' - E)[f_v(E' - E) - f_c(E')]\, dE' \tag{2.55}$$

The gain $g(E) = -\alpha(E)$ which means:

$$g(E) = \frac{n_r}{c} \int_{E'} B_{(E',E)}\rho_c(E')\rho_v(E' - E)[f_c(E') - f_v(E' - E)]\, dE' \tag{2.56}$$

2.9 The optical gain in quantum wells

In three dimensions, the density of states increases with energy as *E*. It follows that when the injection increases the maximum of the gain curve moves towards high energies (**Figure 2.22-a**). On the other hand, in a quantum well, the density of states is constant in each of the sub-bands. So when the Fermi pseudo-level rises under the effect of the injection, the top

of the gain curve remains fixed at the energy of the bottom of the sub-band (**Figure 2.22-b**). As long as the first sub-band is the only one concerned, the top of the gain curve therefore remains fixed. As a result, the increase in injection more effectively increases the gain for energies corresponding to the bottom of the sub-band. The counterpart of the two-dimensional nature of the density of states is that the gain of the active region saturates when the first sub-bands of the electrons and holes are completely inverted. If the gain then obtained is insufficient to compensate for the losses, the oscillation threshold is not reached and the second sub-bands must be used. The laser emission line then corresponds to the transition e_2-h_2 between the second sub-bands of the electrons and the holes.

2.9.1 Emission wavelength

The properties of symmetry of the electronic wave functions in a quantum well entail the existence of selection rules on the optical transitions. These selection rules, which are strict in a well of infinite height, are reduced in a well of finished height by the exit of the carriers in the barriers. However, even in a well of finite height, the integral covering the envelope functions of the electrons and the holes only has appreciable value for $\Delta n = 0$, $\Delta n = n_e - n_h$ where n_e and n_h are respectively the quantum numbers of the electron and holes subbands.

If the population inversion of the fundamental subbands of electrons and holes e_1 and h_1, makes it possible to create a gain greater than the losses, that is to say to reach the threshold of oscillations of the cavity, the laser emission line is given by:

$$\hbar\omega = E_g + E_{e1} + E_{h1} \qquad (2.57)$$

where E_g is the gap of the material constituting the potential well and E_{e1}, E_{h1} the energies of confinement of the electrons and holes in this well. It is therefore easy to control, in a certain range, the emission wavelength of the laser by varying the width of the well. In a double heterostructure this possibility does not exist, only the composition of the materials makes it possible to adjust the wavelength. **[226]**

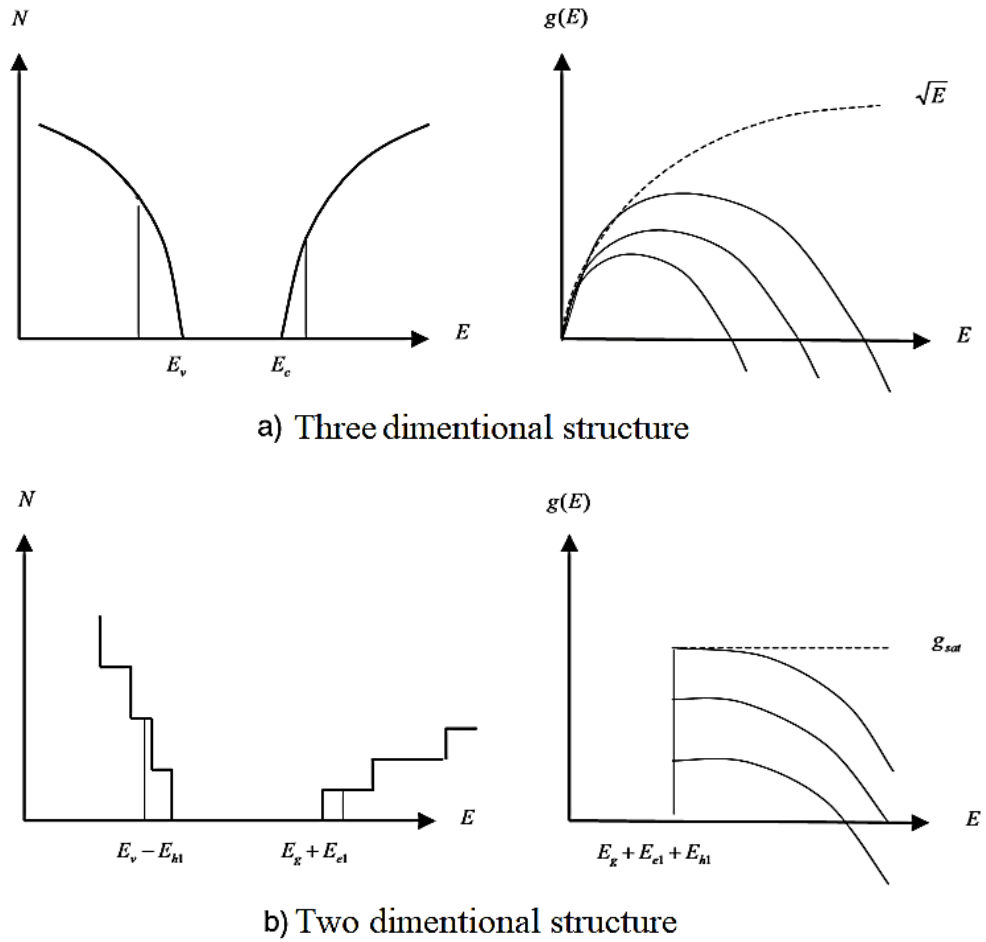

Figure 2.22: Gain characteristic for a) 3-D structure (bulk) b) 2-D structure (QW) [226]

2.9.2 Density of energy levels

The electron gas levels density $\rho(E)$ in 3-D system raise proportionally to $\sqrt{E}$. In quantum wells (2-D system), electrons can move in layers plan but stay confined in the third dimension. The have then two degrees of liberty. The reduced density of state when we take into account all the bands will be expressed as:

$$\rho_r = \frac{m_r^*}{\pi\hbar^2 L_p} \sum_{n=1}^{M} H(E - E_n) \tag{2.58}$$

where H is the Heaviside function.

and the reduced mass:

$$m_r^* = \frac{m_c^* m_v^*}{m_c^* + m_v^*} \tag{2.59}$$

Where: $E_n = E_g + E_{en} + E_{hhn}$ and $E = \hbar\omega$

2.9.3 gain expression with wave vector conservation

In a quantum well with M quantified state levels, the gain is written as:

$$g(E) = \frac{n_r}{c}\sum_{n=1}^{M}\int_{E'}\frac{m_r^*}{\pi\hbar^2 L_p}H(E-E_n)B_{(E',E)}[f_c(E') - f_v(E'-E)]\,dE' \tag{2.60}$$

For one level system (M=1)

$$g(E) = \frac{n_r}{c}\int_{E'}\frac{m_r^*}{\pi\hbar^2 L_p}B_{(E',E)}[f_c(E') - f_v(E'-E)]\,dE' \tag{2.61}$$

Where $\begin{cases} E' = E_c \\ E' - E = E_v \\ E = \hbar\omega \end{cases}$

The probability of transition $B_{(E',E)}$ is given by: [183]

$$B_{(E',E)}(\hbar\omega) = \frac{\pi e^2 h}{m_0^* \varepsilon_0 n_r^2 \hbar\omega}\left|M_{op}\right|^2 \tag{2.62}$$

Where $\left|M_{op}\right|^2$ is the optical matrix element.

$$g(E) = \omega\sqrt{\mu/\varepsilon}\,\frac{m_c^* m_v^*}{m_c^* + m_v^*}\frac{1}{\pi\hbar^2 L_p}\int_{E_{c1}+E_{v1}+E_g}^{\infty}\langle R_{ch}^2\rangle(f_c - f_v)L(E_{ch} - \hbar\omega)\,dE_{cv} \tag{2.63}$$

At the spectrum optical frequencies, the permeability μ is equal to $n_r(\omega)$ which is given by: [227]

$$n_r(\omega) = \sqrt{\varepsilon\omega} \tag{2.64}$$

The following relation gives us the expression of the refractive index given by Peng and Piperk: [206]

$$n_r(\hbar\omega) = \left[a\left(\frac{\hbar\omega}{E_g}\right)^2\left[2 - \left(1 + \left(\frac{\hbar\omega}{E_g}\right)\right)^{0.5} - \left(1 - \left(\frac{\hbar\omega}{E_g}\right)\right)^{0.5}\right] + b\right]^{0.5} \tag{2.65}$$

The parameters a and b are reported in **table 2.1**

	a	b
GaN	9.31	3.03
AlN	13.55	2.05

Table 2.1: The refractive index parameters a and b from [228]

The figure 2.23 shows the refractive index-aluminium concentration dependence for the GaN quantum well width L_p=60Å in $Al_xGa_{1-x}N$ barriers.

- In The quantum well region (GaN) for $x = 0.1,\ n_r = 2.7$ and $x = 0.3,\ n_r = 2.6$
- In the barriers regions ($Al_xGa_{1-x}N$) for $x = 0.1,\ n_r = 2.45$ and $x = 0.3,\ n_r = 2.18$

We can deduce, by simulation calculus, that the variation of the refractive index in the quantum well region is low in contrary to the barrier regions which is high.

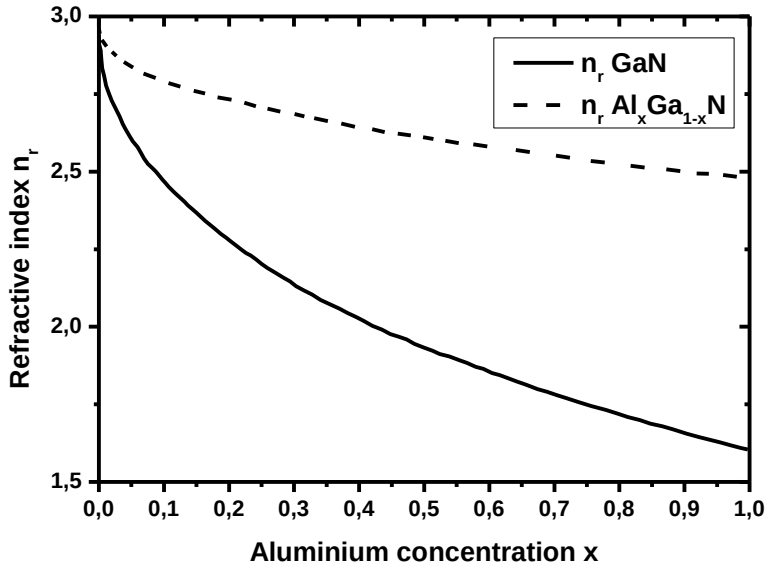

Figure 2.23 The refractive index dependent Aluminium concentration is GaN and $Al_xGa_{1-x}N$ materials

The **figure 2.24** shows the theoretical (from **equation 2.66**) and experimental refractive indexes for $Al_xGa_{1-x}N$ for $\lambda = 400nm$ (which means that we adjust the active zone width correspondent to the wavelength $\lambda = 400nm$).

The change in n_r is expressed as follows **[229]**:

$$n_{r(\lambda=400nm)} = 2.61 - 0.088x + 0.364x^2 \quad (2.66)$$

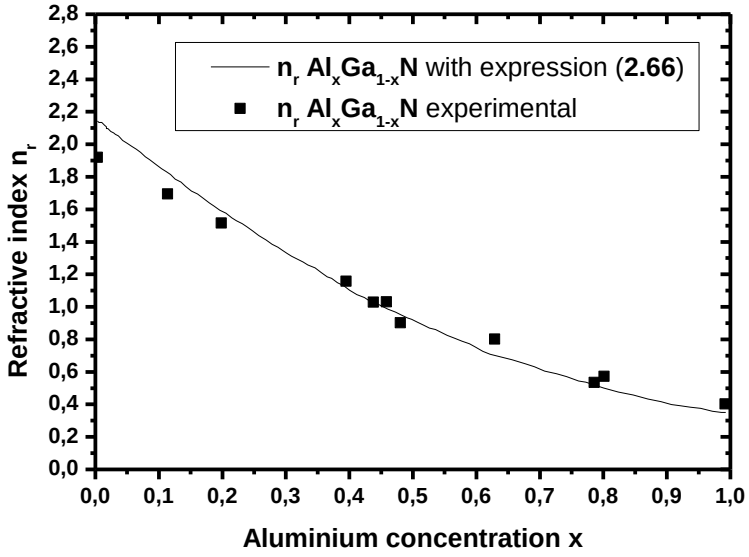

Figure 2.24 The refractive index for $Al_xGa_{1-x}N$ for (λ=400nm) [229]

CHAPTER 3

PHYSICAL MODELS

AND SIMULATION INTERFACE

CHAPTER 3

In this chapter, we are going to describe the physical models employed into the simulation software in order to present this work, a 2-D and 3-D device simulation framework ATLAS of SILVACO TCAD which performs DC, AC, and transient analysis for silicon, binary, ternary, and quaternary material-based devices, and enables the characterization and optimization of semiconductor devices for a wide range of technologies.

3.1 The physical models

3.1.1 The calculation of the density of states

Integrating the Fermi-Dirac statistics over a parabolic density of states in the conduction and valence bands, whose energy minimum is located at energies E_C and E_V respectively, which are referred to as the effective density of states for electrons and holes and are given by:

$$N_c(T_L) = 2\left(\frac{2\pi m_e^* kT_L}{h^2}\right)^{\frac{3}{2}} M_c = \left(\frac{T_L}{300}\right)^{N_{c.F}} N_c 300 \quad (3.1)$$

$$N_V(T_L) = 2\left(\frac{2\pi m_h^* kT_L}{h^2}\right)^{\frac{3}{2}} = \left(\frac{T_L}{300}\right)^{N_{V.F}} N_V 300 \quad (3.2)$$

where M_c is the number of equivalent conduction band minima, T_L is the lattice temperature, $N_{c.F}$ and $N_{V.F}$ are material parameters and taken equal to 1.5 [229,230].

3.1.2 Band gap energy

3.1.2.1 General ternary band gap model with bowing

We use a bandgap model that continuously and non-linearly interpolates between the bandgaps of the two binary extremes in composition (in this case for GaN and AlN materials), and The bandgap as a function of composition is given by:

$$E_g(x,T) = xE_g^{AlN}(T) + (1-x)E_g^{GaN}(T) - bx(1-x) \quad (3.3)$$

where $xE_g^{AlN}(T)$ and $E_g^{GaN}(T)$ are the AlN and GaN bandgaps at a temperature T respectively, x is the aluminum molar fraction and b is the bowing parameter. [231-233]

where the so-called bowing parameter fixed to 0.6 accounts for the deviation from a linear interpolation between the values of $E_g^{AlN}(T)$ and $E_g^{GaN}(T)$ calculated by considering that the coefficients α and β are also dependent on *x* as follows:

$$\alpha(x) = (1-x)\alpha_{GaN} + x\alpha_{AlN} - 2.15x(1-x) \quad (3.4)$$

$$\beta(x) = (1-x)\beta_{GaN} + x\beta_{AlN} - 1561x(1-x) \quad (3.5)$$

The change in the band gap in function of the temperature is given by:

$$E_g(T) = E_g - \left(\frac{\alpha T^2}{\beta+T}\right) \quad (3.6)$$

Where α and β are the coefficients that describe the nonlinear temperature dependence of the bandgap energy. [230]

3.1.2.2 Band gap narrowing

In the presence of heavy doping, greater than 10^{18}cm^{-3}, experimental work has shown that the pn product becomes doping dependent [234]. As the doping level increases, a decrease in the bandgap separation occurs, where the conduction band is lowered by approximately the same amount as the valence band is raised. In Atlas this is simulated by a spatially varying intrinsic concentration n_{ie} where:

$$n_{ie} = n_i^2 e^{\frac{\Delta E_g}{kT}} \quad (3.7)$$

3.1.3 Spontaneous and piezoelectric polarisation

The polarization modeling include both the spontaneous polarization (P_{sp}), which is strain independent, and the piezoelectric polarization along the growth direction <0001> given by [235,236]:

$$P_{pz} = 2d_{pz}\left(C_{11} + C_{12} - 2\frac{C_{13}^2}{C_{33}}\right)\varepsilon_{xx} \quad (3.8)$$

where C_{ij} terms are elastic constants, and d_{pz} is an opportune coefficient, ε_{xx} is the strain tensor.

3.1.4 Shockley-Read-Hall

Phonon transitions occur in the presence of a trap (or defect) within the forbidden gap of the semiconductor. This is essentially a two steps process, the theory of which was first derived by Shockley and Read [237] and then by Hall [238]. The Shockley-Read-Hall recombination is modeled as follows:

$$R_{SRH} = \frac{pn - n_{ie}^2}{\tau_{p0}\left[n + n_{ie}exp\left(\frac{E_t - E_i}{kT_L}\right)\right] + \tau_{n0}\left[p + n_{ie}exp\left(\frac{E_i - E_t}{kT_L}\right)\right]} \quad (3.9)$$

Where T_L is the lattice temperature in degrees Kelvin and τ_{n0} and τ_{p0} are the electron and hole lifetimes related to the carrier cross sections σ_n and σ_p through the equations:

$$\tau_n = \frac{1}{\sigma_n v_n N_T} \quad (3.10)$$

$$\tau_p = \frac{1}{\sigma_p v_p N_T} \quad (3.11)$$

v_n and v_p are the thermal velocities for electrons and holes respectively.

3.1.5 Auger recombination

Auger recombination is commonly modeled using the expression [239]

$$R_{Auger} = C_n(pn^2 - nn_{ie}^2) + C_p(np^2 - pn_{ie}^2) \quad (3.12)$$

Where C_n, C_p are the auger coefficients for electrons and holes respectively.

3.1.6 Impact ionization / incomplete ionization

The electron and hole impact ionization rates, $\alpha_{n,p}$, which are defined as the number of electron– hole pairs generated by the carriers traveling a unit distance along the direction of the electric field, are modeled through the following empirical expression [240]:

$$\alpha_{n,p} = \alpha_{0n,p}exp\left(-\frac{b_{0n,p}}{E}\right) \quad (3.13)$$

The coefficients α_0 and $b_0$were taken from literature [242] as listed in **Table 3.1**. Assuming Fermi–Dirac statistics, the incomplete ionization of impurities can be expressed as [241]

$$N_d^+ = \frac{N_d}{1 + 2\left(\frac{N_d}{N_C}\right)exp\left(\frac{\Delta E_d}{kT}\right)} \quad (3.14)$$

$$N_a^+ = \frac{N_a}{1 + 4\left(\frac{N_a}{N_C}\right)exp\left(\frac{\Delta E_a}{kT}\right)} \quad (3.15)$$

where ΔE_a and ΔE_d are the acceptor and donor energy levels. N_d and N_a are the substitutional n-type and p-type doping concentrations; N_C and N_V are the electron and hole density of states.

Carrier	α_0 (cm^{-1})	b_0 (Vcm^{-1})
Electron	2.41×10^8	3.40×10^7
Hole	5.41×10^6	1.96×10^7

Table 3.1: GaN impact ionization parameters [242]

3.1.7 Mobility model

We have employed an analytic function based upon the work of Caughey and Thomas [243, 244] which can be used to specify doping and temperature-dependent low-field mobilities (following metal polarity along [0001]).

$$\mu_{n0} = \mu_{1n.caug}\left(\frac{T_L}{300k}\right)^{\alpha_{n.caug}} + \frac{\mu_{2n.caug}\left(\frac{T_L}{300k}\right)^{\beta_{n.caug}} - \mu_{1n.caug}\left(\frac{T_L}{300k}\right)^{\alpha_{n.caug}}}{1+\left(\frac{T_L}{300k}\right)^{\gamma_{n.caug}}\left(\frac{N}{N_{critn.caug}}\right)^{\delta_{n.caug}}} \quad (3.16)$$

$$\mu_{p0} = \mu_{1p.caug}\left(\frac{T_L}{300k}\right)^{\alpha_{p.caug}} + \frac{\mu_{2p.caug}\left(\frac{T_L}{300k}\right)^{\beta_{p.caug}} - \mu_{1n.caug}\left(\frac{T_L}{300k}\right)^{\alpha_{p.caug}}}{1+\left(\frac{T_L}{300k}\right)^{\gamma_{p.caug}}\left(\frac{N}{N_{critp.caug}}\right)^{\delta_{p.caug}}} \quad (3.17)$$

Where N is the local (total) impurity concentration in cm^{-3} and T_L is the temperature in degrees Kelvin. The mobility model parameters for GaN are illustrated in table 3.2:

Parameters	Values	Units
$\mu_{1n.caug}$	55	cm^2/(V.s)
$\mu_{1p.caug}$	3	cm^2/(V.s)
$\mu_{2n.caug}$	1000	cm^2/(V.s)
$\mu_{2p.caug}$	170	cm^2/(V.s)
$\alpha_{n.caug}$	1	/

$\boldsymbol{\alpha_{p.caug}}$	1	/
$\boldsymbol{\beta_{n.caug}}$	1	/
$\boldsymbol{\beta_{p.caug}}$	1	/
$\boldsymbol{\gamma_{n.caug}}$	1	/
$\boldsymbol{\gamma_{p.caug}}$	1	/
$\boldsymbol{\delta_{n.caug}}$	1	/
$\boldsymbol{\delta_{p.caug}}$	1	/
$\boldsymbol{N_{critn.caug}}$	2×10^{17}	cm^{-3}
$\boldsymbol{N_{critp.caug}}$	3×10^{17}	cm^{-3}

Table 3.2: Caughey and Thomas mobility parameters for GaN

3.1.8 The radiative recombination model

The default spontaneous radiative recombination model is given by [230]:

$$r_{sP_m}(x,y) = E_{sep} \times EF \frac{c}{N_{eff}} D(E) g_0 \sqrt{\frac{\hbar\omega - E_g}{kT}}$$

$$\times f\left(\frac{E_c - E_{fn} + \gamma(\hbar\omega - E_g)}{kT}\right)\left[1 - f\left(\frac{E_V - E_{fp} + (1-\gamma)(\hbar\omega - E_g)}{kT}\right)\right] \qquad (3.18)$$

Where:

- c is the speed of light,
- h is the Plank's constant,
- k is the Boltzman's constant,
- E_g is the energy bandgap,
- E_C and E_V are the conduction and valence band edge energies,
- T is the lattice temperature,
- E_{fn} and E_{fp} are the electron and hole quasi-Fermi energies,
- ω is the emission frequency that corresponds to the transition parameter E,
- $D(E)$ refers to the optical mode density,
- *EF*: The emission factor, is specified as the scale factor accounting the proportion of light directionally coupled into the lasing mode and it is taken equal to 1,

- g_0 is user defined parameter which is taken equal to 2000 cm^{-1},
- E_{sep} specifies the photon energy separation. It will be automatically set by the calculation of the number of longitudinal modes based on the cavity length and the energy range.
- and N_{eff} is the effective refractive index.
- γ is calculated as follows:

$$\gamma = \frac{1}{\left(\frac{N_C}{N_V}\right)^{\frac{2}{3}} + 1} \tag{3.19}$$

The optical mode density $D(E)$ is given by:

$$D(E) = \frac{n^3 E^2}{\pi^2 \hbar^3 c^3} \tag{3.20}$$

Where n is the refractive index .

The function $f(x)$ is given by:

$$f(x) = \frac{1}{1 + \exp(x)} \tag{3.21}$$

3.1.9 The refractive index model

Finally, Adachi's refractive index model aids to calculate the $Al_xGa_{1-x}N$ x-dependent refractive index as follows [208]:

$$n_r(\omega) = \left(\sqrt{A \left(\frac{h\omega}{E_g}\right)^{-2} \left\{ 2 - \sqrt{1 + \frac{h\omega}{E_g}} - \sqrt{1 - \frac{h\omega}{E_g}} \right\} + B} \right) \tag{3.22}$$

where the material parameters A and B are in the form

$$A(x) = 9.827 - 8.216x - 31.59x^2 \tag{3.23}$$

$$B(x) = 2.736 + 0.842x - 6.293x^2 \tag{3.24}$$

3.1.10 Threshold Current Density

For a single quantum well of width L_w, the threshold current density can be written as [245]:

$$J_{th} = \frac{qL_w n_{th}}{\tau_{th}} \tag{3.25}$$

where n_{th} and τ_{th} are the threshold carrier density and lifetime, respectively.

By increasing the temperature, the intrinsic losses of the laser diode tend to increase while the device internal efficiency factor tends to decrease. The variation of the threshold current with temperature is assumed in the form [183]:

$$J_{th}(T) = J_{th} exp^{\frac{T-T_0}{T_0}} \tag{3.26}$$

where J_{th} is the reference value at a given temperature, and T_0 is a specific parameter that determines the effective degradation of the diode conduction capabilities and the resulting increase of the laser threshold current. This temperature parameter was calculated for AlGaN-based laser diodes by fitting experimental data on J_{th} in [246]. In particular, T_0 was estimated to be 132 K in the low temperature range and it drops down to 89 K for T higher than about 395 K.

3.1.11 Calculations for the optical gain

the optical gain characteristics of a gallium nitride (GaN)-based QW laser is calculated using two different band energy models; the first is based on the simple parabolic band model whereas the second is based on a multiband formalism based on the perturbation theory (k.p model) for calculating the valence band structure.

3.1.11.1 The parabolic band model

In the model, we have assumed parabolic energy levels in the QW for both the conduction and valence band [247], and the gain model is given by:

$$g(x,y) = g_0\sqrt{\frac{\hbar\omega - E_g}{kT}}\left[f\left(\frac{E_c - E_{fn} + \gamma(\hbar\omega - E_g)}{kT}\right) - f\left(\frac{E_v - E_{fp} + (1-\gamma)(\hbar\omega - E_g)}{kT}\right)\right] \quad (3.27)$$

Where the model's parameters are mentioned in section (3.6).

In this model, there is no valence band mixing, and the momentum matrix element P is set to zero when solving for the band structure. This produces parabolic bands, which is a good approximation for wide gap materials.

For a better understanding of the parabolic approximation let us first know where it comes from:

Let us consider the probability of occupation. Electrons are Fermions, for a given energy E measured with respect to the Fermi energy E_f they obey the Ferm-Dirac distribution function.

$$f_{FD}(E,T) = \frac{1}{1 + e^{\frac{E-E_f}{kT}}} \quad (3.28)$$

At zero temperature the Fermi-Dirac distribution is a step function. It reflects a situation where the occupation probability for all states below the Fermi level is 1 and all states above the Fermi level are free. At finite temperature there is some probability for occupied states above the Fermi level. In the figure below the green curve illustrates the Fermi-Dirac function for finite temperature (plotted upwards). Note that correctly speaking the Fermi level should be called chemical potential because the term Fermi level refers to the energy of the highest occupied electron level; as we do not have electron levels within the gap of ideal semiconductors, there are cannot be any electrons with this energy and the Fermi level would always be at the valence band edge. Unfortunately, the term is used a little sloppy in semiconductor physics.

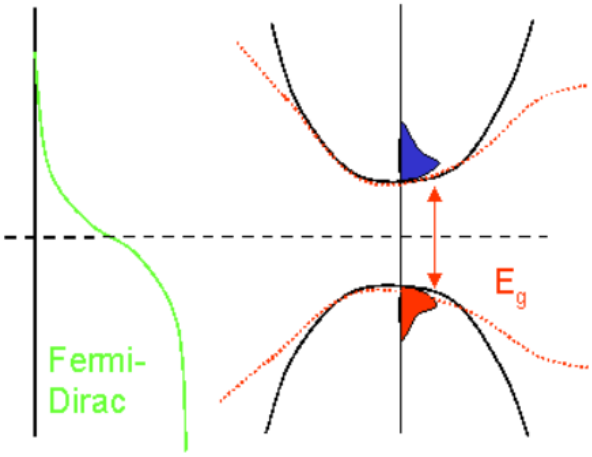

Figure 3.1: Fermi-Dirac function and energy band diagram showing the parabolicity approximation [248].

We observe that in the presence of the bandgap the possible states in the valence band and the conduction band overlap only with the tails of the distribution. For energies far away from the band edges the distribution function drops off exponentially and those states are hardly ever populated. Thus, it is allowed to ignore the exact band structure and expand the energy dependence in Taylor series of second order in *k* around the valence band maximum (VBM) and the conduction band minimum (CBM), respectively. This is known as the parabolic band approximation.

$$E \approx E_0 + \frac{(k-k_0)^2}{2} \underbrace{\left.\frac{\partial^2 E}{\partial k^2}\right|_{k=0}}_{\hbar/m^2} \tag{3.29}$$

The curvature of the energy with respect to k in the proximity of the band edges take over the part of an inverse mass, the so called effective masse *m**. This description is equivalent to the free electron approximation, all the difficulties of crystal periodicity and electron interaction are now packed into one single parameter, the effective mass which the main parameter that also defines the valence bands heavy holes (HH), light holes (LH), and split-off (SO) bands which will be described in k.p band model in the following section.

Let us note that this model is useful for modeling the principle effects, however, it lacks for some drawbacks such as the non-accounting for strain effect (piezoelectric fields effects) and the lack of some physical basis such as the effect of the quantum confinement on such optical characteristics calculations.

3.1.11.2 k.p band model

In this model and in order to obtain more accurate optical responses, we included some parameters and more physically based models into calculations.

The schematic of calculation method is illustrated in figure 3.2.

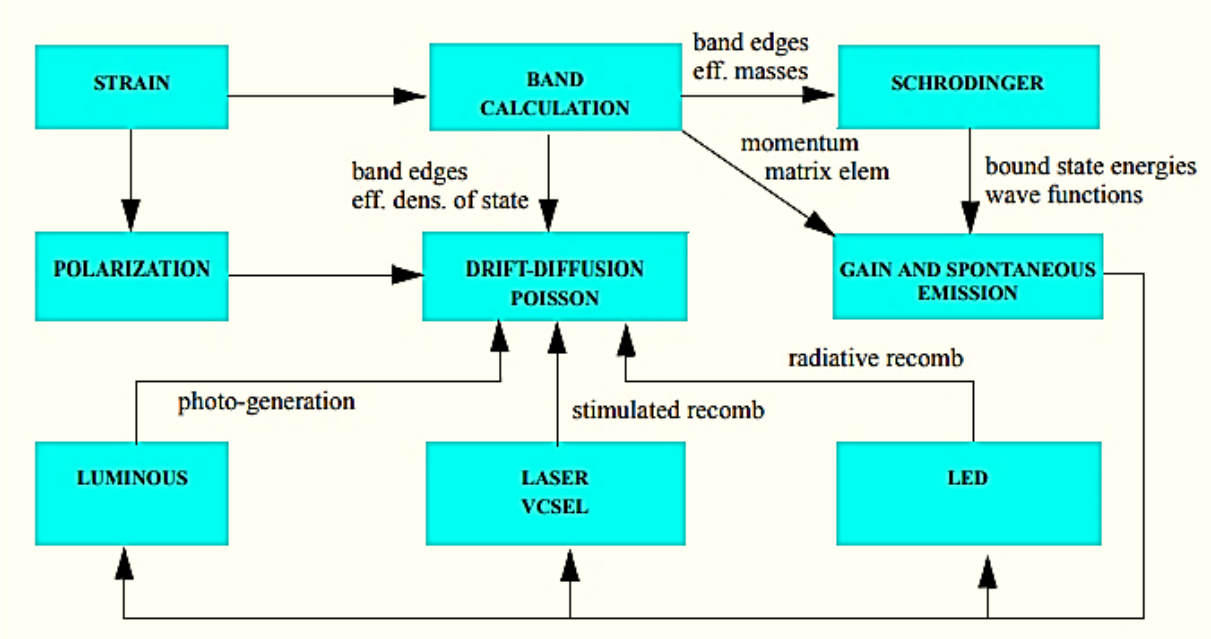

Figure 3.2: Simulation Flow for the optical model's calculations [230]

First, strain is calculated from lattice mismatch and used to calculate the strain effects on band calculations. The strain is also introduced to polarization calculations that enter directly into the drift diffusion calculations as polarization fields.

Next, the band parameters (band-edges and effective masses) are used directly in the drift diffusion simulations as well as feeding into the solutions of Schrodinger's equations to calculate the bound state energies. The band parameters and bound state energies are then used to calculate gain, radiative recombination rate and optical absorption.

The solution for the bound state energies is done by solving Schrodinger equation along discrete slices in the quantization direction. Effective masses and band-edge parameters are calculated from a multi-band k.p-based model.

Let's note that most multiband models treat the electronic states within the effective mass approximation, however, way from the Brillouin zone center, the valence bands calculated within these models can quickly deviate from the exact band structure depending on the strength of inter-mixing of the hole states. The optical response calculated within these models also

become less reliable for large spatial changes in effective mass parameters between the well and the barrier region. This is the reason why we employed a Multiband k.p Model that takes into account this inter-mixing of states to provide a much more accurate band structure and optical response over a wider region of the Brillouin zone.

we have considered a parabolic energy levels for electrons while the hole energy levels have been computed via a 6×6 diagonalized k.p Hamiltonian matrix in the form [249,250]:

$$H^{v}_{6\times6}(K) = \begin{bmatrix} H^{U}_{3\times3}(K) & 0 \\ 0 & H^{L}_{3\times3}(K) \end{bmatrix} \tag{3.30}$$

where $H^{U}_{3\times3}(K)$ and $H^{L}_{3\times3}(K)$ are 3×3 matrices given by

$$H^{U}(K) = \begin{bmatrix} F & K_t & -iH_t \\ K_t & G & \Delta - iH_t \\ iH_t & \Delta + iH_t & \lambda \end{bmatrix} \tag{3.31}$$

$$H^{L}(K) = \begin{bmatrix} F & K_t & iH_t \\ K_t & G & \Delta + iH_t \\ -iH_t & \Delta - iH_t & \lambda \end{bmatrix} \tag{3.32}$$

These matrix elements, which contain the general expressions for a strained semiconductor, can be expressed as follows:

$$F = \Delta_1 + \Delta_2 + \lambda + \theta \tag{3.33}$$

$$G = \Delta_1 - \Delta_2 + +\lambda + \theta \tag{3.34}$$

$$\lambda = \frac{\hbar^2}{2m_0}(A_1 k_z^2 + A_2 k_t^2) + D_1 \varepsilon_{zz} + D_2\left(\varepsilon_{zz} + \varepsilon_{yy}\right) \tag{3.35}$$

$$\theta = \frac{\hbar^2}{2m_0}(A_3 k_z^2 + A_4 k_t^2) + D_3 \varepsilon_{zz} + D_4\left(\varepsilon_{zz} + \varepsilon_{yy}\right) \tag{3.36}$$

$$K_t = \frac{\hbar^2}{2m_0} A_5 k_z^2 \tag{3.37}$$

$$H_t = \frac{\hbar^2}{2m_0} A_6 k_t k_z \tag{3.38}$$

$$\Delta = \sqrt{2}\Delta_3\ \theta \tag{3.39}$$

where A_{1-6} are hole effective mass parameters, Δ_{1-3} are split energies, D_{1-4} are shear deformation potentials, K_t and K_z are wavevectors along the device x-y basal plane and

z-direction, respectively, and ε_{xx}, ε_{yy}, and ε_{zz} are the strain tensors relative to the lattice constant mismatch between the quantum well and the barrier layers modeled through the expressions:

$$\varepsilon_{xx} = \varepsilon_{yy} = \frac{a_1 - a_0}{a_0} \tag{3.40}$$

$$\varepsilon_{zz} = \frac{c_1 - c_0}{c_0} \tag{3.41}$$

where a_i and c_i are the lattice constants in the device structure.

Next, we can calculate the valence band energies from Equations (3-40) through (3-42)

$$E_{hh}^0 = E_v^0 + \Delta_1 + \Delta_2 + \theta_\varepsilon + \lambda_\varepsilon \tag{3.42}$$

$$E_{lh}^0 = E_v^0 + \frac{\Delta_1 - \Delta_2 + \theta_\varepsilon}{2} + \lambda_\varepsilon + \sqrt{\left(\frac{\Delta_1 - \Delta_2 + \theta_\varepsilon}{2}\right)^2 + 2{\Delta_3}^2} \tag{3.43}$$

$$E_{ch}^0 = E_v^0 + \frac{\Delta_1 - \Delta_2 + \theta_\varepsilon}{2} + \lambda_\varepsilon - \sqrt{\left(\frac{\Delta_1 - \Delta_2 + \theta_\varepsilon}{2}\right)^2 + 2{\Delta_3}^2} \tag{3.44}$$

Here, Δ_1, Δ_2 and Δ_3 are split energies and E_v is the valence band reference level [230].

3.2 The simulation process

The simulation was performed with ATLAS of SILVACO TCAD simulation software which provides general capabilities of provides general capabilities for physically-based two (2D) and three-dimensional (3D) simulation of semiconductor devices.

The device structure can be defined by specifying its dimensions and properties starting from the mesh specification, the regions on the structure, the used materials, the doping profile and the doping concentrations onto a two or three dimensional profile.

The mesh is defined by a series of horizontal and vertical lines and the spacing between them. Then, regions within this mesh are allocated to different materials as required to construct the device, the cross between each horizontal and vertical line is called a node.

The electrical characteristics of the device can be achieved by solving the continuity equations, Poisson equation, and the drift-diffusion (transport) equations with specified

numerical methods in each node of the meshing grid with a specified bias conditions using the numerical parameters of each region.

Poisson equation including the carrier concentrations, the ionized donor and acceptor densities are calculated by "incomplete ionization" model. Fermi-Dirac statistics and the density of states are used to calculate the electron and hole concentrations and the quasi-Fermi levels. The generation and recombination rates in the continuity equations which include the carriers' generation and recombination processes are included by using generation and recombination models of the simulation software.

For the bias conditions, the DC solution was used to calculate the current-voltage (I-V) characteristics and then some optical characteristics such the output optical power vs the current (PI) or in function of the current density (P-J).

In the next section we will describe how can a code be defined in ATLAS of SILAVCO-TCAD software and the statements that activate the previous physical models.

3.2.1 ATLAS inputs and outputs

The **figure 3.3** illustrates the types of information that flow in and out of Atlas. Most Atlas simulations use two input files. The first input file is a text file that contains commands for Atlas to execute. The second input file is a structure file that defines the structure that will be simulated. Atlas produces three types of output files. The first type of output file is the run-time output, which gives you the progress and the error and warning messages as the simulation proceeds. The second type of output file is the log file, which stores all terminal voltages and currents from the device analysis. The third type of output file is the solution file, which stores 2D and 3D data relating to the values of solution variables within the device at a given bias point.

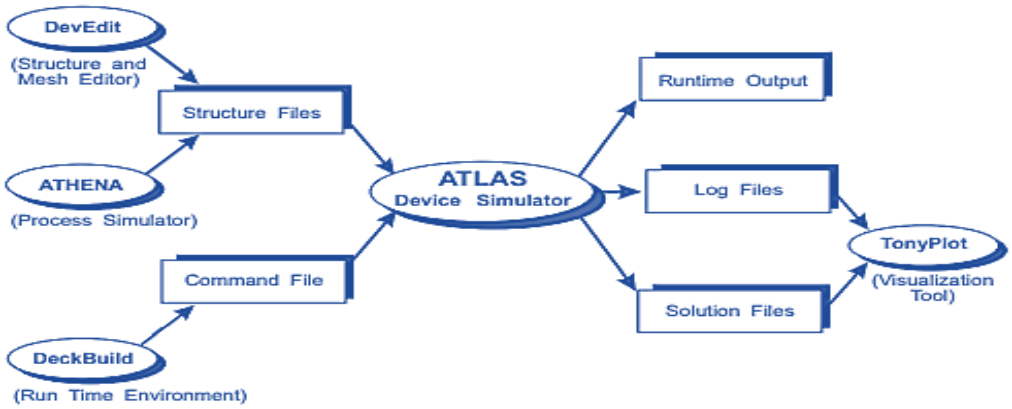

Figure 3.3: Atlas inputs and outputs [230]

As an input-output interface, we used DeckBuild run-time environment, which is an interface that can relate between the user and Atlas simulator that contains two sections, the first one is for the input command file, however, the second is for the output runtime file). In order to run Atlas inside DeckBuild, the code must start with statement GO ATLAS. Also a single input file may contain several Atlas runs separated with a GO ATLAS line.

3.2.2 ATLAS commands

The ATLAS commands consist of a sequence of statements. Each statement consists of a keyword that identifies the statement and a set of parameters. The general format is:

<STATEMENT> <PARAMETER> = <VALUE>

For any <STATEMENT>, ATLAS may have four different types for the <VALUE> parameter. These are: Real, Integer, Character, and Logical.

ATLAS also can read up to 256 characters on one line, but it is preferable to spread long input statements over several lines to make the input file more readable. The \ character at the end of a line indicates continuation.

The order in which statements occur in an Atlas input file is important, this is why ATLAS has five consecutive groups of statements that must occur in an exact order, illustrated in the **figure 3.4** bellow:

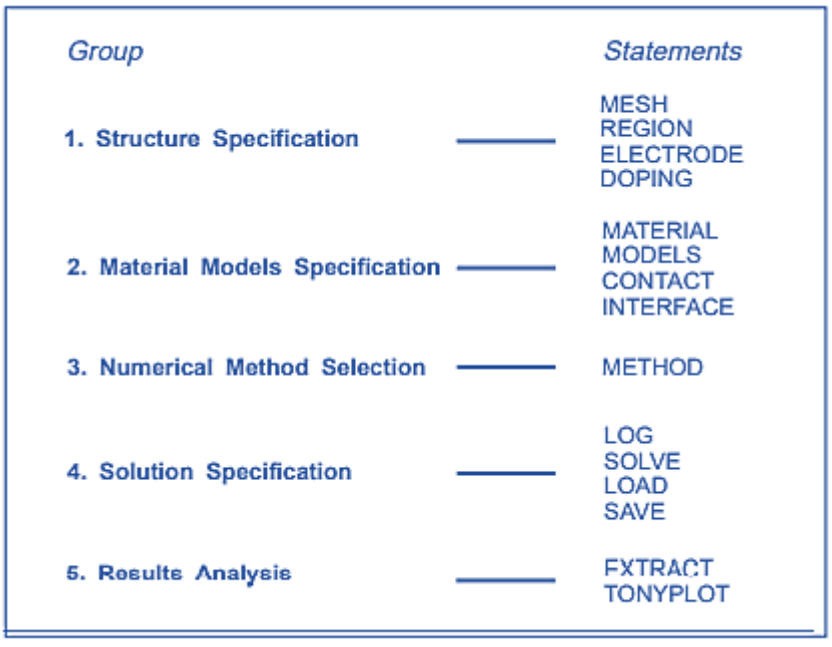

Figure 3.4: Atlas command groups with primary statements in each groups [230]

a. Structure specification

There are the ways to define a device structure in ATLAS.

The first way is to read an existing structure from a file. The structure is created either by an earlier Atlas run or another program such as Athena or DevEdit of SILVACO TCAD. A "MESH" statement loads in the mesh, geometry, electrode positions, and doping of the structure.

The second way is to use the Automatic Interface feature from DeckBuild to transfer the input structure from Athena or DevEdit of SILVACO TCAD.

The third way is to create a structure by using the Atlas command language, which is the way we used in our code. In this case the information described in the following four sub-sections must be specified the order listed in **figure 3.4**.

I- The Mesh specification

The first statement of the code and the structure section is the mesh statement. Mesh statement allows the user to specify the structure types (rectangular, circular and cylindrical). Each of these structure types can be defined in 2 or 3 dimension. Here we will see how to define a 2D triangular structure.

The first employed statement is:

MESH WIDTH

Which specifies a scale factor to represent the un-simulated dimension for 2D simulations and where scale factor is applied to all run time and log file outputs.

This is followed by a series of X.MESH and Y.MESH statements.

X.MESH LOCATION = <VALUE> SPACING = <VALUE>

Y.MESH LOCATION= <VALUE> SPACING = <VALUE>

The X.MESH and Y.MESH statements are used to specify the locations in microns of vertical and horizontal lines, respectively, together with the vertical or horizontal spacing associated with that line. These statements must be listed in the order of increasing x and y. Both negative and positive values of x and y are allowed. Atlas sets some limits on the maximum number of grid nodes that can be used. But this shouldn't be viewed as a bottleneck to achieving simulation results. In the default version, 2D Atlas simulations have a maximum node limit of 100,000.

The reason why we employed rectangular mesh is that our device (Laser) uses only this type of mesh, and it will be taken as default when Atlas mesh is rectangular. (Alternatively, we would be suggested to set up a separate laser mesh with LX.MESH and LY.MESH statements). By default, the solution domain spans over the whole device.

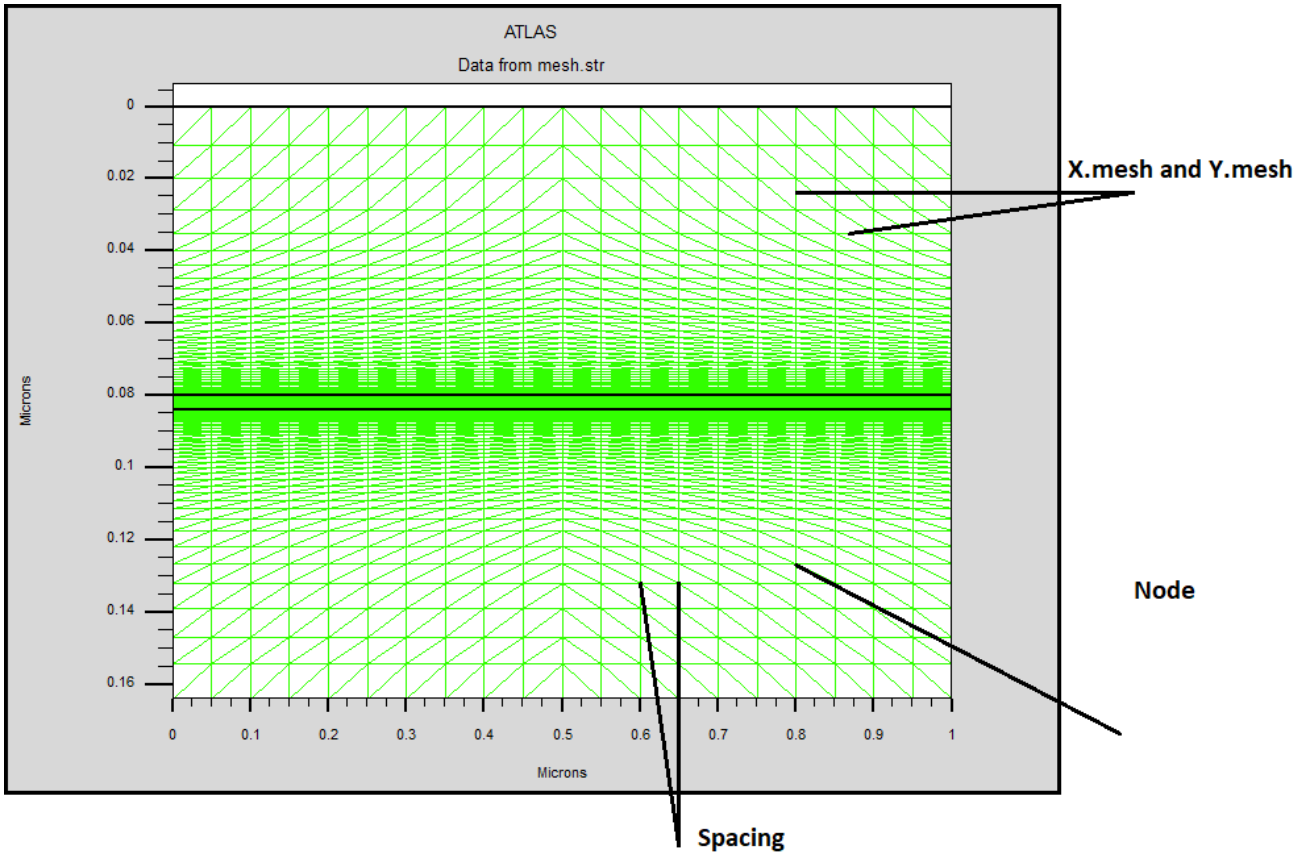

Figure 3.5: The meshing of the structure

Specifying a good grid is a crucial issue in the device simulation but there is a trade-off between the requirements of accuracy and numerical efficiency. Accuracy requires a fine grid that resolves the structure in solutions. Numerical efficiency is greater when fewer grid points are used. The critical areas to resolve are difficult to generalize because they depend on the technology and the transport phenomena, and in our case the fine grid area should be in the active region (the quantum well region) of the device (the laser).

The CPU time required to obtain a solution is typically proportional to N^{α}, where N is the number of nodes and α varies from 2 to 3 depending on the complexity of the problem.

Thus, the most efficient way is to allocate a fine grid only in critical areas and a coarser grid elsewhere. The three most important factors to look for in any grid are:

- Ensure adequate mesh density in high field areas.
- Avoid obtuse triangles in the current path or high field areas.
- Avoid abrupt discontinuities in mesh density.

II-Regions specification

Region specifies the location of materials in a previously defined mesh, where every triangle must be defined as a material.

REGION number = <integer> <material_type> <position parameters>

Region numbers must start at 1 and are increased for each subsequent region statement, and it can have up to 15000 different regions in Atlas. If a composition-dependent material type is defined (like in our case, a ternary alloy $Al_xGa_{1-x}N$), the x composition fraction is also specified in the REGION statement.

III-Electrodes specification

Once we have specified the regions and materials, one has to define at least one electrode that contacts a semiconductor material. This is done with the ELECTRODE statement.

ELECTRODE NAME=<electrode name> <position_parameters>

In ATLAS, we can specify up to 50 electrodes. The position parameters are specified in microns using the X.MIN, X.MAX, Y.MIN, and Y.MAX parameters.

IV-Doping profile

The doping profiles can be specified either analytically or from an input file. The doping statement must contain the doping distribution type, the doping concentration and their types, and the position parameters, Where the position parameters are specified in microns using the x.min, x.max, y.min, and y.max parameters, or by region number or even the material type. For example:

DOPING UNIFORM CONCENTRATION=1E18 P.TYPE MATERIAL=GaN

b. Materials and models specification

After of the structure, materials and electrodes now comes another important step, which is the material parameters and physical models used during the device simulation process. Most of the physical model are defined in the model statement except for some physical models which can be defined in the structure section of the code (such as the impact ionization and some mobility models), however there are some models that can be defined either the model statement or the material section.

I-Material properties specification

All materials are split into three classes: semiconductors, insulators and conductors. Each class requires a different set of parameters to be specified. For semiconductors, these properties include electron affinity, band gap, density of states and saturation velocities carriers' life time ... There are default parameters for material properties used in device simulation for many materials, however, it is preferable for the user to introduce these parameters manually. The syntax of material statement is written as:

MATERIAL <localization> <material_definition>

The material properties of the Gallium Nitride (GaN) and Aluminium Gallium Nitride (AlGaN) used in the code are illustrated in **table 3.3**:

Material parameter	Definition
Taun, Taup	Specify the lifetime of electrons and holes respectively.
$N_{C.F}$, $N_{V.F}$	Specify the conduction and valence bands densities of state dependent temperature
Eg_1300, Eg_2300	Specify energy gap at 300 K for the barriers and quantum well regions.
$Eg_{12}bow$	Specify the bowing parameter of the General Ternary bandgap model.
Egalpha, Egbeta	Specify the alpha and beta coefficients for temperature dependence of bandgap.
Augn, Augp	Specify the Auger coefficients for electrons and holes respectively.
Affinity	Specifies the electron affinity.
copt	Specifies the optical recombination rate for the material.

Well.gamma0	Specifies the Lorentzian gain broadening factor.
well.taup	Specifies the quantum well capture escape model hole capture time.
well.taun,	Specifies the quantum well capture escape model electron capture time.
real.index, imag.index	specify real and imaginary parts of refractive index.
qwell	Specifies that the region is treated as a quantum well for calculation of radiative recombination or gain or both for certain optoelectronic models.
well.taun, well.taup	Specifies the quantum well capture escape model electron/hole capture time.
Wellgamma0	Specifies the Lorentzian gain broadening factor.
Strain	Specifies the strain percentage in the quantum well.
polarization	Apply a piezoelectric polarization calculated using the strain value assigned by the STRAIN parameter.
led	Specifies that the region is to be treated as a light emitting region.

Table 3.3: The material statement parameters used in the simulation

II-Physical models specification

Physical models are specified using the MODELS statement except for impact ionization which is specified in IMPACT statement. Parameters for these models appear on many statements including: MODELS, IMPACT, MOBILITY, and MATERIAL. The physical models can be grouped into five classes: mobility, recombination, carrier statistics, impact ionization, and tunnelling. Atlas activates by default some physical models such as low field mobility model, and density of state temperature dependence with default material parameters, however when these parameters are user-defined, Atlas uses them instead of the default ones in order to calculate these physical models with better mathematic approaches and more accuracy of the results. The physical models specified in our code are illustrated in **table 3.4**.

Model	Definition
FERMI	Activates Fermi-Dirac statistics
SRH	Activates Schokcley-Read-Hall recombination.
AUGER	Activates Auger recombination.
INCOMPLET	Activates the incomplete ionization of impurities

ANALYTIC	Caughey-Thomas model for Concentration and Temperature mobility Dependence
OPTR	Band-band optical recombination, for direct materials only.
BGN	Specifies bandgap narrowing for heavily doped materials (greater than 10^{18} cm^{-3})
PRINT	Lists the run time output, the models and parameters, which will be used during the simulation. This allows the verification of models and material parameters.
SPONTANEOUS	Computes total radiative recombination rate and include it into drift-diffusion equations
WZ.THREE	Wurtzite parameter for the multiband k.p model
K.P	Enables using the k*p model effective masses and band edge energies for drift diffusion simulation.
K.P CV4	Activates the k.p model with spin resolved HH, LH, and CB.
WELL.CNBS, WELL.VNBS	Specify the number of bound states retained for calculation of radiative recombination or gain if the region is treated as a quantum well as specified by the QWELL parameter.

Table 3.4: The physical models used in the simulation

LASER models

There are also other physical models that we employed in the code, where these models are used only for laser simulations, and are cited bellow:

Model	Definition
Laser	Enables the Laser simulation.
s.helm	Specifies that vector or scalar Helmholtz solver will be used for solution for transverse optical modes.
helm.geom	Sets dimenionality and direction of optical eigenmode solver. Possible choices are 2DXY, 1DX,1DY,15DX, and 15DY.

helm.tm	In scalar Helmholtz solver, it allows or blocks a solution for TE, TM transverse modes.
nmodes	The number of total modes. This parameter will differ from NMODES.TRANS only in 3D or in coupled devices. Currently, both parameters have the same effect.
prt.eval	Prints the eigenvalues (propagation constants or eigen frequencies) of the Helmholtz equation on the screen.
photon.energy	Specifies the energy of photons in 2D vector Helmholtz equation
index.model	Specifies whether the simple refractive index model (INDEX.MODEL=0) or the more complex gain dependent refractive index (INDEX.MODEL=1) is used.
gainmod	Specifies the local optical gain model to be used
itmax	Sets maximum number of external VCSEL iterations during photon density calculation. The default value is 30.
Las.rf	Specifies the front mirror reflectivity in percent.
Las.rr	Specifies the rear mirror reflectivity in percent.
fcarrier	Enables the free carrier loss model in Laser.
Las.absorption	Enables the absorption loss model in Laser.
las.loss	Specifies the total losses.

Table 3.5: The laser physical models and parameters used in the simulation

III-Contacts specification

An electrode in contact with semiconductor material is assumed by default to be ohmic. The NAME parameter is used to identify which electrode will have its properties modified. The NUMBER parameter is used to define the electrode number in case there is several electrodes has the same name.

1- Numerical methods

Atlas can solve up to six equations by using different models combinations. For each of the model types, there are basically three types of solution techniques: (a) decoupled equations (GUMMEL), (b) fully coupled equations (NEWTON) and a mixing between both models (BLOCK). The GUMMEL method solves the equations for each variable in turn keeping the other variables constant, and repeating the process until a stable solution is achieved. The

NEWTON method consists of solving the total system of unknowns together. However, the BLOCK method will solve some fully coupled equations while other are decoupled.

Generally, the GUMMEL calculation method is useful when the system of equations is weakly coupled but has only linear convergence. Opposite to the GUMMEL method, the NEWTON method actually is useful when the system of equations is strongly coupled, and has a quadratic convergence. However, it may spend extra time solving the quantities which are essentially constant or weakly coupled. NEWTON method also requires a more accurate initial guess to the problem to obtain convergence. The BLOCK method, in its turn, can provide less simulation time comparing to NEWTON method. GUMMEL can often provide better initial guesses to problems. It can be useful to start a solution with few GUMMEL iterations to generate better guesses or initial solutions, then switch to NEWTON method to complete the solution.

In ALTAS, the specification of the solution method is carried out as follows:

METHOD NEWTON MAXTRAP=10

Where, MAXTRAP parameter specifies the number of times the trap procedure will be repeated in case of divergence. The value of MAXTRAP may range from 1 to 10.

2- Solution specification

Atlas can calculate DC, AC small signals and transient solutions. Obtaining solutions is similar to setting up parametric test equipment for device tests. When a voltage is defined on an electrode in the device, ATLAS then calculates the current through each electrode. ALTAS also calculates internal quantities, such as carrier density and electric fields created through the device.

The solution is obtained by specifying the statement SOLVE INIT which gives an initial guess for the potential and carrier concentrations from the doping profile which help to achieve the convergence for each used equation.

The terminal characteristics calculated by ATLAS is stored in log file by the statement that follows:

LOG OUTFILE=NAME.LOG

The bias sweep to calculate the DC and AC small signal can be done by the next statement:

SOLVE VANODE=0.0 VSTEP=0.1 VFINAL=1.2 NAME=ANODE

SOLVE VANODE=0.0 VSTEP=-0.1 VFINAL=-1.2 NAME=ANODE AC FREQ=1E6

3- Graphical user interface extraction

TonyPlot is a graphical post processing tool for use with all SILVACO simulators and is an integral part of the VWF interactive tools. Tonyplot can operate in stand-alone or along other VWF interactive tools such as DECKBUILD, VWF or SPDB.

To plot a log file or several log files with tony plot, the statements are:

TONYPLOT file1.LOG

TONYPLOT – OVERLAY file1.LOG file.LOG

TONYPLOT FILE1.STR -SET FILE1.SET

TONYPLOT FILE1.LOG -SET FILE1.SET

CHAPTER 4

RESULTS AND DISCUSSION

CHAPTER 4

4.1 Introduction

This chapter illustrates the application of the previous chapters' theoretical considerations in the case of $Al_xGa_{1-x}N$ single quantum well laser structure. The general methodology which allow us to make an advanced analysis of the device optical responses is shown in the previous chapter as well.

The obtained results of a hexagonal compressive strained AlGaN/GaN single quantum well laser, and which are mainly based on the optical gain and the current characteristics, are represented in this chapter. A comparison between two different models is performed; the first is based on the simple parabolic band model whereas the second is based on the perturbation theory (k.p model) for calculating the band structure.

4.2 The device structure

The investigated device structure consists of a thin GaN active layer situated between two 80-nm-thick $Al_xGa_{1-x}N$ barrier regions.

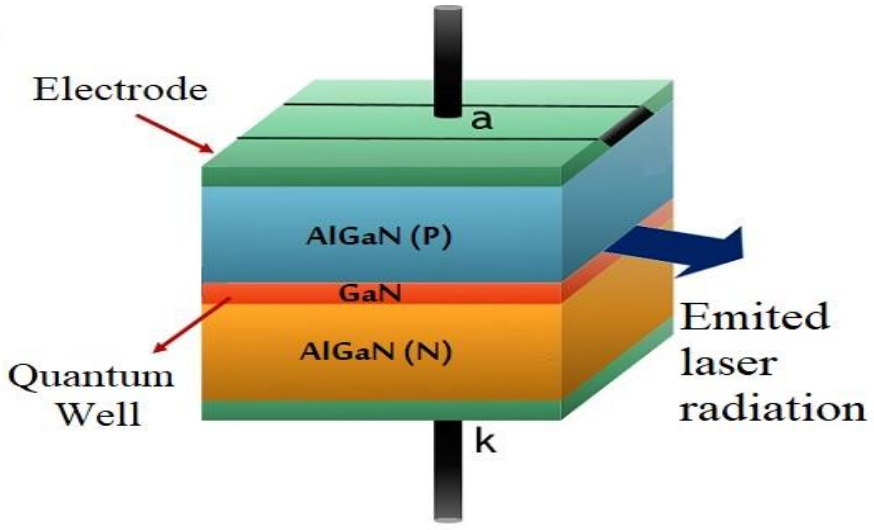

Figure 4.1: The structure of the SQW laser diode

An Aluminum content x = 0.1 and well width considered as L_w = 40 Å are considered as an entry data for modeling, the optical gain spectrum is calculated as a function of the wavelength as well as the transition energy. The device terminals (anode and cathode) are assumed to be Ohmic contacts.

The figure 4.2 illustrates the light intensity distribution along the structure, showing high light intensity around the active region which includes GaN quantum well region (L_w = 40 Å), this region where the optical (electrons-holes) recombination occurs the most.

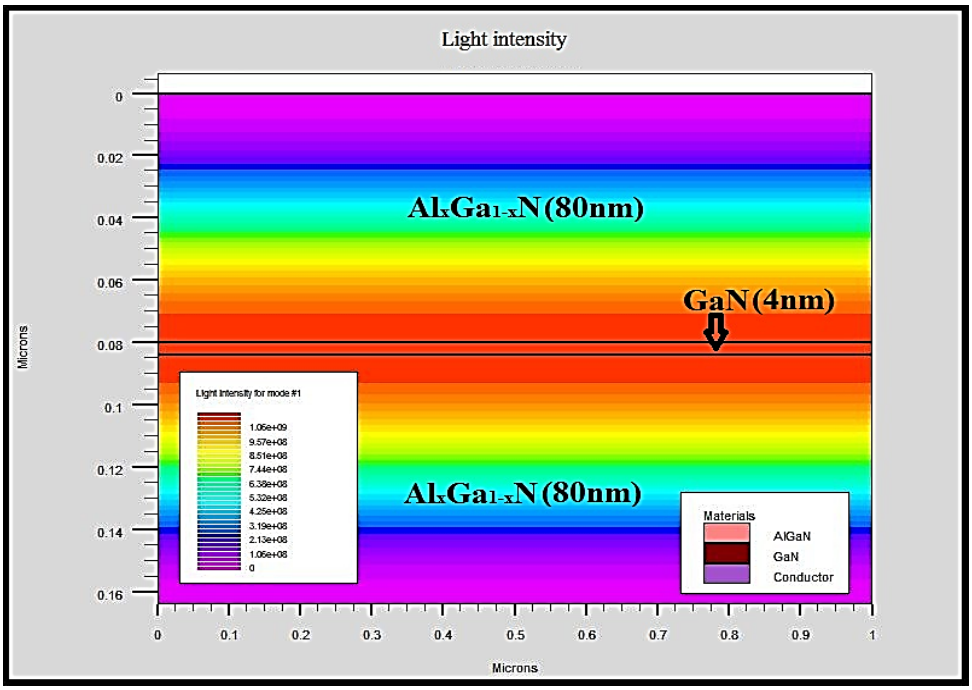

Figure 4.2: The light intensity distribution along the device

The figure 4.3 bellow illustrates the conduction and valence band edge alignment in AlGaN/GaN structure with the application of a compressive strain (Conduction band, Heavy holes, light holes and crystal-field-split-hole bands of the valence band). In AlGaN regions the light hole (LH) band edge of the valence band is higher than the heavy holes (HH) band edge, however in the GaN QW region, and because of the compressive strain application, the heavy hole band (HH) shifts up and the light hole (LH) shifts down, with a slight overall increase of the band gap energy as depicted in the zoomed section, of the figure 4.4.

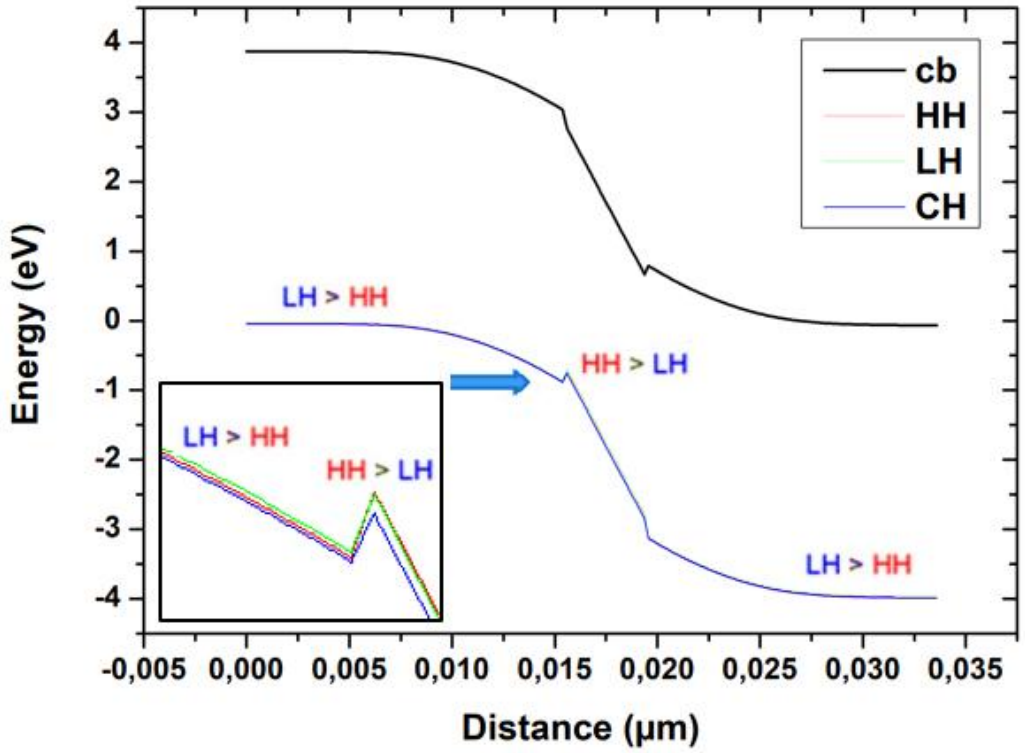

Figure 4.3 AlGaN/GaN conduction and valence band edges of a compressively strained GaN QW on AlGaN barrier layers (including piezo-electric field)

4.3 The band gap energy dependence Aluminum content

One of the most important parameters that affects the band gap energy in the ternary alloys is the molar fraction, which in our case is the Aluminum concentration. Like the **Figure 4.4** clearly shows, the more the Aluminum content raises, the more the band gap energy increases, in the range [2-20] %. Beyond this range, a large amount of dislocations and structural defects will appear, and by consequence, the piezoelectric field will strongly raise which in turn will negatively affect the electrical characteristics and optical responses.

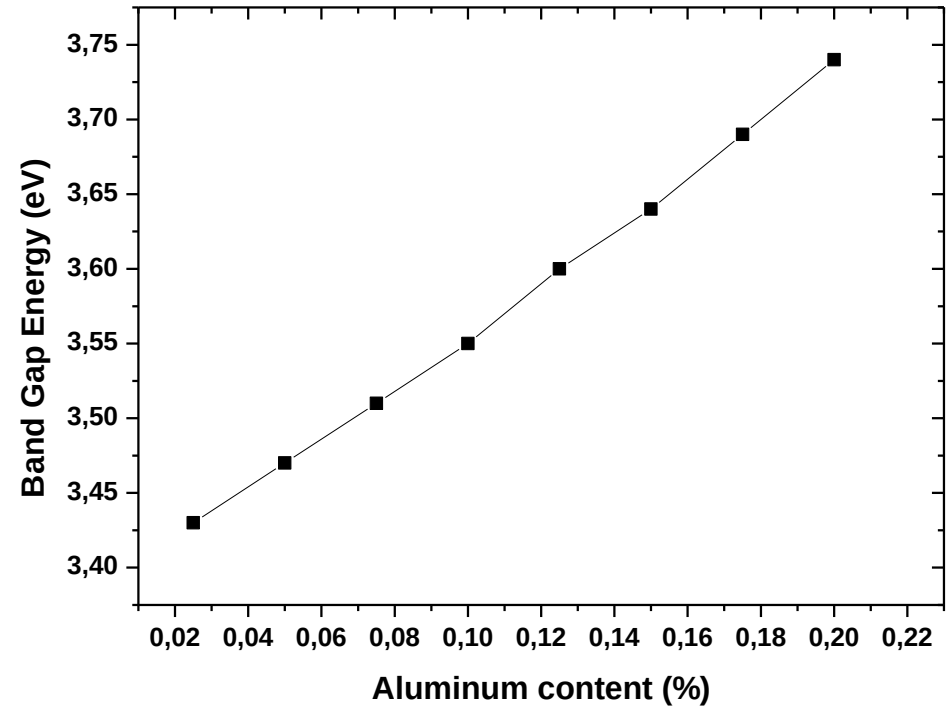

Figure 4.4: The band gap energy dependence Aluminum content

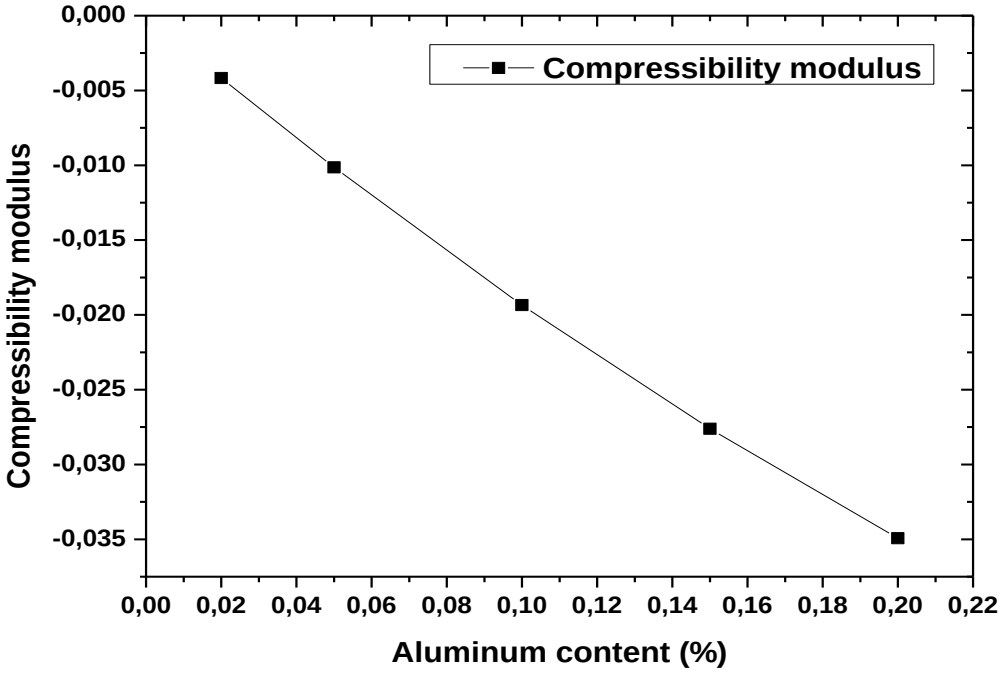

Figure 4.5: The compressibility modulus dependent Aluminum content

The Figure 4.5 illustrates the compressibility modulus – Aluminum concentration dependency. It shows that the device is fully under compressive strain applied to GaN quantum well region from surrounding AlGaN barrier layers. Where the compressibility modulus is calculated by Vegard's law as follows:

$$\beta = \frac{a_{Al_xGa_{1-x}N} - a_{GaN}}{a_{GaN}}$$

$$a_{Al_xGa_{1-x}N} = xa^{AlN} + (1-x)a^{GaN} - bx(1-x)$$

Where: a is the lattice constant, x is Aluminum molar fraction and b is the material bowing parameter.

4.4 The spontaneous emission dependent Aluminum content

One of the most important optical responses of the nitride-based SQW lasers is the spontaneous emission. The analysis of transverse magnetic (TM) and electric (TE) mode light extraction of GaN quantum wells (QWs) based ultraviolet (UV) LD's has been achieved. The transverse electric (TE) and (TM) components of the spontaneous emission of GaN QWs with AlGaN barriers were calculated by using a self-consistent 6-band *k·p* method, which implicates that these modes are strongly dependent on the Aluminum concentration in the barrier layers, where the results indicates that the (TM) component overtakes the (TE) component and becomes the dominant contribution of the spontaneous emission when the Al-content of the AlGaN barrier layers is less than 0.2.

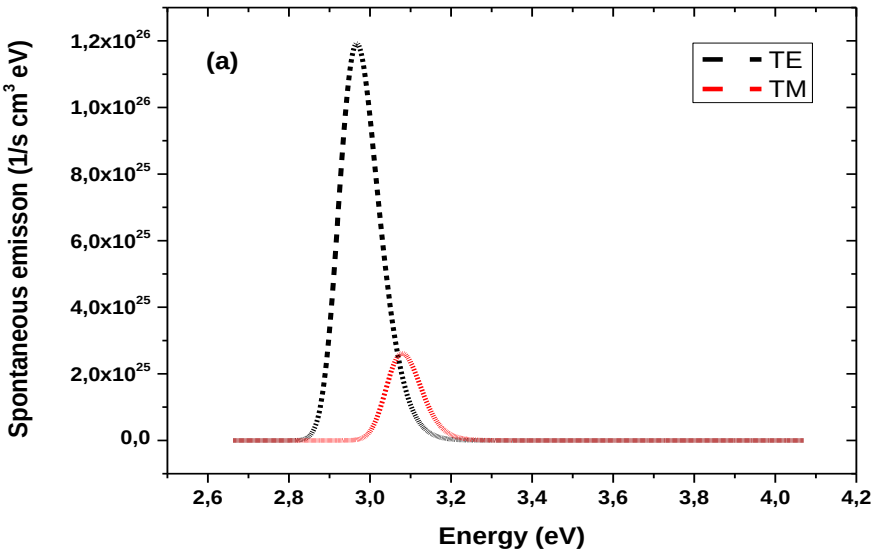

(a) x= 0.3

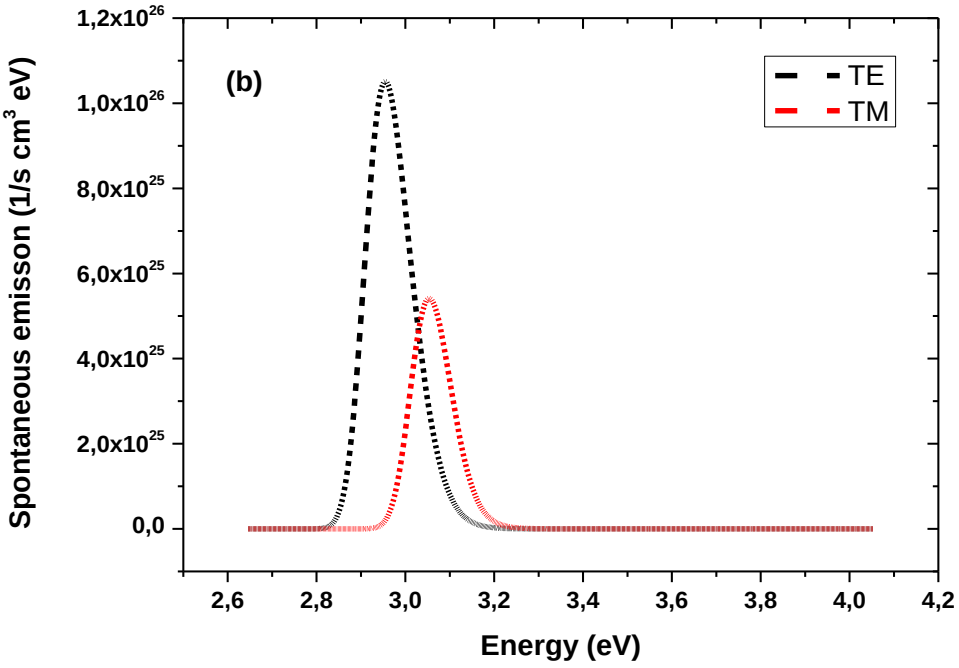
(b)
TE
TM
Spontaneous emisson (1/s cm3 eV)
1,2x10^26
1,0x10^26
8,0x10^25
6,0x10^25
4,0x10^25
2,0x10^25
0,0
2,6
2,8
3,0
3,2
3,4
3,6
3,8
4,0
4,2
Energy (eV)

(b) x=0.25

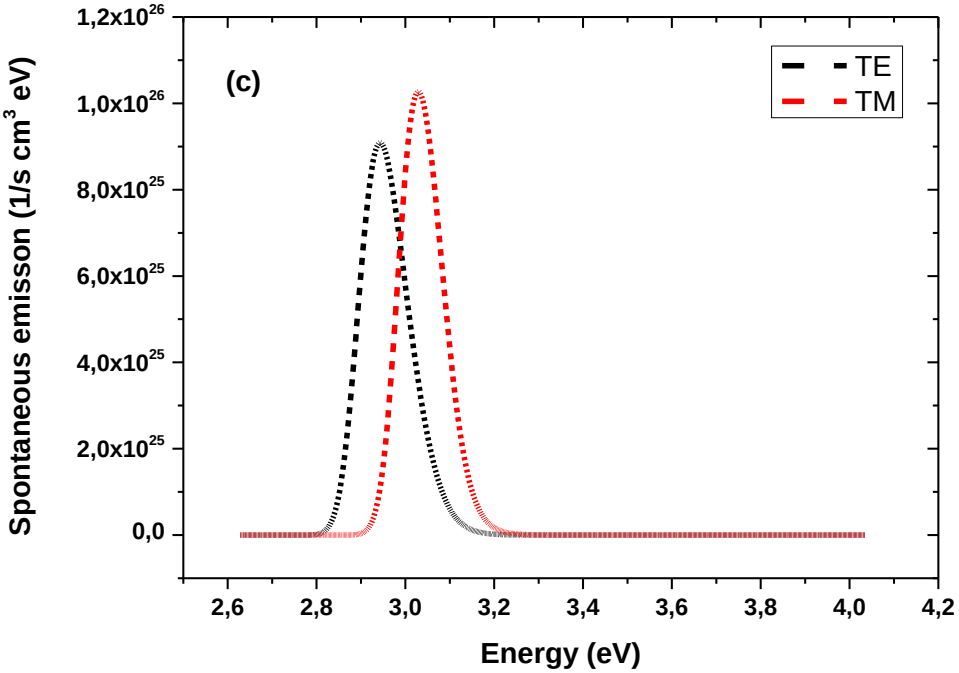
(c)
TE
TM
Spontaneous emisson (1/s cm3 eV)
1,2x10^26
1,0x10^26
8,0x10^25
6,0x10^25
4,0x10^25
2,0x10^25
0,0
2,6
2,8
3,0
3,2
3,4
3,6
3,8
4,0
4,2
Energy (eV)

(c) x=0.2

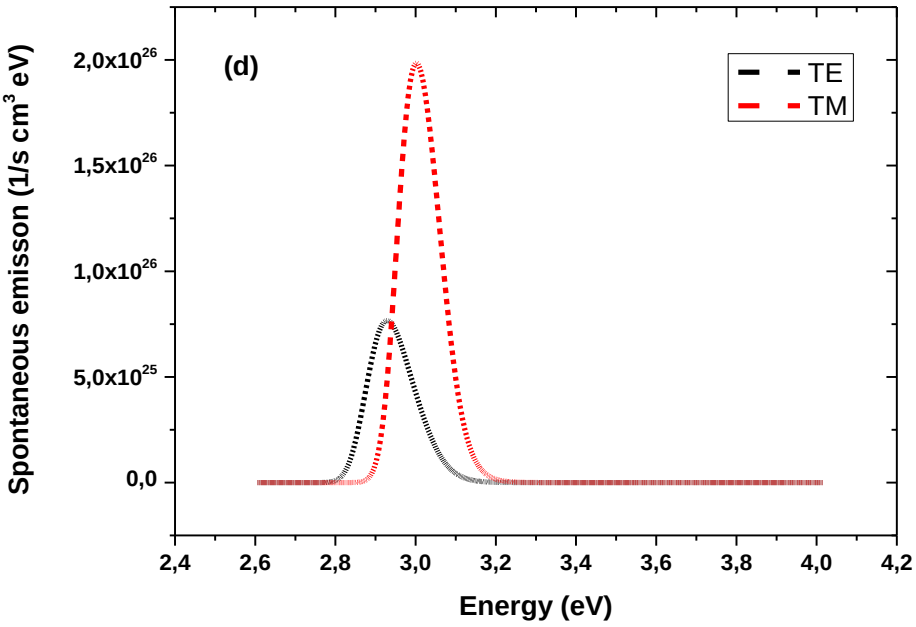

(d) x=0.15

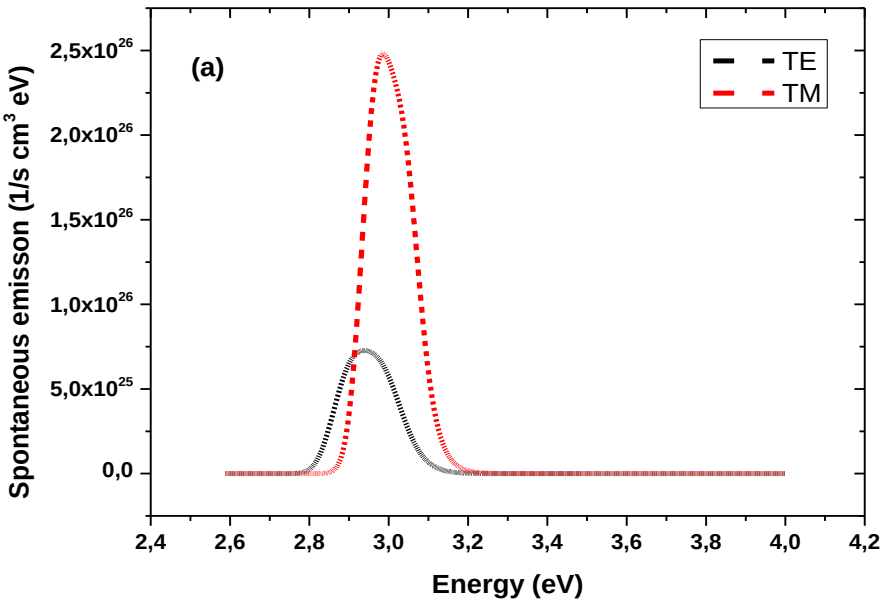

(e) x=0.1

Figure 4.6 The transverse electric (TE) and magnetic (TM) of the spontaneous emission dependent the Al contents: (a) x=0.1, (b) x=0.15, (c) x=0.2, (d) x=0.25 and (e) x=0.3 as function of the transition energy

Coming to the external laser efficiency point of view, the low external quantum efficiency of the UV III-nitride LDs (In the spontaneous emission regime, before the laser operating threshold) is also significantly attributed by the low light extraction efficiency, due to:

1) the total internal reflection from the high refractive index of the nitride semiconductors (n~2.4) in contrast to that of the free space (n = 1).

2) more importantly, the domination of the transverse magnetic (TM) component of the spontaneous emission from the low Al-content AlGaN QWs active region, where (TM) polarization is polarized along the direction normal to the surface, leading to extremely low light extraction efficiency.

4.5 The power spectral density dependent Aluminum content

Besides the spontaneous emission and the optical gain, The Power Spectral Density (PSD) is an important parameter that typically characterizes high power lasers, and is defined as the measure of signal's power content vs transition energy, wave length or frequency. The power spectral density (PSD) also refers to the spectral energy distribution that would be found per unit time. The amplitude of the PSD is normalized by the spectral resolution employed to digitize the signal, and as **Figure 4.7** illustrates, it is manifested as a Gaussian form characterized by its spectral width and amplitude. The last element is dependent on the crystal properties of device material. which is the case here, it is actually affected by the Aluminum content of the barrier layers, where by decreasing the Al content, the amplitude of the power spectral density increases, and slightly shifts the spectrum to larger energies (smaller wavelengths) and vice-versa.

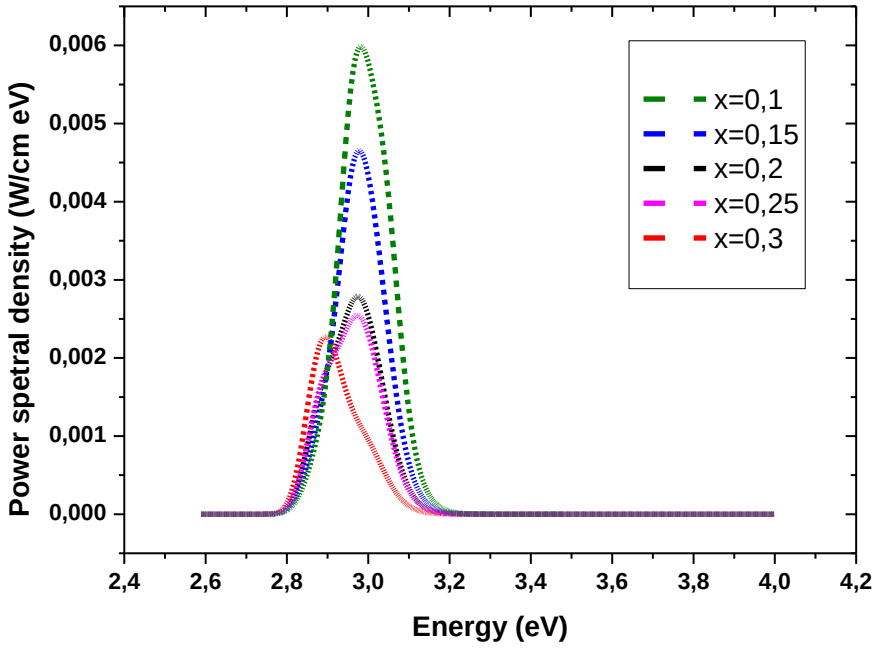

Figure 4.7 The power spectral density dependent the Al contents

(x=0.1, x=.15, x=0.2, x=0.25 and x=0.3) as function of the transition energy

4.6 The optical gain

In this section of the chapter we are going to introduce our work in a comparative way, and that between two methods in optical gain calculation. The gain spectra had been calculated by using a simple parabolic band model and also a multiband formalism based on the perturbation theory (k.p model) that is well suited for crystals with the wurtzite symmetry.

In the first case, we have assumed parabolic energy levels in the quantum well for both the conduction and valence band. In this model there is no valence band mixing, and the momentum matrix element P is set to zero when solving for the band structure. This produces parabolic bands, which is a good approximation for wide gap materials.

However, in the second case, we have assumed parabolic energy levels for electrons while the hole energy levels have been computed via a 6×6 k.p model, all by including a compressive strain effect, applied from the AlGaN barrier layers on the GaN quantum well, which is calculated from lattice mismatch introduced to polarization calculations that enter directly into the drift diffusion calculations as polarization fields. However, the band parameters (band-edges and effective masses) are used directly in the drift diffusion simulations as well as

feeding into the solutions of Schrodinger's equations to calculate the bound state energies. The band parameters and bound state energies are then used to calculate gain, radiative recombination rate and optical absorption.

This model treats the electronic states within the effective mass approximation, over a wide region away from the center of the Brillouin zone, and takes in account the inter-mixing of the hole states, which provide a much more accurate band structure and optical response.

The optical response calculated within this model is more reliable for large spatial changes in effective mass parameters between the well and the barrier region.

4.6.1 The optical gain-carrier density dependence

The calculations are carried out at a temperature of 300 °k, layer thicknesses: L_w = 40 Å GaN quantum well region and L_b = 80 Å $Al_xGa_{1-x}N$ barrier regions with an Aluminum content x = 0.1 as entry data for modeling, the optical gain spectrum was calculated as a function of the wavelength for different doping densities in the range 1×10^{18}-1×10^{19} cm^{-3} as shown in **Figure 4.8** The value of 1×10^{18} cm^{-3}, in fact, can be assumed as the threshold carrier density (transparency density) for the considered device.

As we can see, the increase of the injection level in the active region determines the increase of the maximum optical gain for both the parabolic bands and 6-band k.p models. These behaviors are due to the filling of high states in the conduction and valence bands with the resulting increase of the emission phenomena as observed in similar laser structures. The curves in **Figure 4.8 (a)** and **(b)**, however, are quite different each other. In fact, the optical gain values in **Figure 4.8 (b)** are strongly increased if compared to those reported in **Figure 4.8 (a)** as a consequence of the reduced density of available states due to the non-parabolic model of the valence band. In addition, the gain spectrum calculated using the parabolic band model is rather wide by considering the large energy difference between the quasi-Fermi levels which results from the parabolic band approximation.

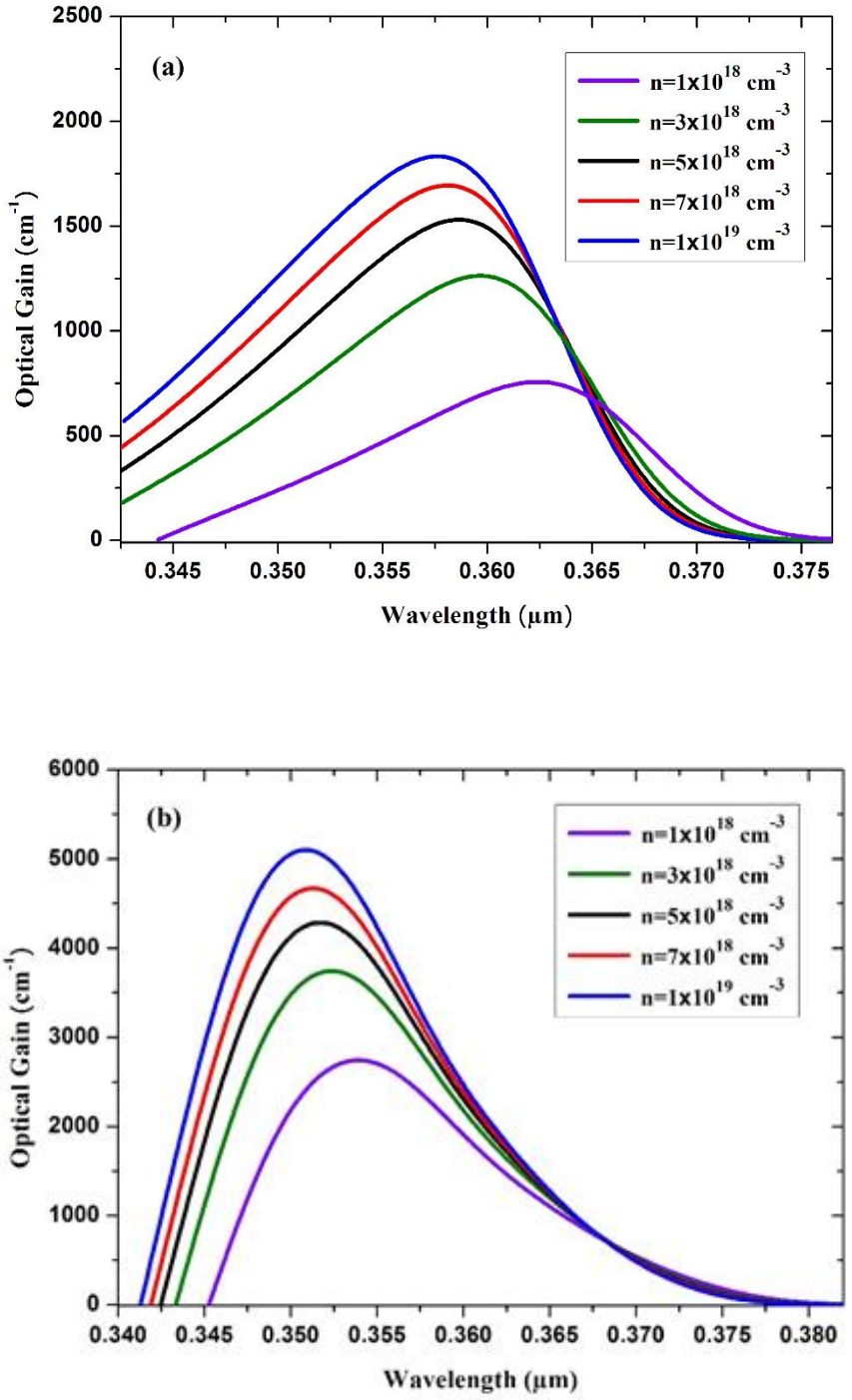

Figure 4.8 Optical gain spectrum in an $Al_{0.1}Ga_{0.9}N/GaN/Al_{0.1}Ga_{0.9}N$ QW laser as a function of the wavelength for different doping densities in the active region at T = 300 K. (a) Parabolic band model. (b) 6-band k.p model.

4.6.2 The optical gain-Aluminum content dependence

The optical gain dependence on the Al molar fraction for n = 1×10^{19} cm^{-3} is shown in **Figure 4.9** It is worth to note that in $Al_xGa_{1-x}N$/GaN QW lasers an increasing value of *x* meaningfully increase the maximum optical gain moving the gain spectrum towards the shorter wavelengths. This shift is due to the increase of the $Al_xGa_{1-x}N$ bandgap calculated as wide as 3.896 eV for x = 0.2 and the change of the quantization energy. At the same time, the increase of the maximum gain value is mainly due to the increase in the optical confinement since the refractive index of the barrier layers tends to become higher than that in the GaN active region.

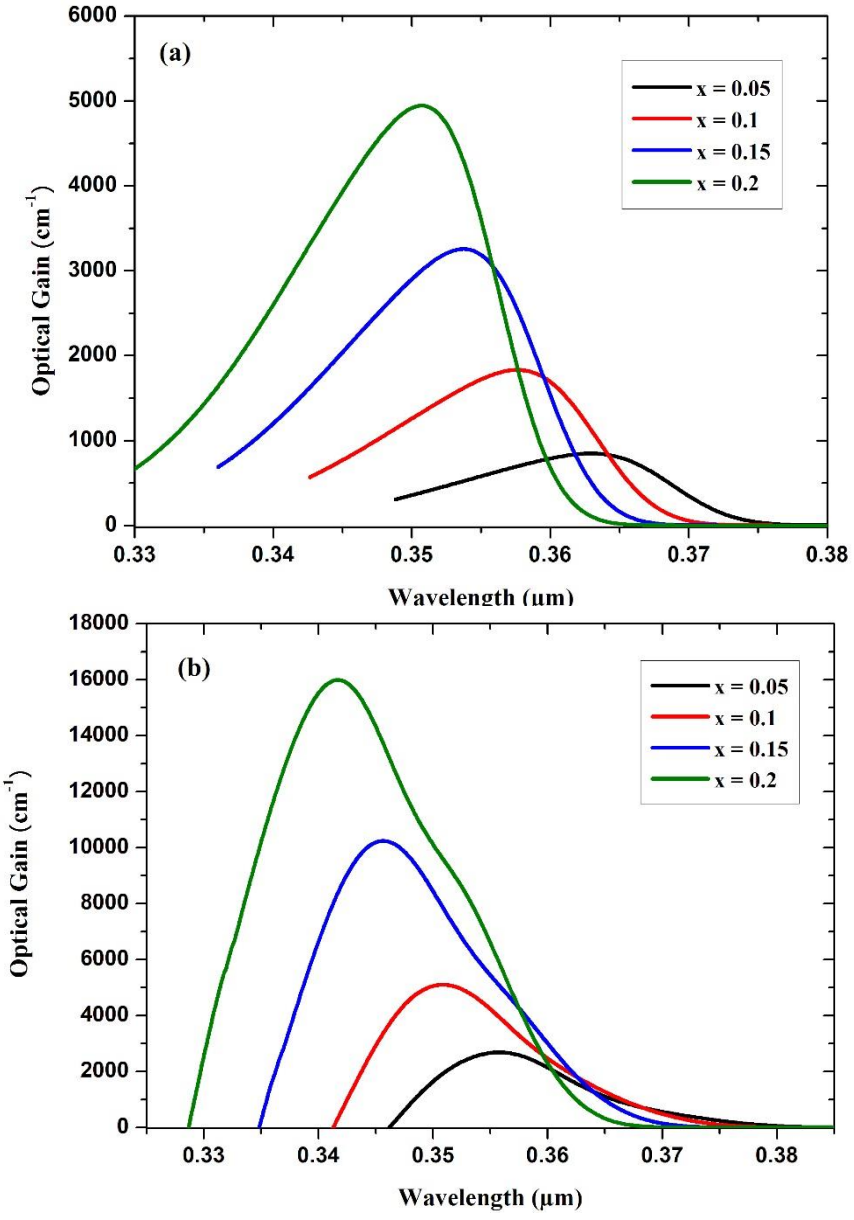

Figure 4.9 The optical gain spectrum as a function of the Al content at *T* = 300 K. (a) Parabolic band model. (b) 6-band k.p model.

4.6.3 The optical gain-well width dependence

A fundamental geometrical parameter in the design of the considered device is the width of the GaN well (L_w). The plot of the maximum optical gain calculated for different values of L_w in the range 30 Å to 60 Å is shown in **Figure 4.10**

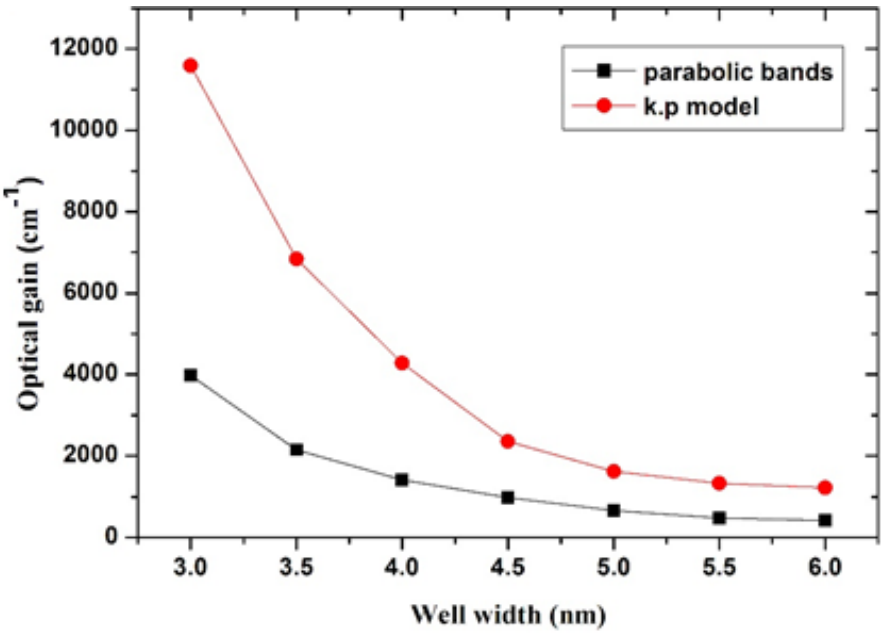

Figure 4.10 Optical gain spectrum as a function of the GaN QW width (x = 0.1 and n = 1×10^{19} cm^{-3}) at T = 300 K.

A wider quantum well penalizes the increase of the optical gain, where, L_w = 40 Å should be assumed as a limit value in this study. In fact, the wider the quantum well is, the stronger electrons and holes are separated by the piezoelectric field and therefore the optical gain reduces. In other words, when the QW width increases, the density of states in this region decreases.

4.6.4 The optical gain-temperature dependence

One of the major elements that affect the optical gain behavior is the temperature, and this is for both parabolic bands and 6-band k.p models, The **Figure 4.11** below illustrates this resonance in function of the transition energy for both models respectively.

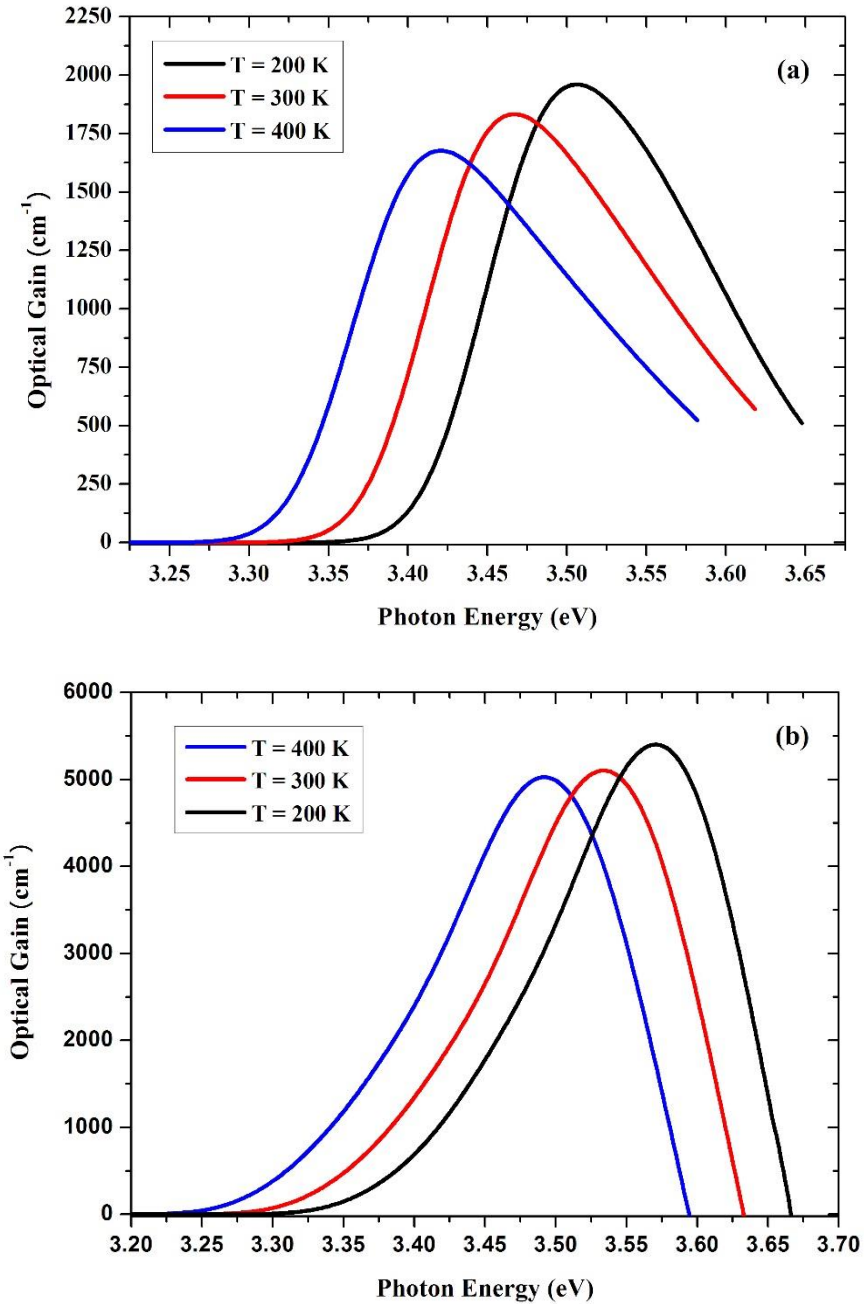

Figure 4.11 The dependence of the optical gain on temperature in the range T= [200, 300, 400] °k for: (a) Parabolic bands model. (b) 6-band k.p model.

From **Figure 4.11**, and with these conditions: (L_w = 40 Å, x = 0.1, and n = 1×10^{19} cm^{-3}), the temperature has an impact on the maximum gain value. In more detail, it tends to decrease as the temperature increase in accordance with the variation of the Fermi-Dirac distributions in Equations. On the other hand, by increasing the temperature, the GaN bandgap shrinks and carriers can scatter to other sub-bands leading to a change of the optical gain spectrum range that tends to shift toward the lower transition energy values.

4.6.5 The quantum well band gap energy-temperature dependence

The temperature-dependent GaN bandgap profile is shown in **Figure 4.13**. As well known, the interatomic spacing increases when the amplitude of the atomic vibrations increases due to an increased thermal energy. This effect causes a dilatation of the lattice and leads to a displacement of the conduction and valence band edges.

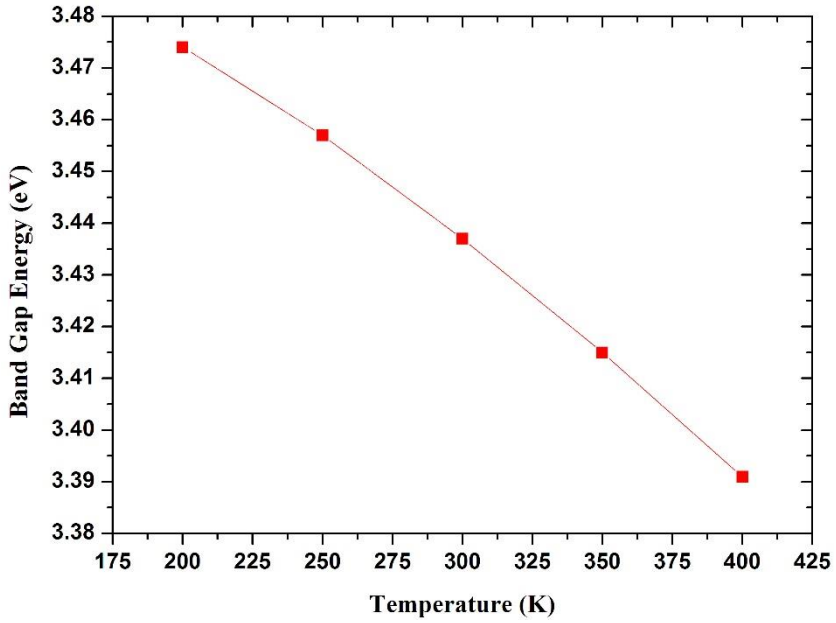

Figure 4.12 GaN bandgap energy as a function of the temperature.

The **Figure 4.13** represents a comparative study results concerning the TE-polarized optical gain spectrum for three different optical gain calculation models (for a carrier density $n=10^{19}cm^{-3}$ and an Aluminum content x=0.1 and a well width L_w=4 nm) which are: the parabolic band model, the 6 band k.p model and an analytic model achieved by Asgari et.Al [251]. The last model, similar to the two other models, calculates the quantum well sub-band energy and related wave-functions of electrons and holes in the active region by taking into account the spontaneous and piezoelectric polarizations of the III-nitride materials which can produce a built in effective electric filed that can change the optical and electrical characterization. The biaxial compression strain increases the mean band gap and splits the degeneracy of the valence band maximum and introduces an anisotropic valence band structure. This model achieves an optical gain maxima of G=1800 cm^{-1} for a transition energy E=3.46 eV, and a larger spectral width.

The calculation of the quantum well sub-band energies and related wave-functions using parabolic band model and the 6-band k.p model have a better introduction of this compressive strain effect (defined in the previous chapter) which introduces more elements and parameters that affects the polarization calculations that enter directly into the drift diffusion calculations as polarization fields, and which in turn has a huge impact on the band parameters (band-edges and effective masses) as well as feeding into the solutions of Schrodinger's equations to calculate the bound state energies, the band parameters and bound state energies are then used to calculate gain. This model achieves a higher optical gain maxima of G=1400 cm^{-1} for a transition energy E=3.42 eV.

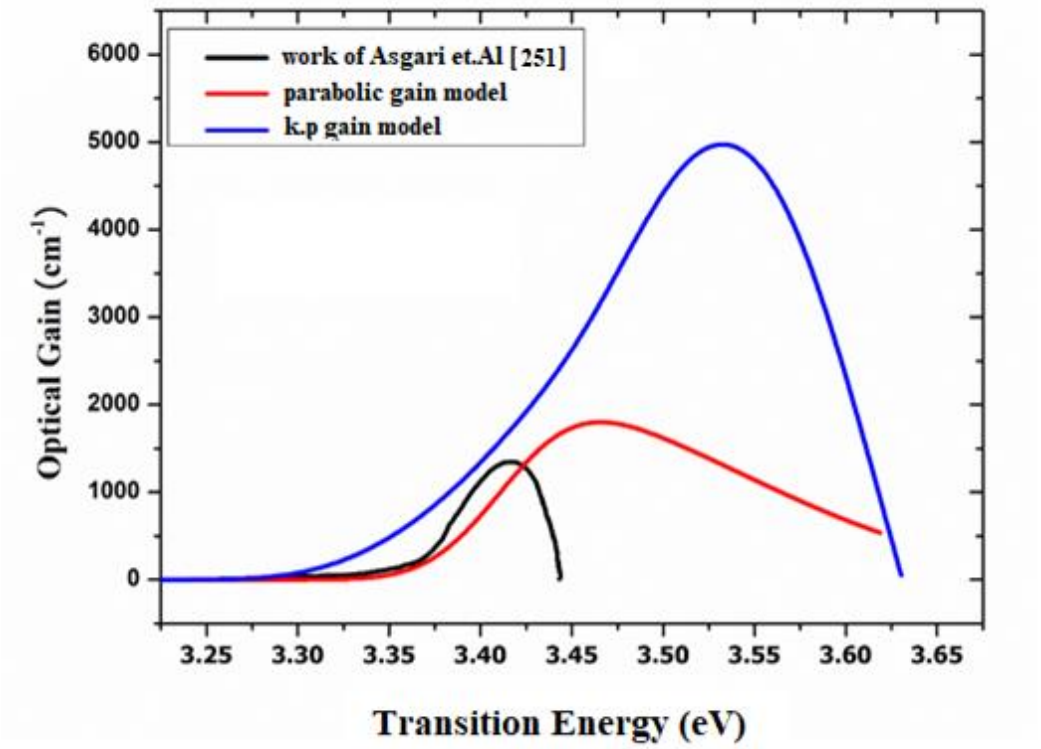

Figure 4.13: TE-polarized optical gain spectrum for (a) parabolic gain model (b) 6-band k.p gain model and (c) work of Asgari et.Al [251]

The the 6-band k.p model, however, has more accurate calculation approaches comparing to the two previous models. Not only this model has a better introduction of the strain effect and its parameters and their impact on the optical response, but it also treats the electronic states within the effective mass approximation with larger strength of the inter-mixing of the hole states which leads to more accurate band structure and optical response over a wide region of the Brillouin zone and which implicates a higher optical gain with a larger spectrum width. The optical gain maxima of this model as illustrated in the **figure 4.13** is more significant and it is equal to 5000 cm^{-1} for a higher transition energy E=3.53 eV (shorter wavelength) and even larger spectral width.

4.7 The threshold current density-temperature dependence

The laser threshold current density variation with temperature in the range 260-340 °K is shown in **Figure 4.14**.

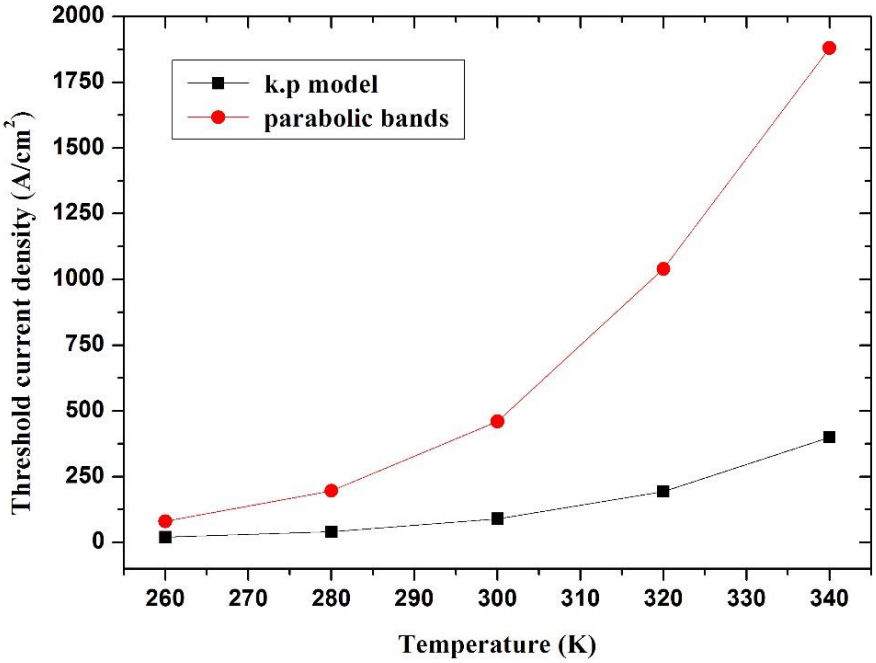

Figure 4.14 The threshold current density dependence on temperature

(L_w = 40 Å, x = 0.1, and n = 1×10^{19} cm^{-3}).

By the use of the k.p model, the increase of the threshold current density with temperature is weaker than the one of the simple parabolic bands model. This increase is on the order of a factor 5 at T = 340 K. However, the minimum current density J_{th} value is around 60 A/cm^2 for both models at very low temperatures. This means that high temperatures affect less the threshold density while using the 6-band k.p model, meanwhile the parabolic band-to-band model is more reliable and affected by high temperatures.

CONCLUSION

Conclusively, we studied by simulation method, using Atlas of Silvaco-TCAD simulator, a compressive-strained hexagonal structure of AlGaN/GaN single quantum well laser diode. An advanced software analysis of the device optical responses, mainly based on the optical gain, was elaborated during this section as well some electrical characteristics.

First we began with illustrating schematic diagrams of the conduction and valence bands structure and the energy band states in the QW, then we have studied the effect of the Aluminum content of the band gap energy which shows an increasing function dependency, besides, the compressibility modulus dependent the Aluminum content in the interval [0.02-0.2] and in which it shows that the device is fully under compressive strain applied to GaN quantum well region from surrounding AlGaN barrier layers.

Then we moved to study one of the most important optical responses of the nitride-based SQW lasers is the spontaneous emission. We did an analysis of transverse magnetic (TM) and electric (TE) mode light extraction of GaN quantum well (QW) of ultraviolet emitting (UV) LD. The transverse electric (TE) and (TM) components of the spontaneous emission of GaN QW with AlGaN barriers were calculated by using a self-consistent 6-band k·p method, which implicates that these modes are strongly dependent on the Aluminum concentration in the barrier layers, where each time we plotted the spontaneous spectrums for both (TE) and (TM) modes for a specific Al content varying from 0.1 to 0.3. The results indicate that the (TM) component overtakes the (TE) component and becomes the dominant contribution of the spontaneous emission when the Al-content of the AlGaN barrier layers is less than 0.2.

Besides the spontaneous emission, The Power Spectral Density (PSD) is an important parameter that typically characterizes high power lasers. The results, manifested as a Gaussian form characterized by its spectral width and amplitude, we were varying the Al content from 0.1 to 0.3 by a step of 0.05 and observing the behaviour of the spectrum for each Al concentration. The results show that by decreasing the Al content, the amplitude of the power spectral density increases, and slightly shifts the spectrum to larger energies (smaller wavelengths) and vice-versa, where for x=0.3 the PSD is equal 0.024 W/cm eV for transition energy equivalent to 2.9 eV, however, for x=0.1 the PSD reached 0.06 W/cm eV for higher transition energy (shorter wavelength) equivalent to 2.97 eV.

Coming the main aspect of the study, and the most important characteristic of our device, which is the laser optical gain. The results were introduced in a comparative way, and that between two methods in optical gain calculation. As mentioned before, the gain spectra had been calculated by using a simple parabolic band model and also a multiband formalism based on the perturbation theory (k.p model) which is well suited for crystals with the wurtzite symmetry.

Using the first model, we have assumed parabolic energy levels in the quantum well for both the conduction and valence band with no valence band mixing, and the momentum matrix element P is set to zero when solving for the band structure.

However, in the second case, we have assumed parabolic energy levels for electrons while the hole energy levels have been computed via a 6×6 k.p model, all by including the compressive strain effect. This model treats the electronic states within the effective mass approximation, over a wide region away from the center of the Brillouin zone, and takes in account the inter-mixing of the hole states, which provide a much more accurate band structure and optical response.

The effect of the quantum well (QW) width, carrier density, and aluminum (Al) concentration in the barrier layers on the optical characteristics are investigated by means of a careful modeling analysis in a wide range of temperature.

- The Carrier density dependency:

The calculations are carried out at the temperature T= 300 °k, a well width L_w = 40 Å, a barrier width L_b = 80 Å and Aluminum content x = 0.1 as entry data for modeling. The optical gain spectrum was calculated as a function of the wavelength for carrier densities n =1×10^{18} to 1×10^{19} cm^{-3}.

The results show that the more the carrier injection is, the higher the optical gain maxima reaches for both the parabolic bands and 6-band k.p models. However, the optical gain maximum of second model is about 3-4 times those of the parabolic bands model.

- The Aluminum concentration dependency:

The optical gain dependence is achieved for an Al molar fraction x = 0.05 to 0.2 for a carrier density n=1×10^{19} cm^{-3}. Increasing the value of x meaningfully increases the maximum

optical gain and shifts the gain spectrum, by around 0.01µm, towards shorter wavelengths. Where the gain maximum of k.p model is about 3 times those of the parabolic bands model.

- The quantum well width dependency:

The plot of the maximum optical gain calculated for different values of the GaN quantum well width (L_w) in the range 30 Å to 60 Å (at x = 0.1, n = 1×10^{19} cm^{-3} and T = 300 °K) for both parabolic band and 6-band k.p models demonstrates that the wider the quantum well is, the lower the optical gain maxima is. However, the optical gain maxima using 6-band k.p model is higher than the parabolic bands gain maxima especially for L_w=[30 - 45] Å, from an optical gain G=1100 cm^{-1} and G=2700 cm^{-1} for L_w = 45 Å to G=4000 cm^{-1} and G=11700 cm^{-1} for L_w = 30 Å and this is for the parabolic bands model and the 6-band k.p model respectively.

- The temperature dependency:

The optical gain in function of transition energy dependent the temperature plots are carried out (for L_w = 40 Å, x = 0.1, and n = 1×10^{19} cm^{-3}) for both parabolic bands and 6-band k.p models in the range T = [200-400] °K.

The results show for both models that the increase of temperature leads the maximum gain to decrease and shifts toward the lower transition energy values. As well as the decrease of GaN band gap energy by the temperature increase over the same range (from 3.475eV at 200 °K to 3.39eV at 400 °K).

Our work completes with an important electrical characteristic which the laser threshold current density-temperature dependence in the range 260-340 °K (for L_w = 40 Å, x = 0.1, and n = 1×10^{19} cm^{-3}).

The results show that by the use of the k.p model, the increase of the threshold current density with temperature is weaker than the one of the simple parabolic bands model. This increase is on the order of a factor 5 at T = 340 K. However, the minimum current density J_{th} value is around 60 A/cm^2 for both models at very low temperatures. This means that high temperatures affect less the threshold density while using the 6- band k.p model, meanwhile the parabolic band-to-band model is more reliable and affected by high temperatures.

As future work, we tend to work on different laser structures as the GRIN SCH (graded index separated confinement heterostructure) laser structure and the multi-quantum well structure with a better focus on the well widths impact on the optical responses and study deeply the threshold current density characteristic of the laser.

REFERENCES

REFERENCES

[1] K. M. Yu, Z. Liliental-Weber, W. Walukiewicz, W. Shan, J. W. Ager III, S. X. Li, R. E. Jones, and E. E. Haller, H. Lu and W. J. Schaff, "On the crystalline structure, stoichiometry and band gap of InN thin films", Appl. Phys. Lett. 86, 071910, (2005).

[2] S. C. Jain, M. Willander, J. Narayan, and R. V. Overstraeten, "III-nitrides: Growth, characterization, and properties", J. Appl. Phys. 87, 965, (2000).

[3] S. N.Mohammad and H. Morkoç, "Progress and prospects of group-III nitride Semiconductors", Prog. Quant. Electr. 20, 361, (1996).

[4] F. Fichter, "Uber aluminumnitride", Z. Anorg. Chem. 54, 322, (1907).

[5] F. Fichter, and F. Schroter, Berichte der Deutschen Chemischen Gesellschaft, 43, 1465, (1910).

[6] V.C.Johnson, J. B. Parsons and M. C.Crew, "Nitrogen compounds of gallium", J. Phys. Chem. 36, 2588, (1932).

[7] H. P. Maruska, J.J. Tietjen, "The preparation and properties of vapor-deposited single-crystalline GaN", Appl. Phys. Lett. 15, 327, (1969).

[8] H. M. Manasevit, F. M. Erdmann and W. I. Simpson, "Use of metalorganics preparation of semiconductor materials; IV. Nitrides of Aluminum and Gallium". J. Electrochem. Soc. 118, 1864, (1971).

[9] S. Yoshida, S. Misawa and A. Itoh, "Epitaxial growth of aluminum nitride films on sapphire by reactive evaporation", Appl. Phys. Lett. 26, 461, (1975).

[10] H. Amano, M. Kito, K. Hiramatsu, and I. Akasaki, "P-Type Conduction in Mg-doped GaN treated with Low-Energy Electron Beam Irradiation", Jpn. J. Appl. Phys. 28, L2112, (1989).

[11] S. Nakamura, T. Mukai, M.Senoh and N. Iwasa, "Thermal annealing effects on p-type Mg-doped GaN films", Jpn. J. Appl. Phys. 31, L139, (1992).

[12] S. Nakamura, M. Senoh and T. Mukai "High-power lnGaN/GaN double-heterostructure violet light emitting diodes", Appl. Phys. Lett. 62, 2390, (1993).

[13] S. Nakamura, M. Senoh, S. Nagahama, N. Iwasa, T. Yamada, T. Mukai, T. Matsushita, Y. Sugimoto, and H. Hiyoku, "Room-temperature continuous-wave operation of InGaN multi-quantum-well-structure laser diodes with a long lifetime", Appl. Phys. Lett. 70, 868, (1997).

[14] A. Yasan, R. McClintock, K. Mayes, S. R. Darvish, H. Zhang, P. Kung, M. Razeghi, S. K. Lee and J. Y. Han, "Comparison of ultraviolet light-emitting diodes with peak emission at 340 nm grown on GaN substrate and sapphire", Appl. Phys. Lett. 81, 2151, (2002).

[15] A. Yasan, R. McClintock, K. Mayes, D. Shiell, L. Gautero, S. R. Darvish, P. Kung and M. Razeghi, "4.5 mW Operation of AlGaN-based 267 nm deep ultraviolet light-emitting diodes", Appl. Phys. Lett. 83, 4701, (2003).

[16] J. Wu, "When group-III nitrides go infrared: New properties and perspectives", J. Appl. Phys. 106, 011101, (2009).

[17] A. J. Sierakowskia and L. F. Eastman, "Analysis of schottky gate electron tunneling in polarization induced AlGaN/GaN high electron mobility transistors", J. Appl. Phys. 86, 3398, (1999).

[18] Y. F. Wu, B. P. Keller, P. Fini, S. Keller, T. J. Jenkins, L. T. Kehias, S. P. DenBaars, and U. K. Mishra, "High Al-content AlGaN/GaN MODFETs for ultrahigh performance" IEEE Electron Device Lett. 19, 50, (1998).

[19] S. T. Sheppard, K. Doverspike, W. L. Pribble, S. T. Allen, J. W. Palmour, L. T. Kehias, and T. J. Jenkins, "High-power microwave GaN/AlGaN HEMTs on semi-insulating silicon carbide substrates" IEEE Electron Device Lett. 20, 161, (1999).

[20] S.J. Pearton and F. Ren, "GaN electronics", Advanced Materials 12, 1571, (2000).

[21] H. Morkoc, A. D. Carlo, R. Cingolani, "GaN-based modulation doped FETs and UV detectors" SolidState Electron. 46, 157, (2002).

[22] A.G. Bhuiyan, A. Hashimoto and A. Yamamoto, "Indium nitride InN.: A review on growth, characterization and properties", J. Appl. Phys. 94, 2779, (2003).

[23] P. S. Zory, Quantum Well Lasers, Academic Press, (1993).

[24] P. V. Mena, S.-M. Kang, and T. A. DeTemple, "Rate-equation-based laser models with a single solution regime," Journal of Lightwave Technology, vol. 15, no. 4, pp. 717–729, (1997).

[25] D. S. Gao, S. M. Kang, R. P. Bryan, and J. J. Coleman, "Modeling of quantum-well lasers for computer-aided analysis of optoelectronic integrated circuits," IEEE Journal of Quantum Electronics, vol. 26, no. 7, pp. 1206–1216, (1990).

[26] S. Ghoniemy, L. MacEachern, and S. Mahmoud, "Extended robust semiconductor laser modeling for analog optical link simulations," IEEE Journal on Selected Topics in Quantum Electronics, vol. 9, no. 3, pp. 872–878, (2003).

[27] M. Dehghan and P. Derakhshan-Barjoei, "A novel dynamic analysus and simulation for quantum-well distributed feedback laser," Progress In Electromagnetics Research B, vol. 3, pp. 105–114, (2008).

[28] G. P. Agrawal, Fiber-Optic Communication Systems, John Wiley and Sons, New York, NY, USA, (1997).

[29] B. P. C. Tsou and D. L. Pulfrey, "A versatile SPICE model for quantum-well lasers," IEEE Journal of Quantum Electronics, vol. 33, no. 2, pp. 246–254, (1997).

[30] N. Bewtra, D. A. Suda, G. L. Tan, F. Chatenoud, and J. M. Xu, "Modeling of quantum-well lasers with electro-opto-thermal interaction," IEEE Journal on Selected Topics in Quantum Electronics, vol. 1, no. 2, pp. 331–340, (1995).

[31] A. R. Sterian, "Coherent radiation generation and amplification in erbium doped systems," in Advances in Optical Amplifiers, P. Urquhart, Ed., InTech, Vienna, Austria, (2011).

[32] A. R. Sterian, Amplificatoare Optice, Editura Printech, Bucureşti, Romania, (2006).

[33] G. Mattioli, M. Scalia, and C. Cattani, "Analysis of large-amplitude pulses in short time intervals: application to neuron interactions," Mathematical Problems in Engineering, vol. 2010, Article ID 895785, 15 pages, (2010).

[34] A. R. Sterian and F. C. Maciuc, "Numerical model of an EDFA based on rate equations," in the 12th International School on Quantum Electronics Laser Physics and Applications, vol. 5226 of Proceedings of SPIE, pp. 74–78, (2003).

[35] A. R. Sterian, Laserii in ingineria electrica, Editura Printech, Bucureşti, Romania, (2003).

[36] E. Ştefănescu, A. R. Sterian, and P. Sterian, "Study on the fermion systems coupled by electric dipol interaction with the free electromagnetic field," in Advanced Laser Technologies, vol. 5850 of Proceedings of SPIE, pp. 160–165, (2005).

[37] E. Stefanescu, P. Sterian, and A. R. Sterian, "The Lindblad dynamics of a Fermi system in a particle dissipative environment," in ALT '02 International Conference on Advanced Laser Technologies, Proceedings of SPIE, pp. 160–168, September (2002).

[38] A. Sterian and V. Ninulescu, "Nonlinear phenomena in erbium-doped lasers," in the International Conference on Computational Science and Its Applications (ICCSA '05), O. Gervasi et al., Ed., vol. 3482 of Lecture Notes in Computer Science, pp. 643–650, (2005).

[39] A. D. Petrescu, A. R. Sterian, and P. E. Sterian, "Solitons propagation in optical fibers computer experiments for students training," in the International Conference on Computational Science and its Applications (ICCSA '07), O. Gervasi and M. L. Gavrilova, Eds., vol. 4705 of Lecture Notes in Computer Science, pp. 450–461, (2007).

[40] A. R. Sterian, Mecanica cuantică, Omnia Univ. S.A.S.T., Braşov, Romania, (2008).

[41] A. R. Sterian, "Computer modeling of the coherent optical amplifier and laser systems," in the International Conference on Computational Science and its Applications (ICCSA '07), vol. 4705 of Lecture Notes in Computer Science, pp. 436–449, (2007).

[42] C. H. Lee, T. H. Yoon, and S. Y. Shin, "Period doubling and chaos in a directly modulated laser diode," Applied Physics Letters, vol. 46, no. 1, pp. 95–97, (1985).

[43] R. Nagarajan, M. Ishikawa, T. Fukushima, R. S. Geels, and J. E. Bowers, "High speed quantum-well lasers and carrier transport effects," IEEE Journal of Quantum Electronics, vol. 28, no. 10, pp. 1990–2008, (1992).

[44] C. Cattani and E. Nosova, "Transversal waves in nonlinear Signorini model," in the International Conference on Computational Science and Its Applications (ICCSA '08), vol. 5072 of Lecture Notes in Computer Science, pp. 1181–1190, (2008).

[45] C. Cattani, "Harmonic wavelets towards the solution of nonlinear PDE," Computers & Mathematics with Applications, vol. 50, no. 8-9, pp. 1191–1210,View at: Publisher Site | Google Scholar | Zentralblatt MATH | MathSciNet, (2005).

[46] C. Cattani and I. Bochicchio, "Wavelet analysis of bifurcation in a competition model," in the 7th International Conference on Computational Science (ICCS '07), vol. 4488 of Lecture Notes in Computer Science, pp. 990–996, 2007.

[47] L. Esaki and R. Tsu, "Superlattice and negative differential conductivity in semiconductor lasers," ZBM. J. Res. Develop., vol. 14, pp. 61-68, (1970).

[48] R. Dingle, A. C. Gossard, and W. Wiegmann, "Direct observation of superlattice formation in a semiconductor heterostructure," Phys. Rev, Lett., vol. 34, pp. 1327-1330, (1975).

[49] J. P. van der Ziel, R. Dingle, R. C. Miller, W. Wiegmann, and W. A. Nordland Jr., "Laser oscillation from quantum well states in very thin GaAl-A10.2Ga0,8As multilayer structures," Appl. Phys. Lett. vol. 26, pp. 463-465, (1975).

[50] N. Holonyak, Jr., R. M. Kolbas, R. D. Dupuis, and P. D. Dapkus, "Quantum-well heterostructure lasers," ZEEE J. Quantum Electron., pp. 170-181, (1980).

[51] W. T. Tsang, "Extremely low threshold (A1Ga)As modified multi-quantum well heterostructure lasers grown by molecular beam epi- taxy," Appl. Phys. Lett., vol. 39, pp. 786-788, (1981).

[52] T. Fujji, S. Yamakoshi, K. Nanbu, 0. Wada, and S. Hiyamizu, "MBE growth of extremely high-quality GaAs-AlGaAs GRIN-SCH lasers with a superlattice buffer layer," J. Vac. Sci. Technol., vol. 2, pp. 259-261, (1984).

[53] R. Chin, N. Holonyak, Jr., B. A. Bojak, K. Hess, R. D. Dupuis, and P. D. Dapkus, ''Temperature dependence of threshold current for quantum well AlGaAs-GaAs heterostructure laser diodes," Appl. Phys. Lett., vol. 36, pp. 19-21, (1979).

[54] K. Hess, B. A. Bojak, N. Holonyak, Jr., R. Chin, and P. D. Dapkus, "Temperature dependence of threshold current for a quantum-well heterostructure laser," Solid-State Electron., vol. 23, pp. 585-589, (1980).

[55] Y. Arakawa and H. Sakaki, "Multi-quantum well laser and its temperature dependence of the threshold current," Appl. Phys. Lett., vol. 45, pp. 939-941, (1982).

[56] Y. Arakawa, K. Vahala, and A. Yariv, "Quantum noise and dynamics in quantum well and quantum wire lasers," Appl. Phys. Lett., vol. 45, pp. 950-952, (1984).

[57] Y. Arakawa, and A. Yariv, "Theory of gain, modulation response, and spectral linewidth in AlGaAs quantum well lasers," ZEEE J. Quantum Electron., vol. QE-21, pp. 1666-1674, (1985).

[58] Y. Arakawa, K. Vahala, and A. Yariv, "Dynamic and spectral properties in semiconductor lasers with quantum well and wire effects," presented at the 2nd Int. Conf. Modulated Semiconductor Structures, Kyoto, Japan, (1985).

[59] S.P. DenBaars, D. Feezell, K. Kelchner, S. Pimputkar, Development of gallium-nitride-based light-emitting diodes (LEDs) and laser diodes for energy-efficient lighting and displays, Acta Materialia 61, 945-951, (2013).

[60] F. Bouzid, L. Dehimi, F. Pezzimenti, M. Hadjab, A.H. Larbi, Numerical simulation study of a high efficient AlGaN-based ultraviolet photodetector, Superlattice. Microst. 122, 57-73, (2018).

[61] E.F. Schubert, J.K. Kim, Solid-state light sources getting smart, Science 308, 1274, (2005).

[62] F. Bouzid, F. Pezzimenti, L. Dehimi, M. L. Megherbi, F.G. Della Corte, Numerical simulations of the electrical transport characteristics of a Pt/n-GaN Schottky diode, Jpn. J. Appl. Phys. 56, 094301, (2017).

[63] Y. Marouf, L. Dehimi, F. Bouzid, F. Pezzimenti, F.G. Della Corte, Theoretical design and performance of In x Ga1-xN single junction solar cell, Optik, 163, 22-32, (2018).

[64] F. Bouzid, L. Dehimi, F. Pezzimenti, Performance Analysis of a Pt/n-GaN Schottky Barrier UV Detector, J. Electron Mater. 46, 6563-6570, (2017).

[65] E. Monroya, F. Guillota, S. Lecontea, III-Nitride Nanostructures for Infrared Optoelectronics, ACTA PHYSICA POLONICA A, Vol 110, (2006).

[66] M. Ikeda, T. Mizuno, M. Takeya, S. Goto, S. Ikeda, T. Fujimoto, Y. Ohfuji, and T. Hashizu, High-power GaN-based semiconductor lasers, Physica statusn solidi, No. 6, 1461–1467, (2004).

[67] A. Asgari, S. Dashti, Optimization of optical gain in AlxGa1-xN/GaN/AlxGa1-xN strained quantum well laser, Optik, 123, 1546-1549, (2012).

[68] R. M. Farrell, D. A. Haeger, P. S. Hsu, M. C. Schmidt, K. Fujito, D. F. Feezell, S. P. DenBaars, J. S. Speck, S. Nakamura, High-power blue-violet AlGaN-cladding-free m-plane InGaN/GaN laser diodes, Applied Physics Letters Vol 99, Issue 17, 171113, (2011).

[69] Vurgaftman I and Meyer J R 2003 Band parameters for nitrogen-containing semiconductors J. Appl. Phys. 94 3675–96

[70] H. Morkoç, S. Strite, G. Gao, M. Lin, B. Sverdlov and M. Burns? Large-band-gap SiC, III-V nitride, and II-VI ZnSe-based semiconductor device technologies J. Appl. Phys. 76 1363–98, (1994).

[71] B. Haskell, F. Wu, S. Matsuda, M. Craven, P. Fini, S. DenBaars, J. Speck and S. Nakamura, Structural and morphological characteristics of planar (1120̄) a-plane gallium nitride grown by hydride vapor phase epitaxy Appl. Phys. Lett. 83 1554–6 155, (2003).

[72] N. Gardner, J. Kim, J. Wierer, Y. Shen and M. Krames, Polarization anisotropy in the electroluminescence of m-plane InGaN–GaN multiple-quantum-well light-emitting diodes Appl. Phys. Lett. 86 111101, (2005).

[73] S. Chichibu, M. Kagaya, P. Corfdir, J. Ganière, B. Deveaud-Plédran, N. Grandjean, S. Kubo and K. Fujito, Advantages and remaining issues of state-of-the-art m-plane freestanding GaN substrates grown by halide vapor phase epitaxy for m-plane InGaN epitaxial growth Semicond. Sci. Technol. 27 024008, (2012).

[74] M. A. Mastro, O. M. Kryliouk, T. J. Anderson, A. Davydov and A. Shapiro,"Influence of polarity on GaN thermal stability", J. Cryst. Growth 274, 38, (2005).

[75] J. Rouviére, J. Weyher, M. Seelman-Eggebert and S. Porowski, "Polarity determination for GaN films grown on (0001) sapphire and high-pressure grown GaN single crystal", Appl. Phys. Lett. 73, 668, (1998).

[76] O. Ambacher, "Growth and applications of Group III-nitrides", Journal of Physics D: Applied Physics 31, 2653, (1998).

[77] T. D. Veal, C. F. McConville and W. J. Schaff, "Indium Nitride and Related Alloys", CRC Press Taylor & Francis Group, Chapter 2, (2010).

[78] T. Sugahara, H. Sato, M. Hao, Y. Naoi, S. Kurai, S. Tottori, K. Ymashita, K. Nishimo, L. T. Romano and S. Sakai,"Direct evidence that dislocations are non-radiative recombination centers in GaN", J. J. Appl. Phys. 37, L398, (1998).

[79] D. Cherns, S. J. Henley and F. A. Ponce, "Edge and screw dislocations as nonradiative centers in InGaN/GaN quantum well luminescence", Appl. Phys. Lett. 78, 2691, (2001).

[80] X. H. Wu, L. M. Brown, D. Kapolnek, S. Keller, B. Keller, P. DenBaars and J. S. Speck, "Defect structure of metal-organic chemical vapor deposition-grown epitaxial (0001) GaN/Al2O3", J. Appl. Phys. 80, 3228, (1996).

[81] F. A. Ponce, D. Cherns, W. T. Young, and J. W. Steeds, Characterization of dislocations in GaN by transmission electron diffraction and microscopy techniques. Appl. Phys. Lett. 69, 770, (1996).

[82].http://www.geology.um.maine.edu/geodynamics/AnalogWebsite/UndergradProjects2010 /PatrickRyan/ Content/dislocationdiagram.jpg.

[83] K. Kim, W. Lambrecht and B. Segall, Elastic constants and related properties of tetrahedrally bonded BN, AlN, GaN, and InN Phys. Rev. B 53 16310–26, (1996).

[84] A. Wright, Elastic properties of zinc-blende and wurtzite AlN, GaN, and InN J. Appl. Phys. 82 2833–9, (1997).

[85] Y. Takagi, M. Ahart, T. Azuhata, T. Sota, K. Suzuki and S. Nakamura, Brillouin scattering study in the GaN epitaxial layer Phys. B Condens. Matter 219–220 547–9, (1996).

[86] A.Polian, M. Grimsditch and I. Gregory, Elastic constants of gallium nitride J. Appl. Phys. 79 3343–4 156, (1996).

[87] M. Yamaguchi, T. Yagi, T. Azuhata, T. Sota, K. Suzuki, S. Chichibu and S. Nakamura, Brillouin scattering study of gallium nitride: elastic stiffness constants J. Phys. Condens. Matter 9 241, (1997).

[88] C.Deger, E. Born, H. Angerer, O.Ambacher, M. Stutzmann, J. Hornsteiner, E. Riha and G. Fischerauer, Sound velocity of AlxGa1−xN thin films obtained by surface acoustic wave measurements Appl. Phys. Lett. 72 2400–2, (1998).

[89] l. McNeil, M. Grimsditch and R. French, Vibrational Spectroscopy of Aluminum Nitride J. Am. Ceram. Soc. 76 1132–6, (1993).

[90] F. Bernardini and V. Fiorentini, ``Spontaneous Polarization and Piezoelectric Constants of III-V Nitrides," Phys.Rev.B, vol. 56, no. 16, pp. R10024-R10027, (1997).

[91] O. Ambacher, B. Foutz, J. Smart, J. Shealy, N. Weimann, K. Chu, M. Murphy, A. Sierakowski, W. Schaff, L. Eastman, R. Dimitrov, A. Mitchell, and M. Stutzmann, ``Two-Dimensional Electron Gases Induced by Spontaneous and Piezoelectric Polarization in Undoped and Doped AlGaN/GaN Heterostructures," J.Appl.Phys., vol. 87, no. 1, pp. 334-344, (2000).

[92] F. Bernardini, V. Fiorentini, and D. Vanderbilt, ``Accurate Calculation of Polarization-Related Quantities in Semiconductors," Phys.Rev.B, vol. 63, no. 19, p. 193201, (2001).

[93] O. Ambacher, J. Majewski, C. Miskys, A. Link, M. Hermann, M. Eickhoff, M. Stutzmann, F. Bernardini, V. Fiorentini, V. Tilak, B. Schaff, and L. Eastman, ``Pyroelectric Properties of Al(In)GaN/GaN Hetero- and Quantum Well Structures," J.Phys.: Condensed Matter, vol. 14, no. 13, pp. 3399-3434, (2002).

[94] W. Yan, R. Zhang, X. Xiu, Z. Xie, P. Han, R. Jiang, S. Gu, Y. Shi, and Y. Zheng, ``Temperature Dependence of the Pyroelectric Coefficient and the Spontaneous Polarization of AlN," Appl.Phys.Lett., vol. 90, no. 21, p. 212102(3), (2007).

[95] Wilson, J. and J.F.B. Hawkes, Optoelectronics, an introduction to Prentice-Hall, (1989).

[96] Agrawal, G.P. and N.K. Dutta, Long-wavelength semiconductor lasers, Van Nostrand Reinhold, (1998).

[97] Zory, P.S., Quantum well lasers, Academic Press, (1993).

[98] N. Nepal, J. Li, M.L. Nakarmi, J.Y. Lin, H.X. Jiang, Temperature and compositional dependence of AlGaN the energy band gap of alloys, Appl. Phys. Lett. 87, 242104, (2005).

[99] L.F. Jiang, W.Z. Shen, H. Ogawa, Q.X. Guo, Temperature dependence of the optical properties in hexagonal AlN, J. Appl. Phys. 94, 5704, (2003).

[100] H. Dakhlaoui, J. Appl. Phys., 117,1357051-1357059, (2015).

[101] Z. Dridi, B. Bouhafs and P. Ruterana, First-principles investigation of lattice constants and bowing parameters in wurtzite AlxGa1−xN, InxGa1−xN and InxAl1−xN alloys Semicond. Sci. Technol. 18 850, (2003).

[102] I. Vurgaftman and J. Meyer, Band parameters for nitrogen-containing semiconductors J. Appl. Phys. 94 3675–96, (2003).

[103] M. Levinshteĭn, S. Rumyantsev and M. Shur, Properties of advanced semiconductor materials: GaN, AlN, InN, BN, SiC, SiGe, New York: Wiley, (2001).

[104] Y-N. Xu and W. Ching, Electronic, optical, and structural properties of some wurtzite crystals Phys. Rev. B 48 4335–51, (1993).

[105] B. SanticOn the hole effective mass and the free hole statistics in wurtzite GaN Semicond. Sci. Technol. 18 219–24, (2003).

[106] L. Ramos, L. Teles, L. Scolfaro, J. Castineira, A. Rosa and J. Leite, Structural, electronic, and effective-mass properties of silicon and zinc-blende group-III nitride semiconductor compounds Phys. Rev. B 63 165210, (2001).

[107] S. Figge, H. Kröncke, D. Hommel and B. Epelbaum, Temperature dependence of the thermal expansion of AlN Appl. Phys. Lett. 94 101915, (2009).

[108] C.Roder, S. Einfeldt, S. Figge and D. Hommel ,Temperature dependence of the thermal expansion of GaN Phys. Rev. B 72 085218, (2005).

[109] R. B. Araujo, J. S. de Almeida, and A. Ferreira da Silva, Electronic properties of III-nitride semiconductors: A first-principles investigationusing the Tran-Blaha modified Becke-Johnson potential, Journal of applied physics, 114(18):183702-183702-6, (2013).

[110] C. Cobet, N. Esser, J. T. Zettler, and W. Richter, Optical properties of wurtzite AlxGa1-xN (x<0.1) parallel and perpendicular to the c axis, Physical Review B, 64(16):165203, (2001).

[111] A.philippe, "caractérisation électrique et optique du nitrure de gallium'', INSA de Lyon, (1999).

[112] I. Vurgaftmana and J. R. Meyer, "band parameters for III-V compound semiconductors and their alloys", J. Appl. Phys., Vol. 89, N 11, (2001).

[113] C. Persson et al. "Effective electronic masses in wurtzite and zinc-blende GaN and AlN", Journal of crystal growth 231, 397-406, (2001).

[114] A. T. Meney et al. ''Optical gain in wide bandgap GaN-quantum well". Semcond. Sci. Technol. 11, 897-903, (1996).

[115] Seoung-Hwan, Yong-Tak Lee, "Intra band relaxation time in zinc-blende GaN/AlGaN quantum-well structures" JKPS, Vol. 35 No. 6, pp. 512-515, (1999).

[116] Isamu Akasaki & Hiroshi Amano, “crystal growth and conductivity control of III-N” Jpn. J. Allp. Phys. Vol 35, pp. 5393-5408 (1997).

[117] Steven P. Den Baars, “Gallium nitride materials technology” France, (2000).

[118] R. Kehl Sink “Cleaved-Facet Group-III Lasers” University of California, December, (2000).

[119] J.Wu et al. “Cleaved cavity stimulated emission from an optically pumped cubic GaN/AlGaN” Appl. Phys. Lett., Vol 73, N° 14, (1998).

[120] Takanobu S. et al, “Optical Characterisation of AlGaN Epilayers” Phys. Stat. sol. B 216,211, (1999).

[121] J. Kepler, “Linear optical properties of III-nitride semiconductors between 3 and 30eV”, Phd thesis, University Linz, (2005).

[122] O. Ambacher. Growth and applications of group III–nitrides. J. Phys. D: Appl. Phys., 31:2653, (1998).

[123] H. Morkoç, Nitride Semiconductors and Devices, Springer Berlin Heidelberg, Springer Series in Materials Science, Print ISBN: 978-3-642-63647-9.

[124] H. P. Maruska and J. J. Tietjen. The preparation and properties of vapour–deposited single–crystal–line GaN. Appl. Phys. Lett., 15:327, (1969).

[125] S. Yoshida, S. Misawa, and S. Gonda. Improvements on the electrical and luminescent properties of reactive molecular beam epitaxially grown GaN films by using AlN–coated sapphire substrates. J. Appl. Phys., 42:427, (1983).

[126] H. Amano, M. Kito, K. Hiramatsu, and I. Akasaki, P-Type Conduction in Mg-Doped GaN Treated with Low-Energy Electron Beam Irradiation (LEEBI), Jpn. J. Phys. 28, L2112, (1989).

[127] H. Amanoand M. Kito, K. Hiramatsu, and I. Akasaki. P–type conduction in Mg–doped GaN treated with low–energy electron beam irradiation (LEEBI). Jpn. J. Appl. Phys, 28: L2112, (1989).

[128] S. Nakamura, T. Mukai, M. Senoh, and N. Iwasa. Thermal annealing effects on p–type Mg doped GaN films. Jpn. J. Appl. Phys., 31: L139, (1992).

[129] A. Van Vechten, J. David Zook, Robert D. Horning and B. Goldenberg, Defeating Compensation in Wide Gap Semiconductors by Growing in H that is Removed by Low Temperature De-Ionizing Radiation, The Japan Society of Applied Physics, 31 3662, (1992).

[130] Pankove Jacques. Electroluminescent semiconductor device of GaN. U.S. Patent 3,683,240, (1972).

[131] M. Inamori,H. Sakai,T. Tanaka,H. Amano, and I.Akasaki, Direct Patterning of the Current Confinement Structure for p-Type Column-III Nitrides by Low-Energy Electron Beam Irradiation Treatment J. Appl. Phys.34, 1190, (1995).

[132] V.Yu. Davydov, A.A. Klochikhin, R.P. Seisyan, V.V. Emtsev, S.V. Ivanov, F. Bechstedt, J. Furthmuller, H. Harima, A.V. Mudryi, J. Aderhold, O. Semchinova and J. Graul, 'Absorption and Emission of Hexagonal InN. Evidence of Narrow Fundamental Band Gap', Physica Status Solidi B, Vol. 229, N°3, pp. r1-r3, (2002).

[133] J. Wu, W. Walukiewicz, K.M. Yu, J.W. Ager, E.E. Haller, H. Lu and W.J. Schaff, 'Small Band Gap Bowing in In1-xGaxN alloys', Applied Physics Letters, Vol. 80, N°25, pp. 4741-4743, (2002).

[134] T. Matsuoka, H. Okamoto, M. Nakao, H. Harima and E. Kurimoto, 'Optical Band Gap Energy of Wurtzite InN', Applied Physics Letters, Vol. 81, N°7, pp. 1246 - 1248, (2002).

[135] L.-H. Peng, C.-W. Chuang, Y.-C. Hsu, J.-K. Ho, C.-N. Huang, and C.-Y. Chen, Deep ultraviolet enhanced wet chemical oxidation and etching of gallium nitride, Optical Society of America, (1998).

[136] M. Iwaya, T. Takeuchi, S. Yamaguchi, C. Wetzel, H. Amano and I. Akasaki, Reduction of Etch Pit Density in Organometallic Vapor Phase Epitaxy-Grown GaN on Sapphire by Insertion of a Low-Temperature-Deposited Buffer Layer between High-Temperature-Grown GaN, Jpn. J. Appl. Phys. 37 L316, (1998).

[137] T. Zheleva, S. Smith, D. Thomson, K. Linthicum, P. Rajagopal and R. Davis, Pendeo-epitaxy: A new approach for lateral growth of gallium nitride films, Journal of Electronic Materials volume 28, pagesL5–L8, (1999).

[138] S. Nakamura, G. Fasol, The Blue Laser Diode, ISBN: 978-3-662-03462-0, (1997).

[139] R. García, S. Srinivasan, Oe Contreras, A.Tomas, AlxGa1−xN (0⩽x⩽1) nanocrystalline powder by pyrolysis route, Journal of Crystal Growth 308(1):198-203, (2007).

[140] C. Hsieh, M. Chang, Y. Chien, L. Chou, L. Chen, and C. Chen, Coaxial Metal-Oxide-Semiconductor (MOS) Au/Ga2O3/GaN Nanowires, Nano Lett. 2008, 8, 10, 3288–3292, (2008).

[141] A. Patsha, P. Sahoo, S. Amirthapandian, A. Prasad, A. Das, A. Tyagi, M. Cotta, and S. Dhara, Localized Charge Transfer Process and Surface Band Bending in Methane Sensing by GaN Nanowires, J. Phys. Chem. C,27 Aug, (2015).

[142] B. AlOtaibi, S. Fan, D. Wang, J Ye, Z Mi, Wafer-Level Artificial Photosynthesis for CO2 Reduction into CH4 and CO Using GaN Nanowires, ACS Catal, 5, 9, 5342–534, (2015).

[143] W. Feng Huang, R. Zheng, H. Wu, Low-Dimensional Structure Vacuum-Ultraviolet-Sensitive ($\lambda < 200$ nm) Photodetector with Fast-Response Speed Based on High-Quality AlN Micro/Nanowire, Advanced Materials, (2015).

[144] Group-III-nitride (inn, gan, aln) semiconductor materials: properties, growth and applications, Anna University, Chennai 600 025.

[145] Geeta Rani Mutta, Propriétés structurales, optiques, électroniques des couches d'InN heterostructure riches en Indium pour applications optoélectroniques. Electronique. Université de Caen, (2012).

[146] L. Liu and J.H. Edgar, "Substrates for gallium nitride epitaxy", Mat. Sci. and Engg. R 37, 61, (2002).

[147] A.R.D Yadira, A Ph.D thesis on "Characterization of A-plane Grown GaN on Sapphire Substrates by Electron Microscopy", Lausanne, EPFL, (2009).

[148] S. Tanaka, R. S. Kern and R. F. Davis, "Initial stage of aluminum nitride film growth on 6H-silicon carbide by plasma-assisted, gas-source molecular beam epitaxy", Appl. Phys. Lett. 66,1, (1995).

[149] C. D. Lee, Ashutosh sagar, R. M. Feenstra, W. L. Sarney, L. Salamanca-riba and J. W. P. Hsu, "Growth of GaN on SiC (0001) by Molecular Beam Epitaxy", Phys. Stat. Sol. (a) 188, 595, (2001).

[150] H. P. Mauska and J. J. Tietjen, "The preparation and properties of vapor-deposited single crystal-line GaN", Appl. Phys. Lett., vol. 15, no. 10, pp. 327–329, (1969).

[151] M. J. almond, C. E. Jenkins, D. A. Rice, and k. Hagen, "Organometallic formation of GaN by MOCVD: structural characterisation of Me3Ga · NH3 by gas-phase electron diffraction," J. Organomet. Chem, vol. 439, no. 3, pp. 251–261, (1992).

[152] E. V. Etzkorn and D. R. Clarke, "Cracking of GaN films, J. Appl. Phys., vol. 89, no. 2, pp. 1025– 1034, (2001).

[153] D. Kapolnek, X. H. Wu, B. Heying, S. Keller, B. P. Keller, U. K. Mishra, S. P. DenBaars, and J. S. Speck "Structural evolution in epitaxial metalorganic chemical vapour deposition grown GaN films on sapphire", Appl. Phys. Lett., vol. 67, no. 11, pp. 1541–1543, (1995).

[154] G. Martinez-Criado, M. Kuball, M. Benyoucef, A. Sarua, E. Frayssinet, B. Beaumont, P. Gibart, C. R. Miskys, and M. Strutzmann "Free-standing GaN grown on epitaxial lateral overgrown GaN substrates", J. Cryst. Growth, vol. 255, no. 3–4, pp. 277–281, (2003).

[155] R. J. Molnar, W. Götz, L. T. Romano, and N. M. Johnson, "Growth of gallium nitride by hibride vapour-phase-epitaxy," J. Cryst. Growth, vol. 178, no. 1–2, pp. 147–156, (1997).

[156] E. Richter, C. Hennig, M. Weyers, F. Habel, J.-D. Tsay, W.-Y. Liu, P. Brückner, F. Scholz, Y. Makarov, A. Segal, and J. Kaeppler "Reactor and growth process optimization for growth of thick GaN layers on sapphire substrates by HVPE, "J. Cryst. Growth, vol. 277, no. 1–4, pp. 6–12, (2005).

[157] M. K. Kelly, R. P. Vaudo, V. M. Phanse, L. Görgens, O. Ambacher, and M. Strutzman, "Large Free-Standing GaN Substrates by Hydride Vapor Phase Epitaxy and Laser-Induced lift-off," Jpn. J. Appl. Phys., vol. 38, no. 3A, p. L217, (1999).

[158] K. Motoki, T. Okahisa, N. Matsumoto, M. Matsushima, H. Kimura, H. Kasai, K. Takemoto, K. Uematsu, T. Hirano, M. Nakayama, S. Nakahata, M. Ueno, D. Hara, Y. Kumagai, A. Koukitu, and H. Seki, "Preparation of Large Freestanding GaN Substrates by Hybride Vapor Phase Epitaxy," J. Appl. Phys., vol. 40, no. 2B, p. L140, (2001).

[159] X. Xu, R. Vaudo, C. Loria, A. Salant, G. Bades, and J. Chaudhuri, "Growth and characterization of low defect GaN by hybride vapor phase epitaxy," J. Cryst. Growth, vol. 246, no. 3–4, pp. 223–229, (2002).

[160] R. Held, D. E. Crawford, A. M. Johnson, A. M. Dabiran, and P. I. Cohen, "In situ control of GaN growth by molecular beam epitaxy," J. Electron. Mater., vol. 26, no. 3, pp. 272–280, (1997).

[161] J.W.Shon, J. Ohta, K. Ueno, A. Kobayashi, and H. Fujioka, "Fabrication of full-color InGaN-based light-emitting diodes on amorphous substrates by sputtering," Sci. Rep., vol. 4, (2014).

[162] W. Walukiewicz: Intrinsic limitations to the doping of wide-gap semiconductors, Proc. Yamada Conf. LIV 9th Int. Conf. Shallow-Level Centers in Semiconductors, p. 123, (2001).

[163] H. Morkoç: Handbook of Nitride Semiconductors and Devices, Vol. 1 (Wiley, Weinheim 2008)

[164] N. Koide, H. Kato, M. Sassa, S. Yamasaki, K. Manabe, M. Hashimoto, H. Amano, K. Hiramatsu, I. Akasaki: Doping of GaN with Si and properties ofbluem/i/n/n+ GaN LED with Si-doped n+-layer by MOVPE, J. Cryst. Growth 115(1–4), 639, (1991).

[165] Y.A. Xi, K.X. Chen, F. Mont, J.K. Kim, E.F. Schubert, W. Liu, X. Li, J.A. Smart: Comparative study of n-type AlGaN grown on sapphire by using a superlattice layer and a low-temperature AlN interlayer, J. Cryst. Growth 299(1), 59, (2007).

[166] H. Morkoç: Handbook of Nitride Semiconductors and Devices, Vol. 2, Wiley, Weinheim, (2008).

[167] W. Gotz, N.M. Johnson, C. Chen, H. Liu, C. Kuo, W. Imler: Activation energies of Si donors in GaN, Appl. Phys. Lett. 68(22), 3144, (1996).

[168] W.J. Moore, J.A. Freitas, S.K. Lee, S.S. Park, J.Y. Han: Magneto-optical studies of free-standing hydride-vapor-phase epitaxial GaN, Phys. Rev. B 65(8), 081201, (2002).

[169] P.J. Dean, J.D. Cuthbert, D.G. Thomas, R.T. Lynch: Two-electron transitions in the luminescence of excitons bound to neutral donors in gallium phosphide, Phys. Rev. Lett. 18(4), 122, (1967).

[170] M. Wieneke, H. Witte, K. Lange, M. Feneberg, A. Dadgar, J. Blasing, R. Goldhahn, A. Krost: Ge as a surfactant in metal-organic vapour phase epitaxy growth of a-plane GaN exceeding carrier concentrations of 1020 cm-3, Appl. Phys. Lett. 103(1), 012103, (2013).

[171] S. Nakamura, T. Mukai, M. Senoh: Si- and Ge doped GaN films grown with GaN buffer layers, Jpn. J. Appl. Phys. 31, 2883, (1992).

[172] J.K. Sheu, G.C. Chi: The doping process and dopant characteristics of GaN, J. Phys. Condens. Matter 14(22), 657, (2002).

[173] H. Amano, M. Kito, K. Hiramatsu, I. Akasaki: Ptype conduction in Mg-doped GaN treated with low-energy electron beam irradiation (LEEBI), Jpn. J. Appl. Phys. 28(12A), L2112, (1989).

[174] S. Nakamura, M. Senoh, T. Mukai: Highly p-typed Mg-doped GaN films grown with GaN buffer layers, Jpn. J. Appl. Phys. 30(10A), L1708, (1991).

[175] S. Nakamura, T. Mukai, M. Senoh, N. Iwasa: Thermal annealing effects on p-type Mg-doped GaN films, Jpn. J. Appl. Phys. 31(2B), L139, (1992).

[176] H. Amano, M. Kitoh, K. Hiramatsu, I. Akasaki: Growth and luminescence properties of Mg doped GaN prepared by MOVPE, J. Electrochem. Soc. 137(5), 1639, (1990).

[177] H. Obloh, K.H. Bachem, U. Kaufmann, M. Kunzer, M. Maier,A. Ramakrishnan, P. Schlotter: Self compensation in Mg doped p-type GaN grown by MOCVD, Proc. Metalorganic Vapour Phase Epitaxy 1998. Ninth Int. Conf, p. 270, (1998).

[178] W. Kim, A.E. Botchkarev, A. Salvador, G. Popovici, H. Tang, H. Morkoc: On the incorporation of Mg and the role of oxygen, silicon, and hydrogen in GaN prepared by reactive molecular beam epitaxy, J. Appl. Phys. 82(1), 219, (1997).

[179] W. Kim, A. Salvador, A.E. Botchkarev, O. Aktas, S.N. Mohammad, H. Morcoç: Mg-doped p-type GaN grown by reactive molecular beam epitaxy, Appl. Phys. Lett. 69(4), 559, (1996).

[180] W. Gotz, N.M. Johnson, J. Walker, D.P. Bour, R.A. Street: Activation of acceptors in Mg-doped GaN grown by metalorganic chemical vapor deposition, Appl. Phys. Lett. 68(5), 667, (1996).

[181] I.D. Goepfert, E.F. Schubert, A. Osinsky, P.E. Norris: Demonstration of efficient p-type doping in AlxGa1xN/GaN superlattice structures, Electron. Lett. 35(13), 1109, (1999).

[182] P. Kozodoy, H. Xing, S.P. DenBaars, U.K. Mishra, A. Saxler, R. Perrin, S. Elhamri, W. C. Mitchel: Heavy doping effects in Mg-doped GaN, J. Appl. Phys. 87(4), 1832, (2000).

[183] T. Tanaka, A. Watanabe, H. Amano, Y. Kobayashi, I. Akasaki, S. Yamazaki, M. Koike: p-Type conduction in Mg-doped GaN and Al0:08Ga0:92N grown by metalorganic vapor phase epitaxy, Appl. Phys. Lett. 65(5), 593, (1994).

[184] M. Suzuki, J. Nishio, M. Onomura, C. Hongo: Doping characteristics and electrical properties of Mg-doped AlGaN grown by atmospheric-pressure MOCVD, Proc. Second Int. Conf. Nitride Semiconductors, p. 51, (1998).

[185] L. Sugiura, M. Suzuki, J. Nishio, K. Itaya, Y. Kokubun, M. Ishikawa: Characteristics of Mg doped GaN and AlGaN grown by H2-ambient and N2-ambient metalorganic chemical vapor deposition, Jpn. J. Appl. Phys. Part 1 37(7), 3878, (1998).

[185] J. Li, T.N. Oder, M.L. Nakarmi, J.Y. Lin, H.X. Jiang: Optical and electrical properties of Mg-doped p-type AlxGa1-xN, Appl. Phys. Lett. 80(7), 1210, (1998) p. 511, (2002).

[186] H. Yu, E. Ulker, E. Ozbay: MOCVD growth and electrical studies of p-type AlGaN with Al fraction 0.35, J. Cryst. Growth 289(2), 419, (2006).

[187] S.N. Mohammed, H. Morkoc: Progress and prospects of group-III nitride semiconductors, Prog. Quantum Electron. 20(5/6), 361, (1996).

[188] L.K. Li, M.J. Jurkovic, W.I. Wang, J. Van Hove, P.P. Chow: Surface polarity dependence of Mg doping in GaN grown by molecular-beam epitaxy, Appl. Phys. Lett. 76(13), 1740, (2000).

[189] A.J. Ptak, T.H. Myers, L.T. Romano, C.G.J.E. Van de Walle: Northrup: Magnesium incorporation in GaN grown by molecular-beam epitaxy, Appl. Phys. Lett. 78(3), 285, (2001).

[190] S. Guha, N.A. Bojarczuk, F. Cardone: Mg in GaN: Incorporation of a volatile species at high temperatures during molecular beam epitaxy, Appl. Phys. Lett. 71(12), 168, (1997).

[191] T.S. Cheng, S.V. Novikov, C.T. Foxon, J.W. Orton: Mechanisms of magnesium incorporation into GaN layers grown by molecular beam epitaxy, Solid State Commun. 109 (7), 439, (1999).

[192] I.P. Smorchkova, E. Haus, B. Heying, P. Kozodoy, P. Fini, J.P. Ibbetson, S. Keller, S.P. DenBaars, J.S. Speck, U.K. Mishra: Mg doping of GaN layers grown by plasma-assisted molecular-beam epitaxy, Appl. Phys. Lett. 76(6), 718, (2000).

[193] Nakarmi M L, Kim K H, Zhu K, Lin J Y and Jiang H X 2004 Transport properties of highly conductive n-type Al-rich AlxGa1−xN(x⩾0.7) Appl. Phys. Lett. 85 3769–71

[194] B. Borisov, V. Kuryatkov, Y. Kudryavtsev, R. Asomoza, S Nikishin, D. Song, M. Holtz and H. Temkin, Si-doped AlxGa1−xN(0.56⩽×⩽1) layers grown by molecular beam epitaxy with ammonia Appl. Phys. Lett. 87 132106, (2005).

[194] R. Collazo, S. Mita, J. Xie, A. Rice, J. Tweedie, R. Dalmau and Z. Sitar, Progress on ntype doping of AlGaN alloys on AlN single crystal substrates for UV optoelectronic applications Phys. Status Solidi C 8 2031–3,(2011).

[195] F. Mehnke, T. Wernicke, H. Pingel, C. Kuhn, C. Reich, V. Kueller, A. Knauer, M. Lapeyrade, Weyers M and Kneissl M 2013 Highly conductive n-AlxGa1−xN layers with aluminum mole fractions above 80% Appl. Phys. Lett. 103 212109

[196] P. Bogusławski, and J. Bernholc, Doping properties of C, Si, and Ge impurities in GaN and AlN Phys. Rev. B 56 9496–505, (1997).

[197] L. Gordon, J. Lyons, A. Janotti, V. Walle, Hybrid functional calculations of D X centers in AlN and GaN Phys. Rev. B 89 085204, (2014).

[198] C.Park and D. Chadi, Stability of deep donor and acceptor centers in GaN, AlN, and BN Phys. Rev. B 55 12995–3001, (1997).

[199] L. Silvestri, K. Dunn, S. Prawer, Hybrid functional study of Si and O donors in wurtzite AlN Appl. Phys. Lett. 99 122109, (2011).

[200] C. Skierbiszewski, T. Suski, M. Leszczynski, M. Shin, M. Skowronski, M. Bremser and R. Davis, Evidence for localized Si-donor state and its metastable properties in AlGaN Appl. Phys. Lett. 74 3833–5, (1999).

[201] X. Trinh, D. Nilsson, I Ivanov, E. Janzén, A. Kakanakova-Georgieva and N. Son, Stable and metastable Si Negative-U centers in AlGaN and AlN Appl. Phys. Lett. 105 162106, (2014).

[202] Taniyasu Y, Kasu N. Kobayashi, Intentional control of n-type conduction for Si-doped AlN and AlxGa1−xN ($0.42 \leqslant x < 1$) Appl. Phys. Lett. 81 1255–7, (2002).

[203] H.C. Casey, M.B Panish, Heterostructure Lasers, ISBN 0-12-163101-X (Two volumes. Part A: Fundamental Principles and Part B: Materials and Operating Characteristics, (Academic Press, 1st edn, (1978).

[204] H. Kressel, J. Butler, Semiconductor Lasers and LEDs, ISBN 0-12-426250-3, (Academic Press, 1st edn, (1997).

[205] P. Hewitt, "Conceptual physics", (2002).

[206] M. S. Hu, G. M. Hsu, K. H. Chen, C. J. Yu, H. C. Hsu, L. C. Chen, J. S. Hwang, L. S. Hong and Y. F. Chen, "Infrared lasing in InN nanobelts", Appl. Phys. Lett. 90, 123109, (2007).

[207] J. J. Lee, L. J. Mawst, and D. Botez, "Asymmetric Broad Waveguide Diode Lasers (lambda = 980 nm) of Large Equivalent Transverse Spot Size and Low Temperature Sensitivity," IEEE Photonics Technology Letters, vol. 14, no. 8, pp. 1046–1048, (2002).

[208] M. Fallahi and R. Bedford, "High-power semiconductor lasers," in Semiconductor lasers: Fundamentals and application, 2nd Edition, Woodhead, p. 662, (2013).

[209] B. Gefvert, C. Holton, A. Nogee, J. Hecht, Annual Laser Market Review & Forecast 2020: Laser markets navigate turbulent times, Jan 28th, (2020).

[210] E. J. Hall, J. D. Cox, in Radiation Oncology Ninth Edition, (2010)

[211] A. Einstein, On the quantum theory of radiation. Phys. Z., 18, 121, (1917).

[212] Bulletin de la société des enseignants de Sciences, Physique, (2005).

[213] M. Fox, Quantum Optics: An Introduction, Oxford University Press, (2007).

[214] Koechner, W. and Bass, Solid State Lasers: A Graduate Text, Springer, (2003).

[215] R. Gresset, G. Lobet, C. Ponçot, G. Renoud-Lias, (2005).

[218] Saleh, B.E.A. and Teich, M.C. Fundamentals of Photonics, John Wiley & Sons, Inc, (2007).

[219] Fgenoud « Semi-conducteurs – diode laser » Plate-forme Matière Condensée et Cristallographie (MCC)- C.E.S.I.R.E. Université J. Fourier Grenoble.

[210] M. Asada, A.kameyama, Y.suematsu, IEEE J. «Fabrication of 780-nm AlGaAs Tunable distributed bragg reflector laser diode by using composional disordering of a quantum well» quantum Electron. QE-20,745, (1984).

[221] M. A. Dem'yanenko, D. G. Esaev, A. I. Toropov, quantum well detectors, Intechopen.71266, (2017).

[222] K. K. Thomber, "Relation of Drift Velocity to Low-Field Mobility and High Field Saturation Velocity", J. Appl. Phys., 51,2127, (1980).

[223] J. G Ruch, "Electron Dynamics in Short Channel Field-Effect Transistors," IEEE Trans. Electron Devices, ED-19, 652, (1972).

[224] C. Zener, Proc. Roy. Soc. London A 130, 499, (1931).

[225] J. Frenkel, Phys. Z. Sowjetunion 9, 158 (1936)

[226] Henry Mathieu, "physique des semiconducteurs et composants électroniques", Masson, (1998).

[227] P. Kiréev "la physique des semiconducteurs ", Mir, Moscow, (1975).

[228] T. Peng & J. Piprek. "Refractive index of AlGaInN alloys", Electronics Letters, Vol. 32 No.24, (1996).

[229] S. Takanobu et al, "Optical constants of GaN, AlN, & AlGaN alloys", Jpn. J.Appl. phy. Vol 39 (2000) pp. L[207] https:/www.ioffe.rssiru/SVA/NSM/Semicond/InP/index.html. [Accessed 15.02.2015]

[230] SILVACO-TCAD, ATLAS User's Manual: Device simulation software, SILVACO International, California, (2016).

[231] N. Nepal, J. Li, M.L. Nakarmi, J.Y. Lin, H.X. Jiang, Temperature and compositional dependence of AlGaN the energy band gap of alloys, Appl. Phys. Lett. 87 242104, (2005).

[232] L.F. Jiang, W.Z. Shen, H. Ogawa, Q.X. Guo, Temperature dependence of the optical

properties in hexagonal AlN, J. Appl. Phys. 94, 5704, (2003).

[233] H. Dakhlaoui, J. Appl. Phys., 117,1357051-1357059 (2015).

[234] 290. Slotboom, J.W., "The PN Product in Silicon", Solid State Electronics 20, 279- 283 (1997).

[235] F. Bernardini and V. Fiorentini, "Spontaneous versus piezoelectric polarization in III–V Nitrides: Conceptual aspects and practical consequences," Phys. Stat. Sol. (b), vol. 216, pp. 391–398, (1999).

[236] O. Ambacher, J.Majewski, C. Miskys, A. Link, M. Hermann, M. Eickhoff, M. Stutzmann F. Bernardini, V. Fiorentini, V. Tilak, W. J. Schaff, and L. F. Eastman, "Pyroelectric properties of Al(In)GaN/GaN hetero and quantum well structures," J. Phys.: Condens. Matter, vol. 14, pp. 3399–3434, (2002).

[237] Shockley W., and W.T. Read, "Statistics of the Recombination of Holes and Electrons", Phys. Rev. 87, 835-842, (1952).

[238] Hall, R.N., "Electron Hole Recombination in Germanium", Phys. Rev. 87 (1952).

[239] Dziewior J. and W. Schmid, Auger coefficient for highly doped and highly excited Silicon, Appl. Phys. Lett. 31, pp. 346-348, (1977).

[240] K.H. Baik, Y. Irokawa, F. Ren, S.J. Pearton, and S.S. Park, Solid State Electron. 47, 1533 (2003).

[241] M. Razeghi and M. Henini, Optoelectronic Devices: III-Nitrides, Amsterdam: Elsevier, (2004).

[242] F. BOUZID, L. DEHIMI, and F. PEZZIMENTI, "Performance Analysis of a Pt/n-GaN Schottky Barrier UV Detector", Journal of ELECTRONIC MATERIALS, (2017).

[243] Caughey, D.M., and R.E. Thomas. "Carrier Mobilities in Silicon Empirically Related to Doping and Field." Proc. IEEE 55, 2192-2193, (1967).

[244] Selberherr, S., "Process and Device Modeling for VLSI", Microelectron. Reliab. 24 No. 2, 225-257, (1984).

[245] S. Dehimi, L. Dehimi, T. Asar, S. Özçelik, Modelling of a Cd1_xZnxTe/ZnTe Single

Quantum well for Laser Diodes, Journal of ELECTRONIC MATERIALS DOI:

10.1007/s11664-016-4984-5.

[246] H. Yoshida, M. Kuwabara, Y. Yamashita, Y. Takagi, K. Uchiyama, H. Kan, AlGaN-based laser diodes for the short-wavelength ultraviolet region, New J. Phys. 125013, (2009).

[247] T. Ohtoshi, K. Yamaguchi, C. Nagaoka, T. Uda, Y. Murayama, and N. Chionone, Solid-State Electron. 30, 627, (1987).

[248] http://www.superstrate.net/pv/physics/band-electron.html visited in 19/04/2020.

[249] S. L. Chuang and C. S. Chang, "k.p method for strained wurtzite semiconductors," Phys. Rev. B., vol. 54, pp. 2491–2504, (1996).

[250] S. L. Chuang, "Optical gain of strained wurtzite GaN quantum-well lasers," IEEE J. Quantum Electron., vol. 32, no. 10, pp. 1791–1800, Oct. 1996.

497-L4999. Part 2. No. 6A, (2000).

[251] A. Asgari, S. Dashti, Optimization of optical gain in AlxGa1-xN/GaN/AlxGa1-xN

strained quantum well laser, Optik, 123, 1546-1549, (2012).

PUBLICATION

Journal of Semiconductors
JOS iopscience.iop.org/jos www.jos.ac.cn

Modelling and optical response of a compressive-strained AlGaN/GaN quantum well laser diode

A. Menani, L. Dehimi, S. Dehimi, and F. Pezzimenti

Citation: A Menani, L Dehimi, S Dehimi, and F Pezzimenti, Modelling and optical response of a compressive-strained AlGaN/GaN quantum well laser diode[J]. *J. Semicond.*, 2020, 41(6), 062301.

View online: https://doi.org/10.1088/1674-4926/41/6/062301

ARTICLES

Journal of Semiconductors
(2020) 41, 062301
doi: 10.1088/1674-4926/41/6/062301

Modelling and optical response of a compressive-strained AlGaN/GaN quantum well laser diode

A. Menani[1], L. Dehimi[1, 2], S. Dehimi[3], and F. Pezzimenti[4, †]

[1]Laboratory of Metallic and Semiconducting Materials (LMSM), Department of Electrical Engineering, Biskra University, Biskra, Algeria
[2]Faculty of Science, Elhadj Lakhdar University, Batnal, Algeria
[3]Research Centre in Industrial Technology (CRTI), Algiers, Algeria
[4]DIIES – Mediterranea University of Reggio Calabria, Reggio Calabria, Italy

Abstract: The effects of the quantum well (QW) width, carrier density, and aluminium (Al) concentration in the barrier layers on the optical characteristics of a gallium nitride (GaN)-based QW laser diode are investigated by means of a careful modelling analysis in a wide range of temperatures. The device's optical gain is calculated by using two different band energy models. The first is based on the simple band-to-band model that accounts for carrier transitions between the first levels of the conduction band and valence band, whereas the second assumes the perturbation theory (k.p model) for considering the valence intersubband transitions and the relative absorption losses in the QW. The results reveal that the optical gain increases with increasing the n-type doping density as well as the Al molar fraction of the $Al_xGa_{1-x}N$ layers, which originate the GaN compressive-strained QW. In particular, a significant optical gain on the order of 5000 cm^{-1} is calculated for a QW width of 40 Å at room temperature. In addition, the laser threshold current density is of few tens of A/cm^2 at low temperatures.

Key words: laser diode; quantum well; optical gain; threshold current; temperature

Citation: A Menani, L Dehimi, S Dehimi, and F Pezzimenti, Modelling and optical response of a compressive-strained AlGaN/GaN quantum well laser diode[J]. *J. Semicond.*, 2020, 41(6), 062301. http://doi.org/10.1088/1674-4926/41/6/062301

1. Introduction

In the last few decades, gallium arsenide (GaAs) alloys and III–V semiconductors were the most commercialized materials for laser diodes (LDs)[1, 2]. However, although GaAs technology is mature and GaAs-based lasers are well known for their high efficiency in converting electricity into monochromatic light, the emission of coherent light is limited in the red and infrared regions of the optical spectrum[3–7]. Therefore, due to the small bandgap of these materials, III–V semiconductors are unsuitable for the fabrication of short-wavelength optical devices[8–15].

An important challenge in the field of optoelectronics is the development of short wavelength lasers which can emit coherent light in green, blue, violet, and ultraviolet (UV) regimes. In particular, III-nitride and IV wide bandgap materials have received a great attention for the promising realization of several devices[16–24]. These devices are able to operate at high power levels and high temperatures, due to their mechanical hardness and larger band offset[25–32]. Recently, GaN-based high efficiency short wavelength light emitting diodes (LEDs) and LDs have been commercialized by achieving apparent improvements in terms of crystal quality and conductivity control in solid-state lighting and high-density optical storage systems. In addition, one of the most interesting features of GaN is the realization of the wurtzite-type crystal for semiconductor lasers. Although zinc-blend GaN has also been studied, it still does not have as good qualities as the wurtzite crystal[33, 34].

In this paper, the optical gain and threshold current density of a compressive-strained AlGaN/GaN quantum well (QW) laser, which emits in the UV regime, have been investigated in a wide range of temperatures by means of the Atlas-Silvaco physical device simulator. The optical gain spectra have been calculated by using a simple parabolic band model and also a multiband formalism based on the perturbation theory (k.p model) that is particularly suited for crystals with wurtzite symmetry. In the first case, we have assumed the electron and hole wavefunctions calculated by taking into account transitions that occur only between the first levels of the conduction band and valence band (band-to-band model) similarly to Ref. [35]. In the second case, we have considered the intervalence band absorption effects from different energy levels, namely heavy-hole (HH), light-hole (LH), and split-off (SO), computed via a 6 × 6 k.p model in the QW region[36, 37]. This model, accounting for an intermixing of states in the valence subbands, provides a much more accurate coupling with the conduction band for an improved laser diode optical response. The calculated optical gain is around 5000 cm^{-1} for a QW width of 40 Å and an Al molar fraction of 0.1 at room temperature. The dependence of the laser threshold current density from temperature has been also investigated.

2. Calculation models and parameters

The optical gain can be defined as the fractional increase in photons per unit of length in response to a given photon flux[33]. The optical gain expression as a function of

Correspondence to: F Pezzimenti, fortunato.pezzimenti@unirc.it
Received 19 SEPTEMBER 2019; Revised 5 DECEMBER 2019.